



MARTIN-LUTHER
UNIVERSITÄT
HALLE-WITTENBERG

Master Thesis

Analysis of physical properties and impurities in Greenland
ice using optical and Raman microscopy



ALFRED-WEGENER-INSTITUT
HELMHOLTZ-ZENTRUM FÜR POLAR-
UND MEERESFORSCHUNG

Submitted by: Ina Kleitz
Gildemeisterstr. 4
27568 Bremerhaven
Ina.Kleitz@student.uni-halle.de

Supervisors: Jun.-Prof. Dr. Ilka Weikusat
Prof. Dr. Dr. h. c. Manfred Frühauf

Date: Bremerhaven, 22.10.2015

Acknowledgements

I want to thank Ilka Weikusat and Manfred Frühauf for supervising this thesis and for supporting me in any scientific and organizational issue. I thank Jan and Wataru for patient explanations during sample preparation. Knowing that you go hunting for particles too, kept me motivated and made me feel way more comfortable during my time in the lab.

Thanks to Christian Weikusat for giving advice during my work with the Raman microscope and for correcting my spectra identification. Thanks to Daniela Jansen, Stefanie Mahlich and Christian Weikusat for proof reading. I thank Sepp Kipfstuhl for patiently answering all my questions and discussing future challenges.

Furthermore, I thank the people of the glaciology section at the Alfred-Wegener-Institute, especially Melanie, Christine, Birthe and Stefanie who always cheered me up and kept me company during the lunchbreaks. I want to thank my roommates who provided some nice distraction when I needed it and helped me warming up after long days in the ice lab. I thank Jur and Dirk for endless Skype conversations and the awesome amount of Stroopwafels.

I want to thank my family. For everything.

Structure

Abstract

1. Introduction.....	8
2. Motivation.....	9
3. Fundamentals.....	10
3.1 The structure of ice Ih.....	10
3.2 Densification from snow to ice.....	11
3.3 Properties of ice.....	13
3.4 Impurities.....	19
3.4.1 Sources, transport and deposition.....	19
3.4.2 Impurity in the Greenland ice sheet.....	21
3.4.3 Location of impurities in ice.....	24
3.4.4 Influences on the microstructure.....	25
4. Samples and drilling site.....	27
5. Methods.....	28
5.1 Microstructure measurements.....	28
5.2 Continuous flow analysis.....	30
5.3 Linescan images.....	33
5.4 Microstructure mapping.....	34
5.5 Raman spectroscopy.....	35
5.6 Correlations.....	37
5.7 Data processing.....	39
5.7.1 CAxes and RunningMean-Programme.....	39
5.7.2 Raman software.....	40
5.7.3 Structure of the plots.....	41
6. Results.....	42
6.1 Preliminary result.....	42
6.2 Results of all bag plots.....	44
6.3 Case study bag 1346_201.....	46
6.4 Case study bag 1346_501.....	53
6.5 Comparison of section 201 and 501.....	57

7. Discussion.....	59
7.1 Influence of the impurities on the microstructure.....	59
7.2 Sulfate.....	61
7.3 Black Carbon.....	63
7.4 Raman spectroscopy.....	66
7.5 Relaxation.....	67
7.6 Possible sources of errors.....	70
8. Summary and outlook.....	72
9. References.....	75
10. Appendix.....	I
10.1 Plot of the total area (all bags).....	I
10.2 Results of the Shapiro-Wilk-Test.....	IV
10.3 All bag plots.....	V
10.4 Correlations coefficients for the chemical and physical parameters...XX	
10.5 Cross correlations for sections 201 and 501 of bag 1346.....XXIV	
10.6 Examples for the Raman spectra.....XXVIII	
10.7 Microstructure maps of section 201 and section 501 of bag 1346.....XXXVI	
10.8 Summarized results of the Raman measurements.....XXXVIII	

List of figures

Fig. 1: The structure of ice Ih (CUFFEY & PATERSON 2010, p. 31).....	11
Fig. 2: Hard and easy glide of an ice monocrystal (THORSTEINSSON 1996).....	13
Fig. 3: (a) a crystal without dislocations, (b) edge dislocation, (c) screw dislocation (HOOKE 1995).....	14
Fig. 4: A creep curve for a single crystal (THORSTEINSSON 1996).....	14
Fig. 5: A creep curve for polycrystalline ice (CUFFEY & PATERSON 2010)	15
Fig. 6: C-axis fabrics produced in simple stress systems by rotation and rotation accompanied by recrystallization (CUFFEY & PATERSON 2010)....	17
Fig. 7: Transport mechanisms of dust particles (RUTH 2002 (from HUA 1999))...	20
Fig. 8: Volcanic regions contributing tephra deposits to the Greenland ice-core records (1-Iceland, 2-Jan Mayen, 3-North America, 4-Alaska) (ABBOTT & DAVIES 2012)	23
Fig. 9: Location map for Greenland ice-core drill sites (ABBOT & DAVIES 2012).	27
Fig. 10: A microtome, used for the preparation of thin sections (KLEITZ 2013)....	28
Fig. 11: The Fabric Analyzer (TAMMEN 2012).....	28
Fig. 12: After data processing a trend image can be obtained (right), where the red areas show a c-axis parallel to the longitudinal axis of the ice core (Trend, left) (WEIKUSAT & KIPFSTUHL 2010).....	29
Fig. 13: A firn core before the melting process starts (CFA system of the Alfred-Wegener-Institute for Polar and Marine Research) (KLEITZ 2013).	30
Fig. 14: Schematic drawing of a CFA system (WEIBBACH, personal communication 2015).....	33
Fig. 15: Schematic drawing demonstrating the principle of a linescan instrument (SVENSSON ET AL. 2005).....	34
Fig. 16: The Raman microscope in the cold laboratory of the Alfred-Wegener-Institute.....	36
Fig. 17: Example of an identification of a Raman spectrum using the CrystalSleuth software.....	40
Fig. 18: The preliminary result for bag 1346 with dashed blue lines marking the edges of the thin sections	42
Fig. 19: Plot of the total area (mean grain size (pixel)*number of grains) for bag 1346.....	43

Fig. 20: Bag plot of bag 1346. The red rectangles mark section 201 and 501.....	45
Fig. 21: Microstructure map of section 201 with marked grain boundaries (blue) and labelled black dots (magenta).....	47
Fig. 22: Examples of black dots as they were labelled in the microstructure maps	48
Fig. 23: Examples of black dots forming conglomerates or chains (observed with the Raman microscope).....	49
Fig. 24: Schematic drawing showing how mixed and separated signals were generated.....	50
Fig. 25: Colour code for mixed and separated signals.....	51
Fig. 26: Bag 1346_201: microstructure map with the pie charts including the particles with a Raman spectrum as a mixed signal.....	52
Fig. 27: Microstructure map of section 501 with marked grain boundaries (blue) and labelled black dots (magenta).....	55
Fig. 28: Bag 1346_501: microstructure map with the pie charts including the particles with a Raman spectrum as a mixed signal.....	56
Fig. 29: Examples of black dots being located on a subgrain boundary/crack (observed with the Raman microscope).....	56
Fig. 30: Raman spectrum obtained from the organic compounds being located on a subgrain boundary/crack.....	57
Fig. 31: Pie charts summarizing the results of section 201 and 501 (mixed and separated signal).....	58
Fig. 32: Grain boundary pinning at a bubble (AZUMA ET AL. 2012).....	61
Fig. 33: Pie charts showing the results of IIZUKA ET AL. (2013) (1 and 2) in comparison to the results of this work (3). Pie chart (3) shows the amount of sulfates of both section 201 and 501 as separated signal.....	63
Fig. 34: Levoglucosan flux, northern hemisphere charcoal influx, temperature, June insolation, modeled burned area for high latitudes, preindustrial CH ₄ flux and atmospheric CO ₂ concentration over the last 15kyr (ZENNARO ET AL. 2015). The dashed black line marks the position of bag 1346...	65
Fig. 35: The LASM image (left) in comparison to the microstructure map (right) of bag 1346_201. The red lines in the LASM image mark the part from which the microstructure map was obtained.....	68
Fig. 36: A LASM image and a microstructure map of bag 1346_201 showing details of microstructural features.....	68

Fig. 37: Schematic drawing of the location of impurity layer n a sample in relation to different focal depths..... 69

Fig. 38: Bag 1346_201: plot of dust and mean grain size with a shift of 17mm... 70

Fig. 39: The cutting plan for the NEEM ice core (NEEM FIELD SEASON 2010)... 72

List of tables

Tab. 1: The chemical species and the main principles of their measuring methods.....	32
Tab. 2: The correlation coefficients for bag 1346_201. The blue colour marks the significant correlations (significance level 95%).....	46
Tab. 3: Assigning the Raman spectra into four groups.....	50
Tab. 4: The correlation coefficients for bag 1346_501. The blue colour marks the significant correlations (significance level 95%).....	54
Tab. 5: The correlation coefficients for bag 1346_201 calculated with a shift of 17 values. The blue colour marks the significant correlations (significance level 95%).....	71

Abstract

The aim of this study was to determine relations between the impurity content and the microstructural features of natural ice using Raman spectroscopy. It should be investigated whether certain chemical species can be related to microstructural features, such as grain boundaries. The method of Raman spectroscopy enables to measure the particles in situ without melting the ice samples. Fourteen bags of the NEEM ice core (North Greenland Eemian Ice Drilling), drilled from different depths, were chosen.

As a first step, data from fabric analysis (mean grain size and eigenvalue 3) were plotted together with data for the major ions obtained from continuous flow analysis and correlation coefficients between those parameters were calculated. The statistically significant correlations between the chemical and physical parameters remained sporadic. For a case study, two sections from Holocene ice from a depth of 739,75 m to 740,30 m were chosen. After mapping the microstructure of the sections, particles were labelled and counted (from a layer with a focal depth of approximately 500 μm). Using Raman spectroscopy the particles were measured in-situ and the chemical species of most of the compounds could be identified. The major components were sulfate, silica particles, TiO_2 , some organic species and black carbon, which mostly appeared as a mixed signal. No carbonates were found and no Raman spectra could be obtained from grain boundaries or triple junctions. The particles often appeared to be in clusters or conglomerates. The location of the particles in relation to grain boundaries was difficult to assess due to relaxation of the ice.

1. Introduction

Polar ice sheets can be regarded as major climate archives. The air that is trapped in the bubbles as well as the ratio of oxygen isotopes and the impurity content can give information about climate related processes and the composition of the paleo-atmosphere and help to reconstruct climate changes (e.g. FARIA ET AL. 2010; JOHNSON ET AL. 1997).

The NEEM ice core (North Greenland Eemian Ice Drilling) was drilled in order to obtain ice layers from the last interglacial, the Eem, which is considered to be an analog to a likely future climate, where a warming of about 2 to 4 °C per century is expected (NEEM COMMUNITY MEMBERS 2013; IPCC 2013). The Eem ended approximately 115 ky ago and mean annual temperatures in Greenland were about 1,5 °C to 5 °C higher in this period than today (NEEM COMMUNITY MEMBERS 2013; TURNEY & JONES 2010). In previous ice cores drilled in Greenland the Eemian layers were already molten or disturbed due to the ice flow near the bedrock and its related deformation processes (NEEM COMMUNITY MEMBERS 2013).

Due to gravity, the ice sheets are continuously spreading and a thinning of the layers in the deep ice leads to difficulties in dating those cores. Therefore, flow models have to be applied for dating and for these information about ice dynamics are essential. The flow law that was developed by GLEN (1955) is a model based on continuum mechanics and does not include internal deformation mechanisms and their influences on the rheological properties. Since ice is not a homogeneous material but shows variations (e.g. in grain sizes or density) with increasing depth as well as different viscosities in warm and cold stages, an improvement of the flow law is essential. It is observed that glacial ice shows a high impurity content and features small grains (e.g. PATERSON 1991). As the impurity content is the major difference between glacial and interglacial ice, impurities are considered to influence the grain sizes and slowing down grain boundary movement due to a pinning effect (ALLEY ET AL. 1986). In order to further determine the role of impurities and their influence on the microstructure of ice, this work aims at analyzing the undissolved impurities (black dots) in samples of the NEEM ice core using Raman spectroscopy as a major method. The key questions of this study are:

- Are there correlations between the impurity content and physical parameters?
- How are the impurities distributed within the polycrystal?
- What kind of impurities can be found (material, chemical species)?
- According to their location within the ice and their composition, are there any connections to microstructural features (e.g. grain boundaries)?

To answer these questions fourteen bags of the NEEM ice core were examined according to their microstructural features and impurity content. Data of the mean grain size and the eigenvalue 3 were obtained from the Fabric Analyzer, a polarized microscope to determine crystal orientations and from the RunningMean-Programme, a software written by J. EICHLER (2013) in addition to trend images that give an idea of the c-axis orientations. Furthermore, data from the continuous flow analysis (CFA) were used showing the variations of the major ions such as calcium, sodium, ammonium and nitrate as well as conductivity and dust content for the length of one bag. The data were plotted in order to visually determine possible correlations between the physical and chemical parameters. To identify layers of high impurity content, linescan images were included in the plots. After calculating correlation coefficients, two sections of one bag were chosen to perform a case study. For each section several microstructure mapping images were taken, which then were used to get an overview of the location and shape of grain boundaries and the location of the black dots. Due to the large number of black dots the study had to be focused on characteristic areas in which the black dots were then measured and identified with Raman spectroscopy.

2. Motivation

The correlation between impurities in ice and its microstructure has been described before (e.g. PATERSON 1991; FARIA ET AL. 2014a, b). However, the processes leading to this correlation are not well understood. Thus, it is necessary to analyze this relation in more detail with the now available data and methods.

This work is a continuation of my Bachelor thesis (KLEITZ 2013), where sporadic correlations between the physical and the chemical parameters, especially between the mean grain size and the content of sodium ions, were found in four bags of the NEEM ice core containing ice from a cold stage. It was concluded that more and stronger correlations might be concealed by

irregularities in the depth scale, which result in a slight mismatch of the data sets. For the continuation, the methods of microstructure mapping and Raman spectroscopy were included to get a more detailed picture about the distribution and chemical species of the impurities.

Raman spectroscopy is a non-destructive method, which requires just little sample preparation (e.g. SMITH & DENT 2005). In contrast, the CFA system requires melting of the sample, thus, impurities, which initially occurred as solid particles in the ice might dissolve during the measuring process (e.g. RÖTHLISBERGER ET AL. 2000; KAUFMANN ET AL. 2008). Furthermore, irregularities in the depth scale as well as in the resolution of the CFA can occur, whereas with a Raman system the particles can be analyzed in-situ (e.g. SMITH & DENT 2005). With the coupling of several datasets and methods this work aims to improve the knowledge about how impurities are distributed in the ice and gain more information about their chemical composition related to their location. Since some impurities are considered to have softening or hardening effects on the crystal structure (e.g. JONES & GLEN 1968; PATERSON 1991) that significantly can influence the deformation, the results of this study contribute to a better parameterization of ice flow.

3. Fundamentals

3.1 Structure of ice Ih

Presently, 12 crystalline structures of ice are known, however, under natural conditions only ice Ih is stable, and thus relevant for this thesis. The crystal lattice of ice shows a hexagonal structure, where the oxygen atoms are connected to the hydrogen atoms via strong covalent bonds. Weaker hydrogen bonds connecting the molecules result in a relatively low melting temperature (SCHULSON & DUVAL 2009, p.7). Every oxygen atom is surrounded by another four oxygen atoms in a tetrahedral arrangement. The molecules are concentrated in series of parallel planes, the so-called basal planes (HOBBS 1974, p.20). Within these planes the molecules are arranged in the closest possible packing (THORSTEINSSON 1996). The normal to the basal planes is referred to as c-axis which is the main symmetry axis of the ice crystal (PETRENKO & WHITWORTH 1999, p.16).

Bonds between the planes are much weaker than bond within one plane (HOOKE 1998, p.27) and the open crystallographic structure is reflected in the low density of ice compared to liquid water (HOBBS 1974, p.20).

The main features of the crystal structure are described by the Bernal-Fowler-ice rules, which state that two hydrogen atoms have to be attached to one oxygen atom via covalent bonds. Additionally, one hydrogen atom cannot have more than one hydrogen bond (see fig. 1). Deviation from those rules leads to defects in the crystal structure (PETRENKO & WHITWORTH 1999, p.16).

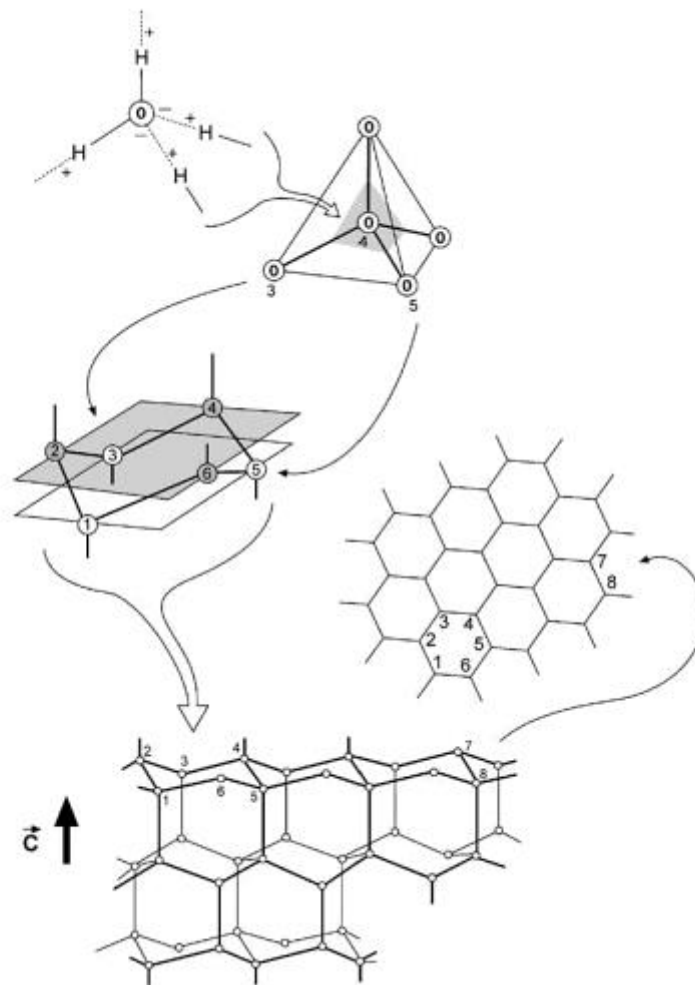


Fig. 1: The structure of ice Ih (CUFFEY & PATERSON 2010)

3.2 Densification from snow to ice

The densification of snow which results into consolidated ice, is driven by the thermodynamic principle stating that every system tries to minimize its free energy. Freshly fallen snow has a

density of approximately 100 to 200 kg/m³ (BLACKFORD 2007) and is mainly referred to as the material that did not undergo changes since its deposition (CUFFEY & PATERSON 2010, p.20). The free energy of snow can be reduced by mechanical destruction of the snow crystals. The fresh snowflakes with their complex shapes are transformed to rounded particles and tend to be redistributed in a way that reduces the total surface area of the crystals. The displacement of individual particles relative to their neighbours, also called settling, is the most important process in this initial state of transformation (CUFFEY & PATERSON 2010, p.20). Under natural conditions the closest packing can be reached with a corresponding porosity of 40 % implying that for further densification other processes must be involved (PATERSON 1994, p.17; HOOKE 1998, p.13).

The settling is followed by the process of sintering: due to sublimation and, to some extent molecular diffusion, material is transferred to points of contact between particles to form bonds (“necks”) resulting in a greater stability and lower energy of the system. The growth of the necks is controlled by the water vapor supply from the surrounding pore spaces (BLACKFORD 2007; CUFFEY & PATERSON 2010, p.21).

When the densification process reaches the firm state, no more loose particles exist, though grain boundaries are still visible (BLACKFORD 2007). Firm has a density of about 550 kg/m³ (HOOKE 1998, p.13). In firm, the pores are still connected, which allows an exchange of air through thin channels. With increasing density, the sublimation rate decreases and the firm becomes less porous. The contact areas between the grains increase while deformation and recrystallization occurs (CUFFEY & PATERSON 2010, p.21; BLACKFORD 2007). Furthermore, molecular diffusion alters shape and size of the crystals to reduce stress, and individual crystals deform by displacement along internal glide planes (PATERSON 1994; ALLEY 1987; CUFFEY & PATERSON 2010, p.21).

With ongoing densification pores close off and their shape changes from cylindrical to spherical. In this phase, around 90 % of the air already escaped through the snow layer surface, the remaining air is now trapped in bubbles (PATERSON 1994, p.18). After the close off the material can be referred to as “ice”, which has a density of 830 kg/m³ (HOOKE 1998, p.14; BLACKFORD 2007). In the Greenland ice sheet the pore close-off takes place at a depth of 50 to 120 m, where the ice is between several hundreds to several thousands of years old (HÖRHOLD ET AL. 2012). The zone where bubbles start to form is called the *zone of firn-ice-transition* (BLUNIER & SCHWANDER 2000). Deeper in the ice sheet (from 900 to 1600 m) the bubbles decrease in size due to the increasing pressure, and are finally integrated in the crystals as clathrate hydrates (CUFFEY & PATERSON 2010).

3.3 Properties of ice

Mechanical properties

Monocrystalline ice is highly anisotropic: when stress is applied on a crystal, the resulting deformation strongly depends on the direction of the stress relative to the c-axis (THORSTEINSSON 1996). A shear stress parallel to the basal planes causes shear deformation, because the basal planes slip past one another due to the weak bonding between them. This process is called easy glide (glide of the basal planes) and has profound consequences for the creep behaviour of polycrystalline ice (SCHULSON & DUVAL 2009; CUFFEY & PATERSON 2010:32). In contrast to that, a crystal is hard against a stress applied parallel to c-axis (hard glide) (THORSTEINSSON 1996) (see fig. 2). Hard glide is realized by dislocation glide along the prismatic and pyramidal crystallographic planes or by dislocation climb normal to basal planes (CUFFEY & PATERSON 2010, p.32).

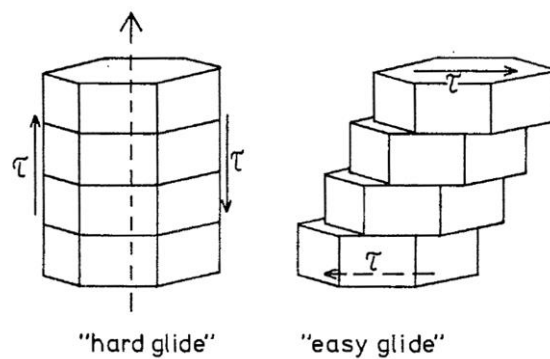


Fig. 2: Hard and easy glide of an ice monocrystal (THORSTEINSSON 1995)

Dislocations are linear defects in the crystal lattice, which allows a slip on basal planes and permit planes of atoms to move past each other much more rapidly than in a perfect crystal, thus influencing deformation processes significantly (WEERTMAN 1964; CUFFEY & PATERSON 2010:32) (see fig. 3). They are described by the *Burger's Vector*, which gives information about magnitude and direction of the distortion a dislocation causes in the crystal lattice (THORSTEINSSON 1996). It can be distinguished between edge and screw dislocations: an edge dislocation is defined by having an additional plane of atoms in a part of the crystal. The plane is located perpendicular to the direction of basal glide, and moves horizontally (parallel to the basal plane) through the lattice (FOSSEN 2011, p.210). The *Burger's Vector* is perpendicular to the edge dislocation. Screw dislocations are parallel to the vector and can cross slip to another atomic plane. This dislocation occurs parallel to the direction of basal

glide, whereas the glide plane is perpendicular to the direction of the glide (FOSSEN 2011, p.210).

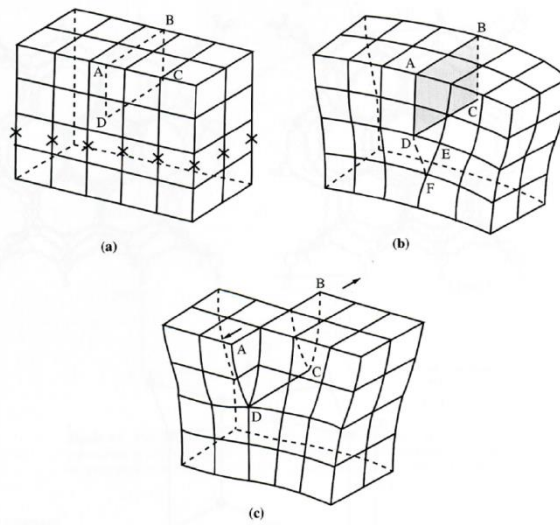


Fig. 3: (a) a crystal without dislocations, (b) edge dislocation, (c) screw dislocation (HOOKE 1995)

In natural crystals mostly mixed dislocation are to be found which hold features of both edge and screw dislocations.

In contrast to linear dislocations, point defects are characterized by excess protons occurring near the molecules. They only play a minor role during deformation. (SCHULSON & DUVAL 2009, p.9).

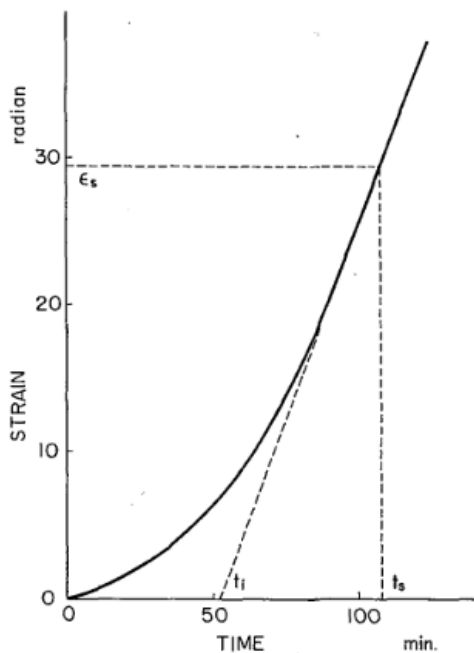


Fig. (4) shows the creep curve for a single crystal: it is a graph of strain rate against time (or strain) that is obtained when a constant stress is applied to a sample (CUFFEY & PATERSON 2010, p.52). The creep curve for a single crystal shows an increasing strain rate in the beginning that reaches a steady value after the crystal is deformed by 20 %. The initial increase is due to a fast multiplication of dislocations. When the dislocation density reaches a value that is in balance with the applied stress, a stationary strain rate is established (THORSTEINSSON 1996).

Fig. 4: A creep curve for a single crystal (THORSTEINSSON 1996)

Since natural ice is polycrystalline, fig. (5) provides a creep curve for the stages of creep of a polycrystal. At the beginning of deformation ice is isotropic, because c-axes are oriented randomly and thus do not favour basal glide (JACKA & JUN 2000). At high pressures flow properties are mainly determined by intracrystalline dislocation glide (DUVAL & MONTAGNAT 2000).

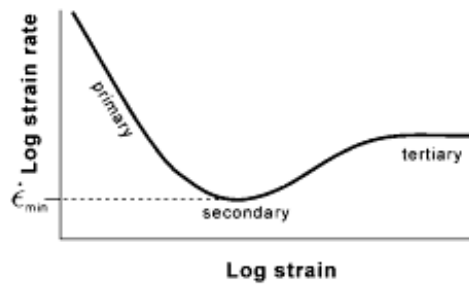


Fig. 5: A creep curve for polycrystalline ice (CUFFEY & PATERSON 2010)

After an initial state of (elastic) deformation (not shown in the curve) where molecules change the position in the lattice, the process of primary creep follows. It results in a deformation of those grains that show the favoured orientation for basal glide (PATERSON 1994). Some dislocations start to form and the creep rate decreases continuously since grains with different orientations impede each other. In the phase of secondary creep the creep rate reaches a minimum and remains constant, which might be due to a temporary balance between the softer and harder parts of the ice body (THORSTEINSSON 1996). It is followed by a stage of accelerated (tertiary) creep, where ice is anisotropic and the creep rate increases again eventually reaching a steady value if the applied stress continues (JACKA & JUN 2000). As recrystallization takes place, new grains favourably oriented for basal glide start to form (THORSTEINSSON 1996). The term recrystallization refers to any re-orientation of the lattice that is caused by grain boundary migration or the formation of new grain boundaries (FARIA ET AL. 2014b). During recrystallization, atoms escape from the crystal lattice on one side of the grain boundary and reattach to the lattice on the other side in order to minimize the free energy. By this process a grain boundary is able to move through the ice (CUFFEY & PATERSON 2010, p.36).

A recrystallization mechanism, that is active without any external stresses, is referred to as normal grain growth: it is driven by the differences in free energy due to the curvature of grain boundaries between the grains (ALLEY ET AL. 1986). The curvature causes a surface tension leading to differences in pressure, with higher pressure on the concave side, which is

the side of the smaller grain. To balance the difference, molecules tend to move from the side of the higher pressure to the side of the lower one so that the grain boundary migrates to the centre of the smaller grain. When the grain becomes smaller the process speeds up until the smaller grain is consumed by the larger one (ALLEY 1992). This almost linear increase occurs in stagnant ice as well as in the upper 400 to 700 m of an ice sheet where no mechanisms to form new grains are active (THORSTEINSSON 1996; CUFFEY & PATERSON 2010, p.36).

With increasing depth and thus increasing stress dynamic recrystallization occurs. This term summarizes the processes of polygonization (or rotation recrystallization (ALLEY 1992)), migration recrystallization and grain nucleation.

Since different parts of the grain can experience various stresses, grains are forced to bend or even twist which leads to an alignment of dislocations in configurations of lower energy (a planar wall), forming a subgrain boundary (or low-angle boundary) and later subdivides the grain (DUVAL & CASTELNAU 1995; CUFFEY & PATERSON 2010, p.42; THORSTEINSSON 1996); PATERSON 1991). Subgrain boundaries can develop to grain boundaries (high-angle boundaries) which show a misorientation to the neighbouring grain of about 3 to 5 ° (WEIKUSAT ET AL. 2010; WEIKUSAT ET AL. 2011). This process of the splitting of grains by forming new boundaries to reduce stress is referred to as polygonization and is observed in polar ice undergoing pure shear (CASTELNAU ET AL. 1996). In this regime, grain growth is still active but is counteracted by the subdivision process so that grain size remains nearly constant (THORSTEINSSON 1996). KIPFSTUHL ET AL. (2009) could provide evidence for dynamic recrystallization occurring in all depth of an ice sheet, although it is not the dominant process in the upper part.

The regime of migration recrystallization is observed in ice showing a critical temperature above -10 °C causing grain boundaries to move easily (DUVAL & CASTELNAU 1995). The process is defined as the nucleation and growth of entirely new grains by rapid migration of grain boundaries (THORSTEINSSON 1996; THORSTEINSSON ET AL. 1995). Deformation of a grain causes new dislocations to develop that interfere with the crystal lattice, thus increasing the stored energy. A different lattice strain energy between two neighbouring grains leads to a transfer of molecules from the higher energy grain to the lower energy one, which results in a migrating grain boundary and growth of the less strained grain at the expense of the high energy one. It can be distinguished from normal grain growth by the different driving force, which is here the strain energy rather than the curvature of the boundary (CUFFEY & PATERSON 2010, p.42).

In areas of high lattice distortion new grains can form with c-axes orientations favourable for basal glide and thus free of lattice strain energy. This process is referred to as grain nucleation. Older neighbouring grains with high strain energy can be consumed by those new grains by migration recrystallization. In ice sheets these processes are active in the deeper layers, where high stresses and increased temperatures occur. Generally, the size of the grains depends on the rates of nucleation and boundary migration: the more rapid the nucleation relative to the migration recrystallization, the smaller the average grain (CUFFEY & PATERSON 2010, p.42).

Polygonization usually has little effect on the c-axis orientation fabric (the change is in the order of the minimum angle difference defining a grain boundary), in contrast to migration recrystallization and nucleation that alter it significantly (CUFFEY & PATERSON 2010, p.42).

The statistically preferred orientation of the crystal lattices of a population of grains is referred to c-axis fabric or simply fabric (FARIA ET AL. 2014b; PATERSON 1994).

These fabrics can be plotted in a Schmidt diagram: in polycrystalline ice, the c-axis of each crystal points in a direction of a unit vector c . The ensemble of those vectors is plotted as dots in a Schmidt diagram which represents the surface on a hemisphere on an equal-area projection. The c-axis is imagined to pass through the centre of the sphere and intersecting with the surface of the lower hemisphere. Every dot marks this intersection of the axis with the sphere. As a consequence of strain, certain fabrics develop that provide information about the deformation history and rheological properties of the ice sheet (ALLEY 1988; CUFFEY & PATERSON 2010, p.33).

In the upper layers of an ice sheet, c-axis orientations generally show a random distribution. With increasing depth and under higher stresses, an orientation pattern of the c-axes develops (ALLEY 1988). Fig. (6) shows the patterns arising from

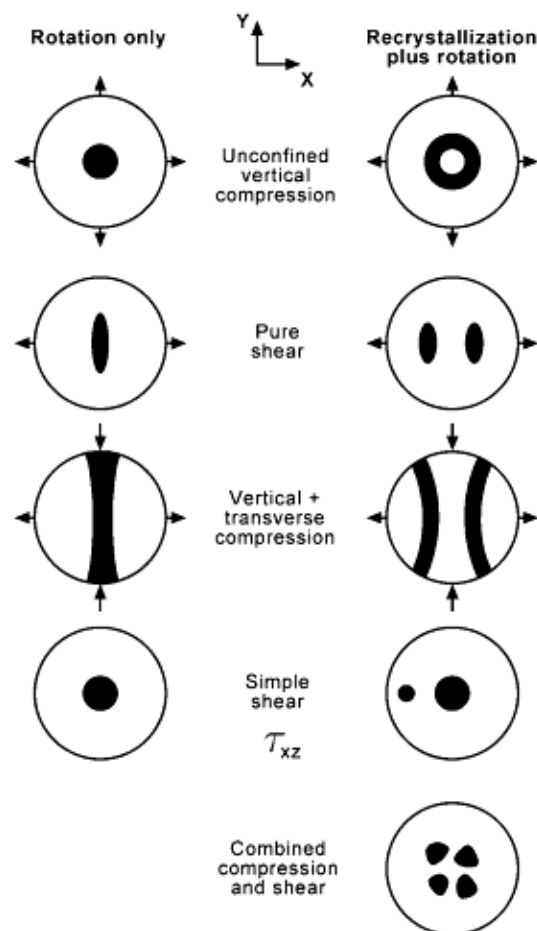


Fig. 6: C-axis fabrics produced in simple stress systems by rotation and rotation accompanied by recrystallization (CUFFEY & PATERSON 2010)

different types of deformation. A single maximum develops if vertical compression (pure shear, e.g. in an ice dome) or simple shear occurs and the c-axes rotate towards the axis of compression (THORSTEINSSON 1996; ALLEY 1992).

A single maximum is common in the middle of an ice sheet and is expected to develop mainly from rotation recrystallization and polygonization (CUFFEY & PATERSON 2010, p.46). Fabrics with multiple maxima can often be observed in temperate glaciers (VALLON ET AL. 1976). If extensional forces occur and the ice enters the regime of migration recrystallization, a girdle fabric will develop, where c-axes rotate away from the direction of extension and tend to distribute evenly in a plane perpendicular to that direction (THORSTEINSSON 1996). Samples from ice cores drilled at ice divides, where the ice flows in two different directions, show a girdle fabric. Depending on stresses applied to the ice also mixed patterns are possible.

For a better description of the fabrics, a second order orientation tensor is used. As with the Schmidt diagram, the c-axis is imagined to pass through the centre of a sphere diagram and every point of intersection with the surface is considered to have a mass $m=1$. If the sphere rotates around the centre of an arbitrary axis, kinetic energy referred to as moment of inertia will be required to start the rotation. The moment of inertia is defined as $M=m*a^2$, whereas m is the mass of the particle and a the distance perpendicular to the axis of rotation (WALLBRECHER 1986, p.157).

Finding the rotation axis resulting in the minimum and maximum moment of inertia, one receives two directions which can define the position of the c-axes in the sphere already well (WALLBRECHER 1986, p.159). The eigenvectors λ_1 and λ_2 are related to these directions with the third eigenvector λ_3 perpendicular to them. The corresponding eigenvalues are the norms of the eigenvectors, whereas for the normalized orientation tensor counts:

$$E_1 < E_2 < E_3$$

(THORSTEINSSON 1996; EISEN 2007).

The directions of the eigenvectors form a Cartesian coordinate system. The axis with the maximum moment of inertia is related to the lowest eigenvalue E_1 and the axis with the minimum moment of inertia corresponds to the highest eigenvalue E_3 (WALLBRECHER 1986). The three eigenvectors span the surface of an ellipsoid, the distribution of the c-axes is reflected in the ratios of the eigenvalues (SURMA 2011).

Optical properties

To measure c-axis orientations in polycrystalline ice, it is necessary to focus on the optical properties of ice. Since ice crystals show a hexagonal structure, ice belongs to the optical anisotropic minerals which typically feature a weak birefringence: when light enters an anisotropic mineral, the ray is separated into two transversal waves that travel perpendicular to each other and propagate with different velocities. The two waves are referred to as “ordinary” and “extraordinary” waves (MÜLLER & RAITH 1993, p.67). Since the refractive index in the direction of the extraordinary wave is larger the refractive index in the direction of the ordinary one, the material is said to have a positive birefringence (PETRENKO & WHITWORTH 1999, p.219). In the direction parallel to the c-axis just one wave is propagating whereas in all of the other directions two waves with different refractive indices occur. Thus, ice is considered to be optically uniaxial (MÜLLER & RAITH 1993). Perpendicular to the c-axis, the largest birefringence is observed (PETRENKO & WHITWORTH 1999).

The measuring of c-axis orientations is described in detail in chapter 5.1.

3.4 Impurities

3.4.1 Sources, transport and deposition

Impurities in ice can provide essential information about the climatic conditions in their source areas as well as about former atmospheric circulation patterns (RUTH 2002). Additionally, the analysis of those particles can help to understand the physical properties of ice (DELLA LUNGA ET AL. 2014; REMPEL ET AL. 2001; REMPEL ET AL. 2002).

Mostly they are referred to as aerosols which are smallest particles being suspended in the atmosphere (RUTH 2002) whereas a differentiation between soluble and insoluble components can be made. Soluble particles are of marine, terrestrial or biogenic origin (e.g. Na^+ , K^+ or NH^+) (LEGRAND & DELMAS 1988) while insoluble compounds mostly originate from terrestrial sources and are referred to as “dust” (DELLA LUNGA ET AL. 2014; REMPEL ET AL. 2001; REMPEL ET AL. 2002).

Due to chemical and physical weathering processes in arid and semiarid areas, fine-grained and loose material is provided which will be eroded if appropriate wind speeds occur and transported to the atmosphere via convective cells (RUTH 2002; FISCHER ET AL. 2007). Particles with a diameter less than 0.5 mm do not reach the atmosphere but can be rolled over the ground (surface creep or reptation) whereas particles with a diameter from 0.05 to 0.5 mm

can be shortly lifted up and thus, resulting in a transfer of kinetic energy to jolted neighbouring particles when they reach the ground again (saltation, see fig. 7) (RUTH 2002; FISCHER ET AL. 2007). Generally, 50 to 80 % of the particles are moved by saltation (RUTH 2002). 1 % of the particles can remain in suspension in the atmosphere due to their very small diameter of less than 0.05 mm (RUTH 2002, WEIBBACH 2011) (see fig. 7).

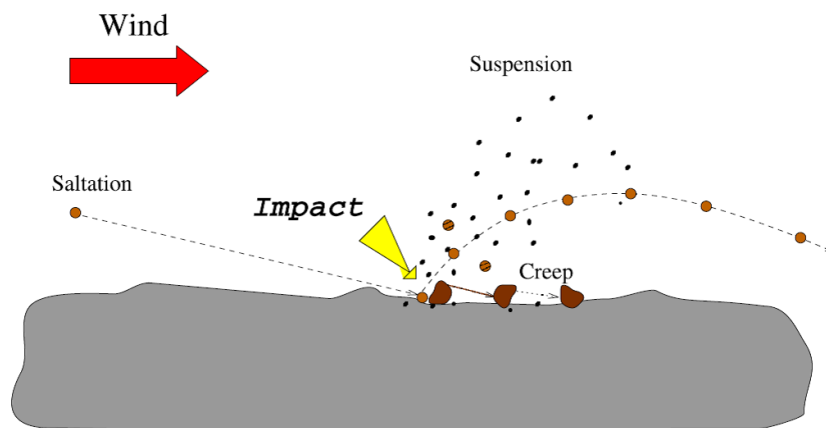


Fig. 7: Transport mechanisms of dust particles (RUTH 2002 (from HUA 1999))

Aerosols can stay in the stratosphere (more than 10 km in height) up to one year while they remain in the upper troposphere (3 to 10 km high) not longer than a month and in the lower troposphere (up to 3 km in height) just some days to few weeks (BARRIE 1985). A long range transport is only possible in the planetary layer where the material can be transported to via high wind speeds in convective cells. On the northern hemisphere zonal transport is realized in the area of the westerly winds (Jetstream), meridional transport occurs due to the low-pressure areas (cyclones) developing along the polar front (RUTH 2002). During the last glacial the polar front was shifted southwards leading to a higher gradient in temperatures between the arctic and the tropics thus resulting in a higher activity of cyclones that were reaching towards the equator (RUTH 2002, FISCHER ET AL. 2007).

Regarding the deposition, one can distinguish between wet and dry deposition. Wet deposition is related to precipitation and thus directly proportional to snow accumulation (FISCHER ET AL. 2007). Aerosols can act as cloud condensation nuclei (CCN) and rain out with the precipitation. 80 % of the precipitation condensate through aerosols (BARNES & WOLFF 2004), although the majority of the particles is attached to the snowflakes without acting as a condensation nuclei (FISCHER ET AL. 2007). Particles can also be washed out with the falling precipitation in case they remain in suspension below the clouds (RUTH 2002).

Dry deposition is independent from precipitation (FISCHER ET AL. 2007) and occurs mostly at low accumulation rates and in spring when a lot of particles accumulate in the atmosphere (HUTTERLI ET AL. 2006). During dry deposition the sedimentation of big aerosols ($>10 \mu\text{m}$) is of importance and particles can reach the snow surface via simple attachment or impaction (BARRIE 1985).

Generally, changes in the concentration of impurities in ice do not directly correspond to changes in the concentration in the atmosphere which is due to the length and kind of transport as well as due to post depositional processes (FUHRER ET AL. 1993). Deposition of gaseous species (e.g. H_2O_2) is reversible whereas aerosols (e.g. Ca^{2+} , NH_4^+) are irreversibly attached to the snow surface and thus are stationary in the ice. After the deposition, macroscale processes can alter the composition at the surface: high wind speeds can lead to a drift of material at the surface so that dunes can develop which might destroy the annual layering (DIBB ET AL. 1992, FUHRER ET AL. 1993).

3.4.2 Impurities in the Greenland ice sheet

This chapter deals with the impurities to be found in the Greenland ice explaining their seasonal variability and possible sources. The main focus is on those species (e.g. Ca^{2+} , Na^+) that were included in the calculation of the correlation coefficient and could be identified with Raman spectroscopy in the progress of this thesis (see chapter 6).

The snow falling over Greenland generally contains low amounts of impurities, since most of them have been removed already by precipitation during their transport from the evaporation sources to the Arctic (DELLA LUNGA ET AL. 2014).

The transport of dust is influenced by the southward shift of the polar front during cold stages which leads to increased atmospheric circulation intensities as well as by the monsoon cycles in its source areas (RUTH 2002; BISCAYE ET AL. 1997). Furthermore, a decreased atmospheric moisture level causes fewer washouts of particles during their transport to Greenland (FUHRER ET AL. 1999, YUNG ET AL. 1996). The mid-Asian deserts, especially the Taklamakan desert in West China, could be identified as the main source of dust in the Greenland ice sheet (BORY ET AL. 2003).

In Greenland, the insoluble components of dust are composed of crustal minerals, mainly containing aluminosilicates (PALAIS ET AL. 1990). In samples from the GRIP (Greenland Ice Core Project) ice core, LAJ ET AL. (1997) found a high amount of quartz particles during cold stages in contrast to clay minerals and mica occurring more during warm periods. The content

of insoluble calcium particles (mainly apatite and plagioclase) remained very low. Calcium carbonates and gypsum represent the biggest share of the soluble fraction (see chapter 3.4.1) (LAJ ET AL. 1997) so that calcium (Ca^{2+}) can be used as a proxy for dust since both components show the same seasonality (RUTH ET AL. 2003). Calcium concentrations in Greenland reach a maximum in spring, since most of the snow cover in the source areas is already molten but there is still not enough vegetation regrown to prevent erosion (FISCHER & WAGENBACH 1996). Generally, dust concentrations in glacial times are about 10 to 100 times higher than in the Holocene (STEFFENSEN 1997).

Furthermore, components of sea salt are transported to the ice sheet. Oceans cover about 71 % of the earth's surface so that sea spray aerosols (SSA) are the largest source of aerosols in the atmosphere (LEWIS & SCHWARTZ 2004; AULT ET AL. 2013). SSA particles are mainly composed of sodium (Na^+), chloride (Cl^-), and to some extent also magnesium (Mg^+) and calcium (Ca^+) (FISCHER ET AL. 2007). At high wind speeds small air bubbles burst at the ocean surface producing small droplets that can be transported to the boundary layer via convective cells (FISCHER ET AL. 2007; OHNO ET AL. 2005). Since the atmospheric turbulences (storm activity) increases in winter, the amount of sea salt shows a maximum in winter to early spring (KURAMOTO ET AL. 2011).

Another important fraction of the impurities in the ice are nitrogen compounds whereas especially nitrate (NO_3^-) and ammonium (NH_4^+) are of interest for this thesis.

The seasonal cycle for nitrogen compounds are weaker than for example dust but still NH_4^+ and NO_3^- can be said to have their maxima in spring to summer (ANDERSEN ET AL. 2006). Both compounds can be connected to processes of bacterial decomposition which occur mainly during warmer periods of the year (KURAMOTO ET AL. 2011). Recent firn samples also show increasing concentrations of nitrate (NO_3^-) in winter to early spring which are thought to be caused by anthropogenic emissions (FISCHER ET AL. 1998; KURAMOTO ET AL. 2011).

LEGRAND ET AL. (1992) also explains that ammonium is a proxy for forest fires. Samples from Summit ice core, Greenland, show high ammonium peaks which must be caused by a high intensity source that emits ammonium on a time scale of days to a month. They came to the conclusion that only forest fires have enough energy to extend in the upper troposphere where a transport over large distances is possible. Still the amount of ammonium derived from wildfires might be less than 5 % (SEILER & CRUTZEN 1980). Since DANSGAARD ET AL. (1993) point out that the circulation pattern in the northern hemisphere did not changed significantly during the last 10,000 years, the Siberian boreal forests can be determined as a source for wildfire emissions (FUHRER ET AL. 1996, STOHL 2006).

Boreal fires occur during summertime when high temperatures combined with reduced precipitation and high fuel availability due to increased plant productivity allows combustion (ZENNARO ET AL. 2014; PYNE 2001). Plumes from those fires can circle the entire northern hemisphere and are an important source of air pollutant throughout the Arctic (LAVOUÉ ET AL. 2000; DAMOAH ET AL. 2004). Besides ammonium, the black carbon (BC) contributes to a large extend to wildfire emission. It is emitted during incomplete combustion of fossil and biofuels in fires from both natural and human sources (MCCONNELL ET AL. 2007) and has a short atmospheric lifetime of 6 ± 2 days (PARK ET AL. 2005). BC is not a single chemical compound and lacks well-defined characteristics (MASIELLO 2004; ZENNARO ET AL. 2014). The μm -sized BC particles may also accumulate and coat other impurities (SCHWARTZ ET AL. 2008).

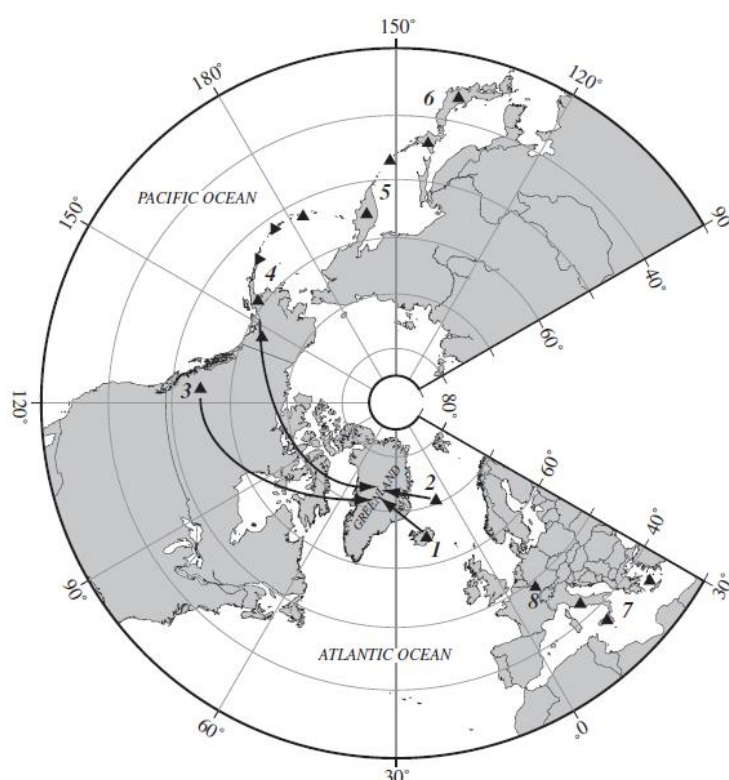


Fig. 8: Volcanic regions contributing tephra deposits to the Greenland ice-core records (1-Iceland, 2-Jan Mayen, 3-North America, 4-Alaska) (ABBOTT & DAVIES 2012)

For example sulphur compounds might be a species occurring together with BC. During meltwater analysis mostly sulfate (SO_4^{2-}) concentrations are detected, since sulfate is a dominant contaminant of precipitation. It can originate from human activity, biological decay or volcanic emissions (DELMAS & BOUTRON 1977). During glacial times, sulphur is mostly

not of biogenic origin but can primarily derive from volcanic tephra (LAJ ET AL. 1997). Tephra is a collective term for all volcanic ejecta and unconsolidated deposits arising from pyroclastic currents and fallout deposits (LOWE 2011). The ash components can be ejected high into the atmosphere and distributed over a wide geographical area due to the interaction of magma and water which increases the explosivity of basaltic eruptions (see fig. 8) (ABBOTT & DAVIES 2012; ÓLADÓTTIR ET AL. 2008). An increased concentration of sulfate can be measured up to two years after an eruption (FISCHER 2001). Still, dating remains difficult since the particles originating from volcanic eruptions are transported and it can take years until they are deposited at the poles. Greenland deep ice cores preserve a tephra record for the past 123,000 years including 45 different volcanic events (ABBOTT & DAVIES 2012) and most of them are determined to be of Icelandic origin (ÓLADÓTTIR ET AL. 2008).

3.4.3 Location of impurities

As described in the previous chapter, the major part of the remaining impurities in the Greenland ice sheet are insoluble microparticles of terrestrial origin, sea salt aerosols and acids. Their location and distribution within the ice polycrystal depend on the mode of incorporation into the snowflakes or ice crystals and on subsequent processes that occur during recrystallization (WOLFF ET AL. 1988).

Generally, it is assumed that very few impurities dissolve in ice, as even most of the impurities that are easily dissolved in water are rejected as the water freezes. A few acids, ammonia and some alkalis and their derivatives might be exceptions (PETRENKO & WHITWORTH 1994). Since the atomic radii of fluorine and nitrogen are similar to the atomic radius of oxygen, it is assumed that fluoride (F^-), hydrogen fluoride (HF), chloride (Cl^-) and ammonia (NH_4^+ and NH_3) are able to replace water molecules and thus go into the lattice (HOBBS 1974, p. 112). Additionally, experiments with doped ice have shown that hydrogen chloride (HCl) and hydrogen bromide (HBr) might be substitutionally incorporated into the crystal (HOBBS 1974, p.112; BARNES & WOLFF 2004). Once the impurities are incorporated they drastically change the protonic carrier concentration and cause defects in the structure (PETRENKO & WHITWORTH 1994).

For some small molecules (e.g. HCl or partly H_2SO_4) it can be also possible to be situated in the free spaces between the molecules of the lattice since the ice crystal features a relatively open structure (PATERSON 1994, p.88).

Still, most of the impurities are considered to be too large to go into the lattice (REMPEL ET AL. 2001). Insoluble particles (dust) can be located in the bulk of the grain as well as in ripple junctions or grain boundaries, where they prefer to be located, since they will produce strain in the lattice due to their different structure (WOLFF ET AL. 1988). In comparison to lattice, the grain boundary is an amorphous or disordered area so that lower strain energy is achieved when the impurity is forced into the grain boundary (ALLEY ET AL. 1986, OHNO ET AL. 2005). In temperate ice grain boundaries can include a liquid phase (BLACKFORD 2007). This continuous network of microscopic channels remains liquid at subzero temperatures so that it can act as an alternative route for diffusive transport (REMPEL ET AL. 2001). This process is very effective in small grained ice since there are more potential pathways (FARIA ET AL. 2010).

Using Raman spectroscopy, FUKAZAWA ET AL. (1998) could identify sulfate and nitrate ions in the liquid phase of grain boundaries and triple junctions in Antarctic ice. They did not observe Raman peaks associated with molecular ions in grain interiors, indicating that the grains are impurity free (FUKAZAWA ET AL. 1998, BARLETTA ET AL. 2012). Additionally, BAKER & CULLEN (2000, 2001, 2003) found impurities concentrated in filaments with a diameter of about 1 μm in grain boundaries. Although they concluded these filaments to be artefacts produced by sample sublimation, they demonstrate the presence of impurities that are segregated along grain boundaries (DELLA LUNGA ET AL. 2014). The substances they identified comprised sulphur, chloride, magnesium and sodium, which are typical for atmospherically derived impurities (BAKER & CULLEN 2000; BAKER & CULLEN 2001; BARNES 2002).

However, BAKER & CULLEN (2000, 2001) state, that the majority of the particles are not trapped in grain boundaries or triple junctions. Microparticles at nano- to micrometer scale that are not partitioned to the grain boundaries but remain in the bulk of the ice crystal are referred to as “black dots” (see chapter 6.3). Solid-state diffusion through single ice grains is extremely slow so that impurities considered to be frozen in place (REMPEL ET AL. 2001).

Generally, there is a wide range of locations for impurities while their distribution processes, to a large extent, remain unclear. Their influences on the ice microstructure with respect to their location are discussed in the following chapter.

3.4.4 Influences on the physical properties

In general, it is assumed that impurities and dust change the mechanical properties of ice. The origin of this assumption is that ice deposited during glacials shows smaller crystals, a stronger fabric, and at the same time higher concentrations of soluble and insoluble impurities than ice from Holocene (PATERSON 1991). Experiments on doped ice have shown that impurities have an influence on the ductility of ice and thus might change the processes of densification and creep. One example is given by HÖRHOLD ET AL. (2012), who found a positive correlation between the Ca^{2+} concentration signal and density in Greenland ice cores, suggesting that high impurity concentrations lead to a softening of the firn and thus accelerated densification. They state, that impurities can affect densification and control the variability of density. They might change the character of firn layering from deposition-dominated density layering in the upper firn to impurity-dominated density layering in deeper firn. Furthermore, HÖRHOLD ET AL. (2012) could determine that seasonal cycles in density, which follows seasonal cycles of Ca^{2+} .

Particles that gather at grain boundaries can interact with them e.g. slow down their migration. When the velocity of the moving grain boundary (of grain growth) is not high enough to separate from extrinsic material (impurities), the velocity of the grain boundary is influenced by the extrinsic material. This leads to a pinning effect: the grain boundary is pinned by the particle and thus moves at a slower velocity. It resides in a low-velocity regime (ALLEY ET AL. 1986). Basically, temperature and strain rate (dislocation density) influence the migration velocity. If the velocity of the migrating grain boundary is high enough, it will separate from extrinsic material so that an unpinning effect occurs and the grain boundary changes to the high-velocity regime. Generally it migrates faster when it is separated from the impurities (ALLEY ET AL. 1986; THORSTEINSSON 1996). Still, ALLEY & WOODS (1996) and ALLEY ET AL. (1986) state that impurity concentrations even in ice age ice are too low to impede grain boundary migration and grain growth, only concentrations as they occur in layers close to the bedrock and layers containing volcanic ash might be sufficiently high.

Generally, it is assumed that nano- to micro-sized particles can interact with grain boundaries as material from the crystal lattice has to diffuse around the particle and the larger the particle on the boundary the more material has to be moved. Furthermore, temperature determines the velocity of the migrating boundary, since higher temperatures result in an accelerated diffusion (FARIA ET AL. 2010). Also other properties of the boundary might be of importance (DASH ET AL. 1995). Based on observations using optical microscopy FARIA ET AL. (2010)

state that there is no interaction between grain boundaries and inclusions down to a depth of about 2400 m. Samples from the Antarctic EPICA DML core show that below this depth, grain boundaries contain a high concentration of impurities. They even seem to harvest those inclusions which might be due to changes in the internal structure of the grain boundaries (the grain boundaries become “sticky”) in response to an increase in temperature.

Furthermore, impurities can act as obstacles for dislocations, which can be pinned and thus kept in place by two particles (HOOKE 1998). When particles block the movement of dislocations they can increase dislocation density as well as the stored energy and the recrystallization rate (PATERSON 1991). Experiments on doped ice have shown that already small amount of hydrogen fluoride (HF) can soften the crystal due to an increased number of point defects (JONES & GLEN 1968).

4. Samples and drilling site

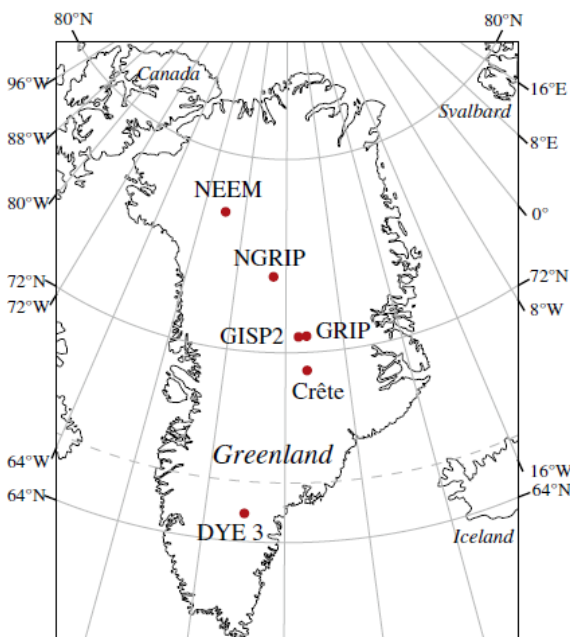


Fig. 9: Location map for Greenland ice-core drill sites (ABBOTT & DAVIES 2012)

The drilling location for the NEEM-ice core is situated in the northwestern part of Greenland (77,45 °N; 50,06 °W). The ice at the drill site is around 2542 m thick and the Eemian ice can be found at depths between 2265 m and 2345 m (NEEM COMMUNITY MEMBERS 2013). The annual layers at that depth should be around 7mm thick (RASMUSSEN ET AL. 2013).

The location (see fig. 9) was investigated with radar techniques and had to fulfill certain criteria: firstly, the ice should be thick enough to guarantee that the ice is old enough to include the Eemian layer. Secondly, the bedrock should be flat so that the layering is not disturbed by an irregular ice flow due to unevenness at the ground. Third, the site should be located on an ice divide which is the line that separated the east-flowing part from the west-flowing part and the area where usually the oldest layers can be found. Finally, the precipitation should be moderately high, because a large annual snow fall causes fast thinning of the lower, older layers (http://neem.dk/about_neem/). The present day annual snow accumulation at NEEM

site is 0,22 m ice equivalent, which is similar to those of the GRIP and GISP ice cores. The sample used for the case study in this thesis (bag 1346) originates from a depth of about 740 m, where the annual layers have a thickness between 12 and 16 cm. It is ice deposited during the Holocene, as it is ca. 4000 years old (RASMUSSEN ET AL. 2013).

5. Methods

5.1 Microstructure measurements

The thin sections used to determine c-axis orientations were measured in the field directly after drilling in order to minimize relaxation effects. At first, the core is cut into approximately 55 cm long pieces, the so called “bags” which are subsequently divided for further analysis. For the preparation of thin sections one bag is separated into 6 sections, each of them about 6 cm long and 7 cm wide, while 2 to 3 cm of loss can occur due to cutting. The sample is glued with water to the object plate and microtomed down to approximately 300 to 250 μm in thickness (see fig. 10). Giving the sample some time to sublimate will make the grain boundaries more visible and thus easier to distinguish (KIPFSTUHL ET AL. 2006).



Fig. 10: A microtome used for the preparation of thin sections (KLEITZ 2013)

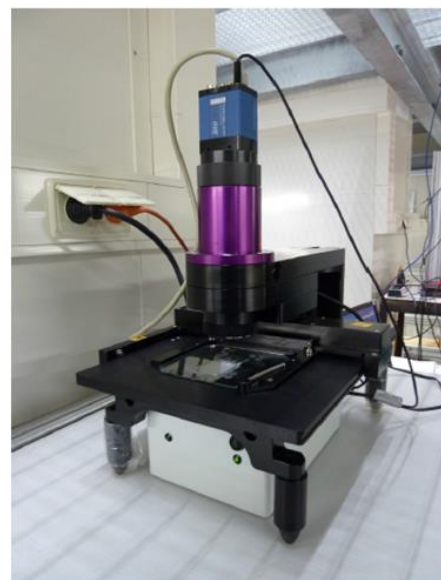


Fig.11: The Fabric Analyzer (TAMMEN 2012)

The prepared thin section can be measured with the Fabric Analyzer to determine c-axis orientations in the sample (see fig. 11). With a Fabric Analyzer c-axis orientations of optical uniaxial minerals, such as ice, quartz or calcite can be measured, although the device is limited to minerals with a hexagonal or trigonal crystal structure and cannot determine the complete crystallographic orientation (PETERNELL ET AL. 2010).

The main parts of the device are a light source, a microscope stage, two polarizers, a $\lambda/4$ retarder plate (another special polarizer), an objective lens and a CCD camera. The light source is provided by one LED mounted perpendicular to the sample and another eight LED's that are oriented ca 12° from the vertical and arranged at 45° to one another in order to focus a conical light beam on the sample. Crossed polarizers can be rotated synchronously around the stationary microscope stage with the thin section between 0 and 90° in steps of $11,25^\circ$. The camera captures images for each LED so that pictures with the crossed polarizers, for the retarder plate and for the polarized light between 0 and 90° are taken (WILSON ET AL. 2007, PETERNELL ET AL. 2009, TAMMEN 2012). For every picture, the layer in which the c-axis is located and the angle of extinction of every c-axis can be determined.

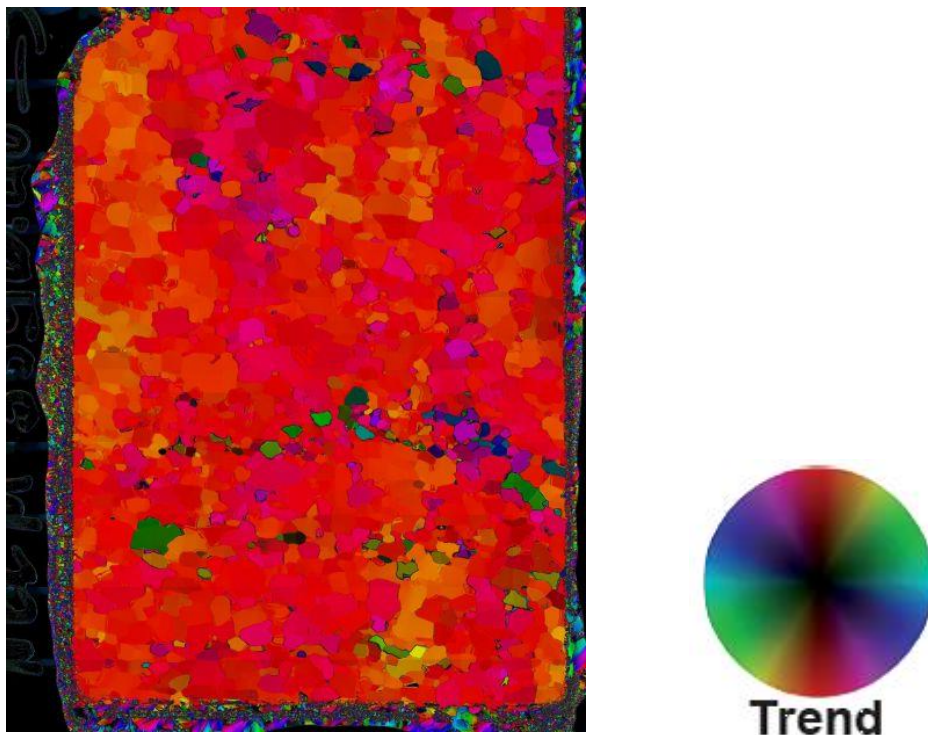


Fig. 12: After data processing a trend image can be obtained (right), where the red areas show a c-axis parallel to the longitudinal axis of the ice core (Trend, left) (WEIKUSAT & KIPFSTUHL 2010; MONTAGNAT ET AL. 2014)

By Using Fourier Transformation, the angle of extinction can be calculated by fitting the light amplitude values for each step of the polarizers to a sinusoid curve (PETERNELL ET AL. 2009). By combining all 9 layers (or planes), an intersection line can be obtained which is related to the c-axis orientation. Using the angles of the azimuth, which defines the deviation from the longitudinal axis of the ice core ($0^\circ \leq \text{azi.} \leq 360^\circ$) and the colatitude (the deviation from the normal to the longitudinal axis of the core, $0 \leq \text{colatitude} \leq 90^\circ$), the c-axis orientation can be determined for every pixel (see fig. 12) (PETERNELL ET AL. 2009, TAMMEN 2012).

5.2 Chemical parameters

For measuring concentrations of major ions and dust particles in ice cores, systems for continuous flow analysis (CFA) became a standard method in ice core analysis due to the fast and efficient decontamination of the samples and the high temporal data resolution that can be obtained over the full length of an ice core (KAUFMANN ET AL. 2008; BIGLER ET AL. 2007).

The samples from the NEEM ice core used for this work were directly measured in the field. In the following, the main setup for a CFA system for a stationary lab is described.

Sample preparation and melting is performed in a cold laboratory at approximately -10 to -20°C . A longitudinal subsection is cut from an ice core (an ice core “stick”) which usually has a cross section of about $3.5\text{ cm} \times 3.5\text{ cm}$ and measures around 100 cm in length (COLE-DAI ET AL. 2006) and breaks in the core should be documented seriously. All working surfaces have to be decontaminated (e.g. with Isopropanol) to guarantee good working conditions for low level measurements. As the breaks and also the ends of the stick are sources of contamination, it is necessary to take off some millimeters at the edges of the core (RUTH ET AL. 2003). The prepared stick is fixed in an open-ended aluminum tray and mounted over a melt head so that it can melt at one end (RÖTHLISBERGER ET AL. 2000; KAUFMANN ET AL. 2008). For firn cores the melt head is usually made from aluminum, for ice cores it is coated with



Fig. 13: A firn core before the melting process starts (CFA system of the Alfred-Wegener-Institute for Polar and Marine Research) (KLEITZ 2013)

gold. The melt head consists of two concentric parts: a 2,5 cm square inner zone inside a 4,0 cm square melt area. Since the cross section of the sample is slightly larger than the inner zone, the potentially contaminated melt water from the outer zone can be channeled separately to the waste stream thus providing decontamination (COLE-DAI ET AL. 2006; MCCONNELL ET AL. 2002). Only the stream of the inner part which was never in contact with ambient air is drained off for further sample analysis (BIGLER ET AL. 2007). Fig. (13) shows the melt head for firm of the CFA system owned by the Alfred-Wegener-Institut for Polar and Marine Research, Bremerhaven. The analysis of firm samples is slightly difficult since the capillary forces in the porous firm result in meltwater which is soaked up into layers above the melt head. Thus, a firm-melt head consists of a flat surface with many radial narrow slits that cause a capillary force downward into the melter, which is higher than the one of the porous firm (RÖTHLISBERGER ET AL. 2000). The melt head is usually kept at a temperature of about 20 °C to maintain a constant melt rate of typically 3,5 cm/min. A weight lying upon the ice sample applies additional pressure on the ice to keep a constant melt speed also towards the end of the measurement, where the net weight of the stack gets lower (KAUFMANN ET AL. 2008). A peristaltic pump ensures the flow in the sample stream and the meltwater is channeled via plastic tubes to the warm laboratory that is located in the adjacent room operating under normal room temperature (COLE-DAI ET AL. 2006). The meltwater naturally contains air bubbles coming from the enclosed air in the ice, which accounts for approximately 10 % of the volume so that the water first passes a debubbler preventing any air bubbles entering the following system (KAUFMANN ET AL. 2008; RUTH ET AL. 2003). After that, an automated set of valves determines whether meltwater from the sample or standard calibration solutions are measured and divides the sample stream to the different plastic tubes leading to the measuring devices and to the waste bin (see fig. 14) (RÖTHLISBERGER ET AL. 2000). The measuring device can include a conductivity meter, a pH meter and several components to measure the major ions such as Ca^{2+} , Na^+ , NH_4^+ , NO_3^- , SO_4^{2-} or H_2O^2 (COLE-DAI ET AL. 2006). Table (1) summarizes the measuring principles for the major ions.

Tab. 1: The chemical species and the main principles of their measuring methods

Chemical species	Method	Reference
Ca^{2+}	- measuring the intensity of fluorescent complexes	SIGG ET AL. 1994; RUTH ET AL. 2007
Na^+	- Absorption	RÖTHLISBERGER ET AL. 2000
NH_4^+	- measuring the intensity of fluorescent complexes	SIGG ET AL. 1994
NO_3^-	- Absorption	RÖTHLISBERGER ET AL. 2000
SO_4^{2-}	- optical	MADSEN & MURPHY 1981; BIGLER ET AL. 2002; BIGLER ET AL. 2007; BURAKHAM ET AL. 2004
H_2O_2	- measuring the intensity of fluorescent complexes	SIGG ET AL. 1994
Dust (insoluble particles)	- optical	KAUFMANN ET AL. 2008

After the measurements, uncontaminated sample water is collected in vials by an autosampler for subsequent discrete analysis (WOLFF ET AL. 2006; KAUFMANN ET AL. 2008).

With a CFA system (see fig. 14) a recorded resolution of about 1 mm should be achieved while the effective resolution is between 10 and 25 mm (ANDERSEN ET AL. 2006; RASMUSSEN ET AL. 2006). The depth resolution is defined as the core depth interval represented by a single analytical measurement and is mainly influenced by the turbulent mixing that takes place in the long tubes of the system and the geometry of the melting device (SIGG ET AL. 1994; RASMUSSEN ET AL. 2005; COLE-DAI ET AL. 2006).

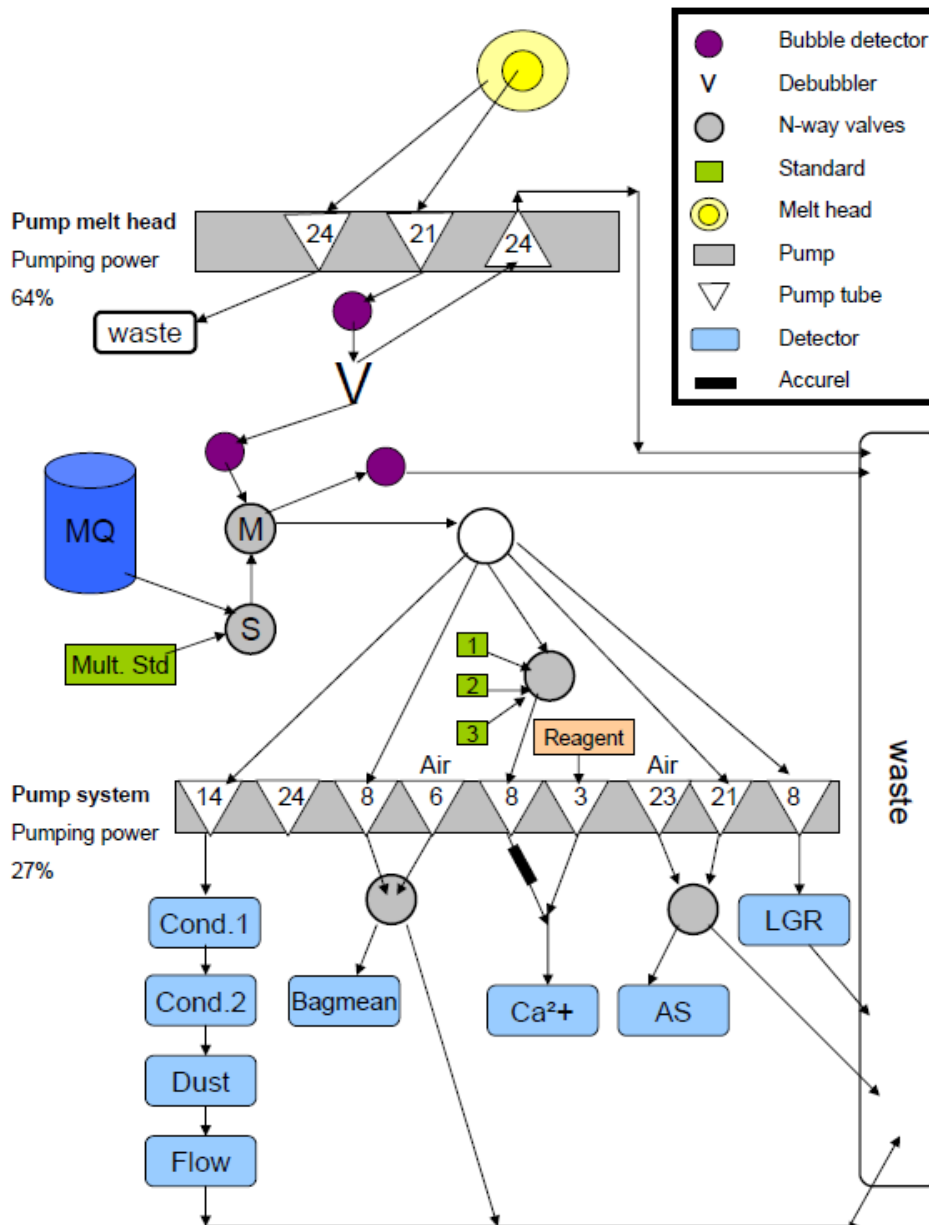


Fig. 14: Schematic drawing of a CFA system (WEIBBACH, personal communication 2015)

5.3 Linescan images

To identify layers of high impurity concentrations (cloudy bands), linescan images can be an appropriate method. Cloudy bands develop when seasonal events lead to an increased transport and deposition of impurities onto the ice shield (SVENSSON ET AL. 2005; DELLA LUNGA ET AL. 2014).

For sample preparation, the ice core slabs have to be carefully microtomed on both sides. The measuring principle is comparable to dark field microscopy. The main setup the shown in fig. (15): above and below the ice core section two trolleys are located holding an indirect light source and a camera, which can measure light intensities in 8 bit resolution. The trolleys move synchronously along the sample while the camera records the light that is scattered in the ice. The images have a resolution of 118 pixel/cm, bright layers of intense cloudy bands and volcanic ash can be identified due to the light scattering of the particles (SVENSSON ET AL. 2005). Since pure ice does not contain high amounts of impurities, it will appear dark in the images (SVENSSON ET AL. 2005; DELLA LUNGA ET AL. 2014).

For this work, not all samples have been scanned due to the fact that the ice originates from the brittle zone (e.g. NEFF 2014), which makes sample preparation difficult.

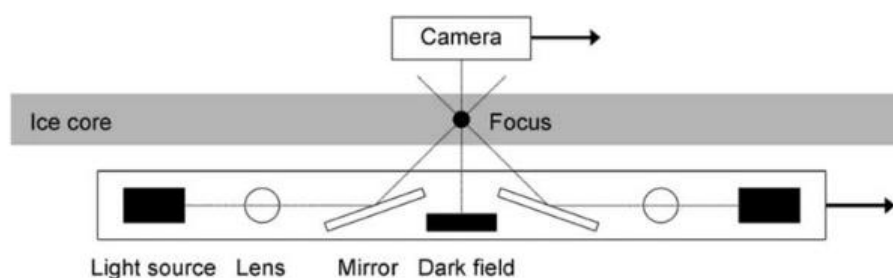


Fig. 15: Schematic drawing demonstrating the principle of a linescan instrument (SVENSSON ET AL. 2005)

5.4 Microstructure mapping

For further investigations two sections from one bag are chosen as a case study (see chapter 6.3 and 6.4) for which the method of microstructure mapping was used as described by KIPFSTUHL ET AL. (2006). For the chosen samples a full overview of all microstructure features is necessary to identify the black dots to be measured with Raman spectroscopy as well as to get a first impression about their distribution.

The samples are usually vertical sections with the long axis parallel to the vertical axis of the ice core, and are approximately 90 to 110 mm long, 40 to 50 mm wide and 4 to 5 mm thick (see chapter 7.6, fig. 39). They are prepared according to the standard procedure for the production of thin sections for fabric analysis: for this work, an approximately 20 mm wide and 90 mm long area in the middle of the convex side of the sample was microtomed, then the

sample was frozen with the microtomed side on a glass plate to prepare the surface on the other side. After that procedure the sample sublimated for about one hour so that the scratches produced by the microtome blade disappear and the subgrain and grain boundaries become more visible.

The system used at the Alfred-Wegener-Institute consists of an optical microscope (Leica DMLM), a CCD camera, a frame grabber and an xy-stage. The images are taken in transmission and acquired in grey value with a resolution of 1 byte or 256 grey values, since black and white cameras show a better contrast so that microstructural features can be distinguished more easily. After adjusting the sample position and brightness, consecutive images are taken every 2 mm in the x-direction, whereas the standard size chosen for a single image is 2.5 by 1.8 mm (KIPFSTUHL ET AL. 2006).

For the sample area described here, the scan took about an hour and acquired a series of about 386 images, which were later aligned using software developed by J. EICHLER (AWI) to get a full picture of the microstructure.

5.5 Raman spectroscopy

For this work, Raman spectroscopy was used to identify the material the black dots are made of since this method is non-destructive and requires minimal sample preparation. Raman spectroscopy belongs to the group of vibrational spectroscopies and utilizes the Raman effect which is defined as the inelastic scattering of light photons of molecules or molecular groups (e.g. SMITH & DENT 2005).

A molecule with no active Raman modes absorbs a photon and returns back to the same basis vibrational state as before the excitation, emitting a photon with the same frequency as the excitation source. This type of interaction is referred to as elastic or *Rayleigh scattering* (SMITH & DENT 2005). About 99.999 % of all incident photons undergo *Rayleigh scattering*, and thus are useless for molecular characterization, whereas one in every 10^8 photons produces a Raman signal (WEIKUSAT ET AL. 2012; SMITH & DENT 2005).

The laser beam induces an electric dipole moment to the sample which deforms molecules resulting in a vibration of the molecules with a characteristic frequency. If a molecule has vibrational Raman modes, its polarizability is changed by the induced vibration and a photon can transfer a part of its energy to the vibration so that the frequency of the scattered photon is shifted downwards. This is referred to as “*Stokes*” scattering. If a molecule is already in an

excited vibrational state, the excessive energy can be transferred to the photon, resulting in a higher frequency. This is called “*Anti-Stokes*” scattering (SMITH & DENT 2005).

The positions of the Raman bands directly give the energy of the detected vibrations, which can be influenced by environmental conditions, neighbouring atoms or the short-range order of the crystal structure (WEIKUSAT ET AL. 2012; SMITH & DENT 2005).

A Raman spectrum is unique for each chemical composition and can range from single bands to very complex multi-band spectra thus providing qualitative and quantitative information about the analyzed material. The spectrum is a plot of the intensity of the shifted light versus frequency and generally, the Raman spectra are plotted with respect to the laser frequency so that the Rayleigh band is set at 0 cm^{-1} . The Raman band positions give the energy levels of the different functional group vibrations (SMITH & DENT 2005).

The basic components of a Raman system (see fig. 16) include an excitation source (usually a laser), a sample illumination system, light collecting optics, a filter for rejecting the Rayleigh scattered light, a spectrometer and a detector (a photodiode array, CCD or PMT).

For this work the Raman measurements were performed on a WITec Alpha 300R microscopy system equipped with a frequency-doubled Nd:YAG laser ($\lambda=532\text{ nm}$), an UHTS300 Raman Spectrometer, with a Peltier-cooled DV401A-BV CCD detector and a 50x LWD objective, operated in a cold laboratory at $-15\text{ }^{\circ}\text{C}$ at the AWI (WEIKUSAT ET AL. 2015; HUEN ET AL. 2014). After the microstructure mapping the samples could directly be used for the Raman measurements. Some additional microtoming was performed in case the surface contamination challenged the identification of the grain boundaries. The black dots in the sample were located due to microstructure maps using the 10x LWD objective, then switched to the 50x LWD objective for further focusing and for obtaining the Raman spectrum. The challenge is then to remove background noise or fluorescence which is explained in chapter 5.7.2.



Fig. 16: The Raman microscope in the cold laboratory of the Alfred-Wegener-Institute

5.6 Correlations

To reveal possible links between the data obtained from the continuous flow analysis and the fabric analysis correlations were calculated, though it has to be noted that high correlation coefficients are not a sufficient condition for a causal relation between two components. If the correlation coefficient implies a correlation between component x and component y, it cannot be defined whether x influences y or vice versa, or whether they influence each other mutually. Furthermore, the correlation can occur randomly or even a third variable might interact with the two parameters, thus making it difficult to determine a certain relationship without further information (SCHÖNWIESE 2006). Nevertheless, correlation coefficients can be used as a tool to complement the results obtained from other methods.

For normally distributed data, *Pearson's Product-Moment correlation* can be calculated with the formula:

$$r = \frac{\sum_{i=1}^n (x_i - \bar{x})(y_i - \bar{y})}{\sqrt{\sum_{i=1}^n (x_i - \bar{x})^2} \sqrt{\sum_{i=1}^n (y_i - \bar{y})^2}}$$

with $\bar{x} = \frac{1}{n} \sum_{i=1}^n x_i$ and $\bar{y} = \frac{1}{n} \sum_{i=1}^n y_i$ being the arithmetic means of the data and n the population (BURT & BARBER 1996, p.386).

Since a linear correlation is assumed, the range of the correlation coefficient is between -1 and 1, whereas a correlation coefficient of 1 implies that the values of both variables increase or decrease synchronously. A negative value of -1 shows, that the values of one variable increase while the values of the other variable decrease. A correlation coefficient of 0 implies no correlations between the variables.

A calculated correlation requires a test for statistical significance where two hypothesis are proposed: the null hypothesis H_0 states, that the feature to be tested (the correlation between two parameters) occurred randomly, while with the alternative hypothesis H_1 the opposite case is assumed. For this work the alternative hypothesis states, that the parameters are correlated and thus the correlation coefficient is 1 (SCHÖNWIESE 2006). Furthermore, a confidence level has to be determined which shows the probability for the test decision for the related hypothesis (SCHÖNWIESE 2006). For this work a 95 % confidence interval was chosen.

With the formula

$$p = \frac{r\sqrt{n-2}}{\sqrt{1-r^2}}$$

the p-value can be calculated on the basis of the correlation coefficient r and the population n (BURT & BARBER 1996, p.391). The p value gives the strength for the evidence for the null hypothesis: a p-value >0.05 with a confidence level of 95 % leads to a rejection of the null hypothesis and thus it can be stated that the correlation is significant and does not occur randomly (SCHÖNWIESE 2006).

The *Shapiro-Wilk Test* shows (see appendix 10.2), that the data used for this thesis are not normally distributed, so that *Pearson's Product-Moment correlation* could not be applied and the correlation of *Spearman's Rho* was used instead. This correlation method can be used when the obtained data are not normally distributed or show ordinal scales (SCHÖNWIESE 2006). With difference to *Pearson's Product-Moment correlation* the values are ranked, which might result in a loss of information.

Spearman's Rho is calculated as

$$r_s = 1 - \frac{6 \sum_{i=1}^n D_i^2}{n(n^2 - 1)}$$

where n is the population and D the differences of the ranks (BURT & BARBER 1996, p.395).

The p-value is calculated as

$$p = r_s \sqrt{n-1}$$

where n is the population and r_s the correlation coefficient (BURT & BARBER 1996, p.396). With this formula the p-value can only be calculated asymptotically since bindings can occur due to the ranking of the values. Bindings are referred to as same values in the correlated data sets so that they cannot be assigned an explicit rank. Thus, the arithmetic mean of the differences of the ranks are used to calculate the p-value, although less than 25 % should show bindings otherwise an extended formula has to be applied (BURT & BARBER 1996). For this work, the given formula could be used.

Since there is no significant correlation between NEEM CFA data and fabric data in many cases a cross correlation was calculated in addition to *Spearman's Rho*. The data can be regarded as time series, because snow accumulates in layers on the surface of the ice sheet so that the depth can be related to time. When calculation a cross correlation, the data sets (or time series) are shifted against each other in steps of one data point (one value) in order to determine whether stronger correlations occur with a postponement.

The cross correlation is calculated with the formula

$$r_c = \frac{\sum_{i=1}^{n-\tau} a_i b_i + \tau}{\sqrt{\sum_{i=1+\tau}^n b_i^2 \sum_{i=1}^{n-\tau} a_i^2}}$$

where n is the population, a_i and b_i the correlated variables and t the shift in time (postponement) (SCHÖNWIESE 2006, p.231).

The correlation plots were generated using the free software R. It was not possible to calculate a cross correlation with *Spearman's Rho* so that *Pearson's Product-Moment correlation* was used, which is of course not correct but might still give an impression on how a shift in time influence the correlation coefficient. The x-axis shows the shift in time while the correlation coefficient is shown on the y-axis. The blue dashed line marks the 95 % confidence level.

5.7 Data processing

5.7.1 CAxes and RunningMean-Programme

To determine c-axes orientations and perform statistical analyses on the data obtained by the Fabric Analyzer, two programmes are applied: with the cAxes programme a segmentation of the grains can be achieved, which makes it possible to calculate grain statistics for each thin section. Using the data from the Fabric Analyzer, the azimuth and colatitude are transformed into Cartesian coordinates and with some additional adjustments of the parameters, a vector image can be generated from the coordinates for x,y and z (EICHLER 2013).

The data output from the cAxes programme is then used as an input to the RunningMean programme (written by J. EICHLER 2013 using C++). This programme aims to improve the grain statistics in terms of crystal orientations and resolution of the grain sizes using a running mean. For this work, all six thin sections from one bag, related to numbers from 101 to 601 were aligned (TAMMEN 2012). In the following some parameters have to be defined, like (if

desired) the removal of the edges of the sample given in pixels. Additionally, the area to be averaged (frame height) should be determined, as well as the step width. The smaller the step width, and frame height, the higher will be the resolution of the outcoming data. According to the CFA data, which theoretically have a depth resolution of 1mm, the frame height was chosen 500 pixel ($\cong 1$ cm) and the step width 50 pixel ($\cong 1$ mm). The edges were not removed. After starting the programme, the data are saved in a “runningmean.txt” file from which the data for the mean grain size and eigenvalue 3 are taken to generate the plots for each bag.

5.7.2 Raman software

After the Raman spectra were obtained, it was necessary to extract the band parameters from the spectrum in order to allow a more reliable identification of the material. Therefore, the WITec software also used to operate the Raman microscope was applied. As a first step, the 0-peaks of the spectra were mathematically fitted to a Gauss-Lorentz function in order to maintain the correct positions of the peaks since the instrument is not calibrated prior to each measuring session. Furthermore, a background correction was performed to improve the quality of the spectra and the ice spectrum, which always occurs in combination with the spectra of the extrinsic material, had to be subtracted.

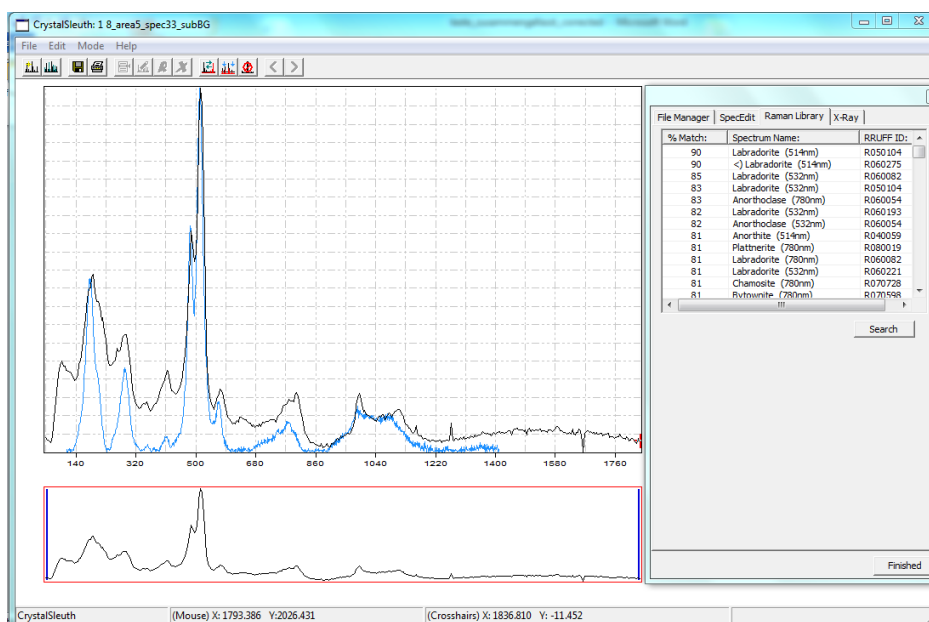


Fig. 17: Example of an identification of a Raman spectrum using the CrystalSleuth software

The identification of the spectra is based on the data obtained from the RRUFF database for Raman spectra, x-ray diffraction and chemical data for minerals (<http://rruff.info/>) and the related software CrystalSleuth. The software reads the spectra and after some additional background correction, the minerals and mineral compositions matching the given spectrum are suggested (see fig. 17). Although not completely reliable, the software can be used to identify the major Raman bands of a spectrum.

5.7.3 Structure of the plots

For the following analysis, the open source software and programming language “R” is used. To generate graphics with R both datasets have to contain the same amount of data. In the data obtained from the RunningMean analysis 10 values were missing, which might be due to the cutoff occurring when the core is separated into six sections. The cutoff is compensated by including NaN’s (not a number) into the file with an even distribution at the positions where the transition from one thin section to the next one is expected (the cutoff is not documented during sample preparation). After that, both datasets could be plotted and summarized into one graphic.

The information of the bag number and the depth are included in every plot, whereas the depth can be calculated from the bag number with the formula:

$$(B_n - 1) * 0,55 = x_1$$

$$(y - 1) * \frac{0,55}{6} = x_2$$

$$x_1 + x_2 = D$$

, whereas B_n is the bag number, y is the piece number which is related to the data from the thin section for the RunningMean programme (101-601) and D the calculated depth.

The structure for the plots described in the following is equal for each bag (see appendix 10.3): the lower x-axis shows the absolute depth (m), whereas the upper x-axis gives the relative position in the 55 cm long bag. The y-axes on both sides of the plot are adapted to the values of the data for the ions, the mean grain size and the eigenvalue 3, respectively. In order to compare the data and estimate their statistical relevance it is necessary to give the mean

grain size in mm^2 and thus recalculate it from the value given in pixels from the RunningMean programme. For every value in the frame the mean grain size in pixels has to be multiplied with 0,0004 to obtain the value in mm^2 . The upper graphs show the plotted values for ammonium (NH_4^+) with a light green colour with the axis on the left side and nitrate (NO_3^-) on the right axis in black. Beneath, the electric conductivity is plotted in dark green. In the middle, the turquoise line shows the content of calcium (Ca^{2+}) with the corresponding axis on the left side and the content of sodium (Na^+) with a purple line. The eigenvalue 3 is plotted underneath with a single curve in orange. Finally, the dust content (number of particles/ml; blue line) is plotted together with the mean grain size in mm^2 (red line). For every plot the trend images obtained from the Fabric Analyzer are aligned for one bag (\cong 6 thin sections/images) and included in the graphics. The linescan images are not available for all samples.

6. Results

6.1 Preliminary results:

Bag number: Bag 1346 , depth top: 739.75m , depth bottom: 740.3m

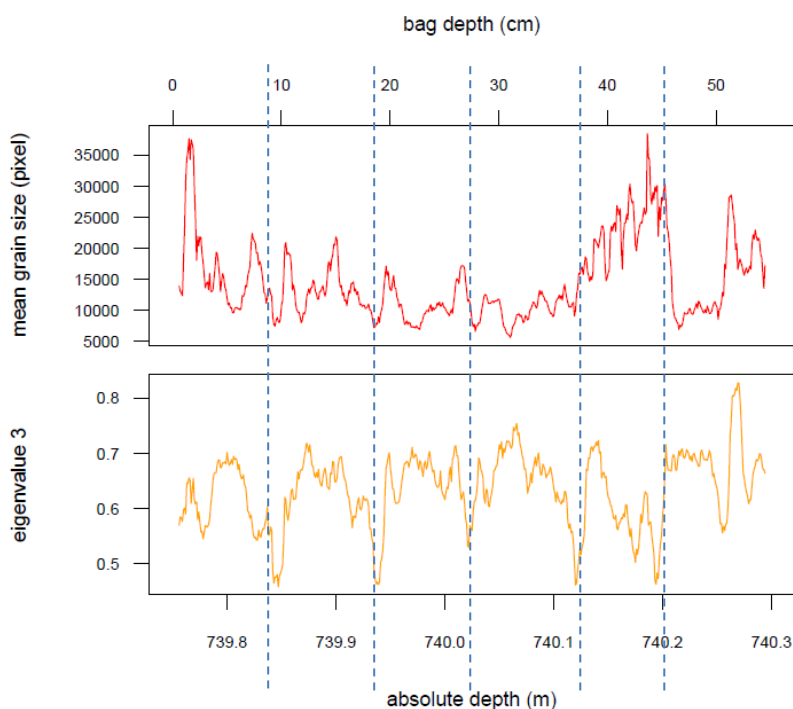


Fig. 18: The preliminary result for bag 1346 with dashed blue lines marking the edges of the thin sections

After initially plotting the data, several negative peaks of the mean grain size and the eigenvalue 3 were identified that appear with a distance of 9 cm at the same positions in every plot. These peaks are considered to be artefacts originating from the grains forming from the water which was used to fix the thin section on the glass plate. Fig. 18 shows the mean grain size and the eigenvalue 3 plotted for bag 1346 as an example (the red arrows mark the artefacts). The negative peaks had to be eliminated manually in order to prevent major mistakes in the correlation statistics, as they could not be removed automatically despite some adjustments of the cAxes programme. To visualize the artefacts (or spikes) a plot of the total area was generated: For each frame of the RunningMean data, the mean grain size was multiplied with the number of grains (per frame) which should result in the analyzed overall frame size in pixel. With the total area it can be rated whether the xAxes programme is able to identify all grains to fill the frame. In case the difference between the area of the frame and the area of the grains is too big, the results of the running mean should be rejected since the software did not identify all grains.

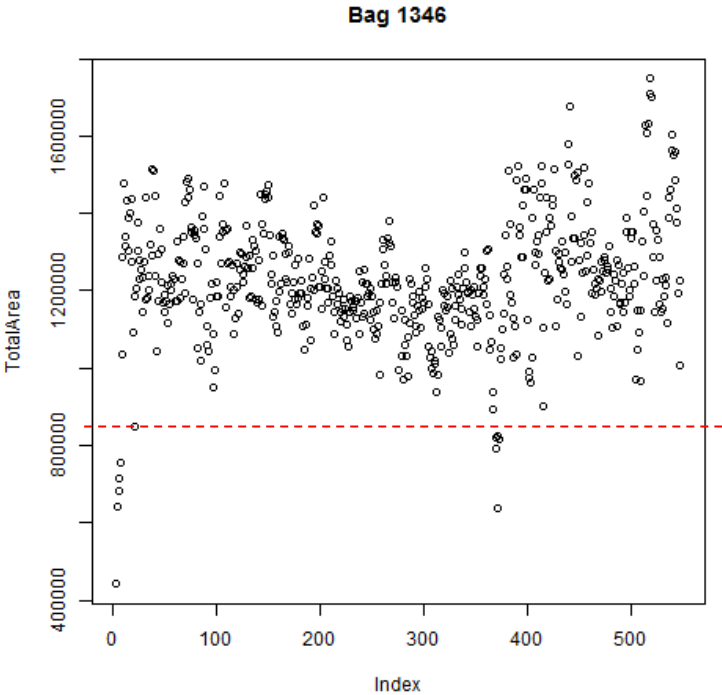


Fig. 19: Plot of the total area (mean grain size (pixel)*number of grains) for bag 1346

Fig. (19) shows the plot of the total area exemplary for bag 1346. The total area plot was generated for the data of the mean grain size and eigenvalue 3 for every bag so that a limit for the grains to be reliably identified could be determined. Below that limit, the spikes were

removed manually and substituted by NaN's. The limit was chosen independently for the mean grain size and for the eigenvalue for every bag according to the range of the values and the results from the trend images. In the following the amount of the data that could be used for further analysis is given in percent for every bag.

The plots described here and the tables with the correlation coefficients (cc), are to be found in the appendix (see appendix 10.3), except for bag 1346 which was chosen for a case study and is therefore included in this chapter (see chapter 6.2) Very high or strongly increasing values for the CFA parameters occurring at the edges of the bag or at breaks are not included in the interpretation as they might be due to contamination during the measuring process. Gaps in the data can be related to the previously described removed spikes, to breaks in the core or even air bubbles that got accidentally into the CFA system. In the following, the main results for every bag are described, whereas for the significant correlation coefficients (obtained by *Spearman's Rho*) rounded values are given.

6.2 Results of all 12 bag plots (see appendix 10.3 and 10.4)

Bag 1346

For bag 1346 (739,75 m to 740,3 m depth) 94,81 % of the data for the mean grain size and 92,58 % of the data for the eigenvalue 3 could be used. This bag is broken in the middle so that no linescan image and no CFA data could be obtained (see fig. 20). The thin section 1346_201 and 1346_501 were chosen for a case study since they show important features to be interesting for further examination with Raman spectroscopy: one criterion was the high ammonium peak of 27,20 ng/g at 739,85 m. Since ammonium is considered to be one of the compounds that might be incorporated into the ice crystal lattice, it would be of great interest if it is found as one of the black dots. Furthermore, the chosen section show high dust peaks that can be related to the maxima of sodium and calcium at 739,91 m and 740,17 m, respectively. The first two dust peaks in section 201 in the range from 739,89 m to 739,94 m go together with rather small grain sizes, whereas the peak from approximately 740,15 m to 740,20 m seems to correlate with larger grains. In the case study (see chapter 6.3 and 6.4) the aim is to find possible differences in the composition of the black dots by using Raman spectroscopy. The c-axes do not show a preferred orientation.

The mean grain size shows some weak correlations with several compounds (see tab. 2): a significant positive correlation with dust (cc=0,13), with conductivity (cc=0,10) and with nitrate (cc=0,11) as well as a weak negative correlation with ammonium (cc=-0,10).

The eigenvalue 3 correlates negatively with sodium (-0,19), with calcium (-0,18) and with ammonium (-0,19) (see appendix 10.4).

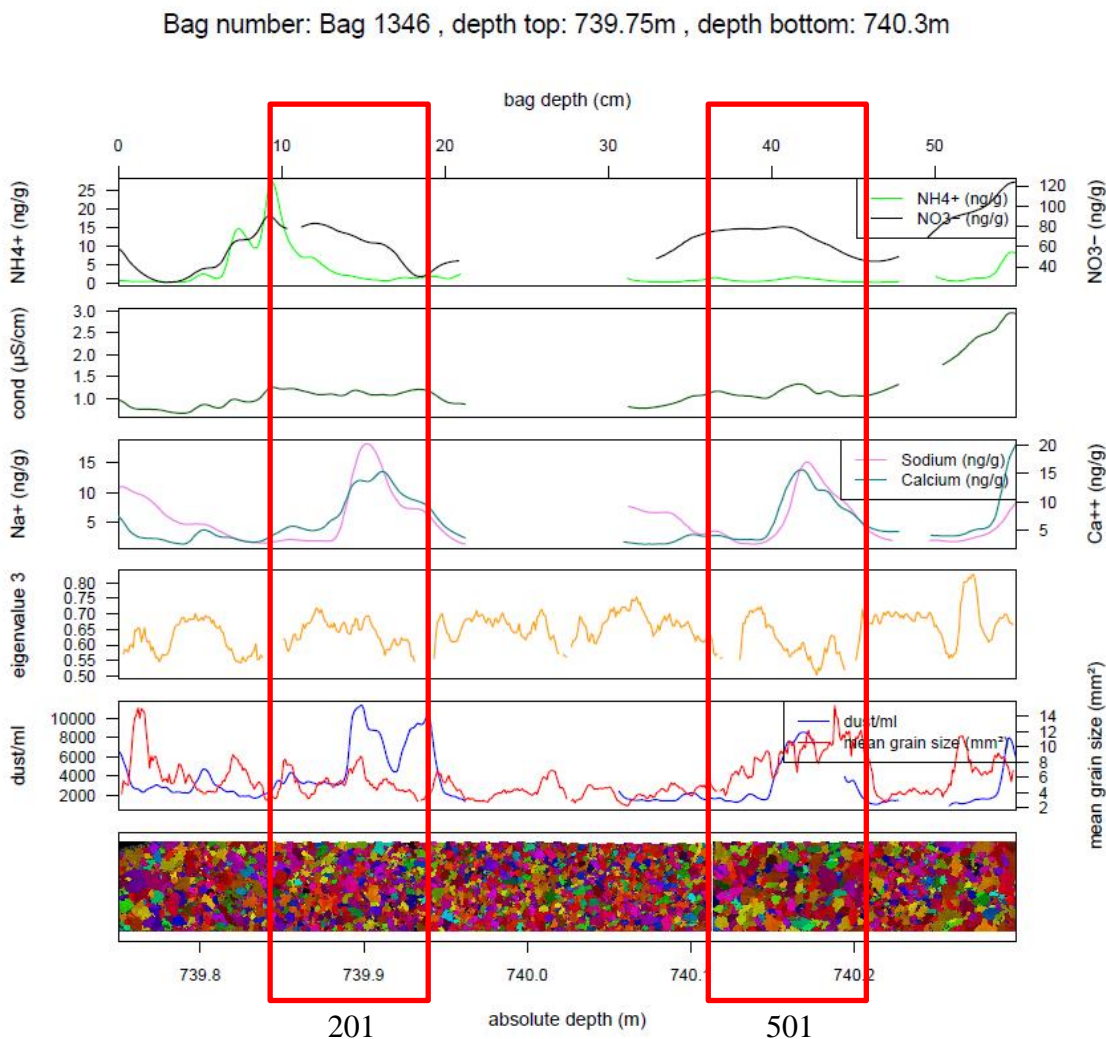


Fig. 20: Bag plot of bag 1346. The red rectangles mark section 201 and 501.

Generally, almost no correlations can be found between dust and the mean grain size. Due to some fractures in the cores, the interpretation of the ion record is difficult since information is missing to complete the picture. Still it can be stated, that the nitrate signal often goes together with the sodium record while the calcium signal is mostly related to dust. The calculated correlations do neither constantly show a relation between specific compounds nor can be related to certain peaks in the data for the compounds. They rather occur randomly throughout the bags which might be due to some difficulties with the depth scale (see chapter 7.6).

6.3 Case study bag 1346_201

Bag plot

The section 201 (see fig. 20) from bag 1346 originates from a depth between 739,84 m to 739,96 m. The most characteristic features of this section are the ammonium peak of 27,18 ng/g at 739,84 m and the high peak of dust (11292 particles/ml) at 739,90 m. Calcium shows a maximum of 15,34 ng/g at 739,91 m accompanied by a maximum peak in the sodium ion concentration of 18,18 ng/g at 739,90 m. The conductivity remains rather stable at around 1.1 $\mu\text{S}/\text{cm}$. The mean grain size varies between 2,89 mm^2 and 8,74 mm^2 . The eigenvalue 3 fluctuates between 0,54 and 0,72 showing that the distribution of c-axis orientations in depth is not completely random.

Correlations

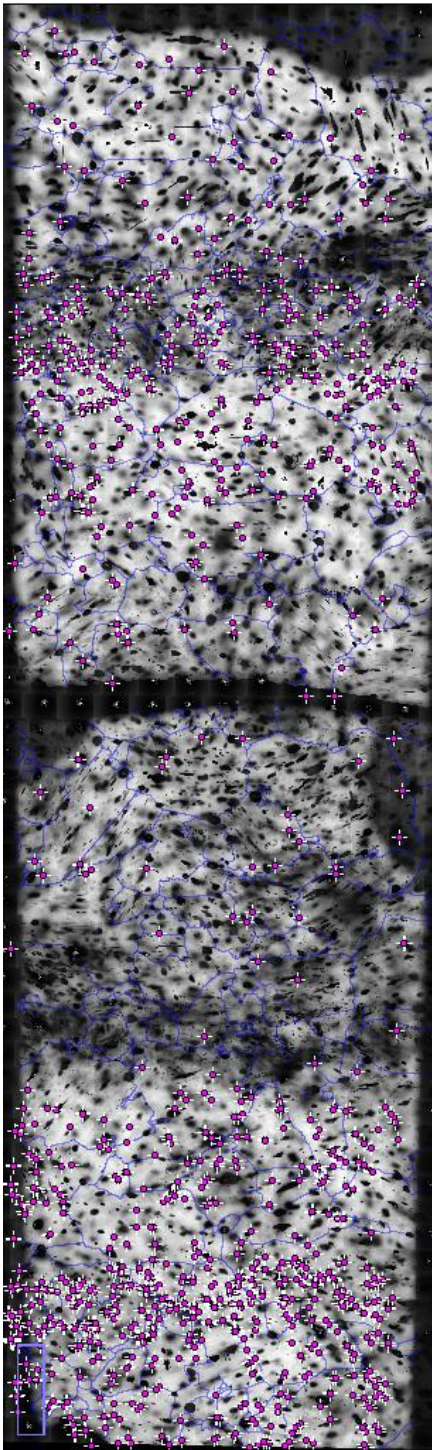
Weak positive correlations could be found between the mean grain size and sodium ($cc=0,29$) as well as between the mean grain size and calcium ($cc=0,26$). The eigenvalue 3 negatively correlates with sodium ($cc= -0,21$) and calcium ($cc=-0,23$) and positively correlates with ammonium ($cc=0,24$) (see tab. 2).

Tab. 2: The correlation coefficients for bag 1346_201. The blue colour marks the significant correlations (significance level 95%)

	dust	conductivity	sodium	calcium	ammonium	nitrate
mean grain size	0,092	-0,097	0,286	0,261	-0,079	0,115
eigenvalue 3	-0,188	-0,148	-0,206	-0,228	0,237	0,577

The cross correlations show that with a lag of 17 mm the correlation between the eigenvalue 3 and sodium gets stronger, showing a correlation coefficient of approximately -0.70. The coefficient for the eigenvalue 3 and calcium as well as dust rises up to -0,60 with the same lag. With small lags of 6 to 7mm weaker positive correlations between the mean grain size and ammonium ($cc=0,4$) and between the mean grain size and nitrate ($cc=0,45$) can be found. These results imply slight irregularities in the depth scale, which need further investigation addressed later in the discussion section (see appendix 10.5).

top



bottom

1 cm

Microstructure mapping

Three microstructure maps were prepared for both sections from the bag: one obtained from the surface in order to get a complete picture of the grain and subgrain boundaries and two with a focal depth of about 500 to 1000 μm below the surface to exclude impurities that might be related to surface contamination (see appendix 10.7). The black dots were marked with tools from the ImageJ software. Fig. (21) shows the microstructure map of the surface of section 201, where the grain boundaries are marked with blue lines, and the black dots counted from an inner layer with a focal depth of about 500 μm below the sample surface are highlighted in magenta. The surface picture was included in order to get a better overview of the distribution of the black dots in relation to the grain boundaries, thus revealing visible connections to the microstructure. Fig (22) shows examples of the appearance of the black dots counted here (marked with red circles).

Generally, the microstructure mapping revealed that bag 1346 contains bubble-rich ice where bubbles are elongated parallel to the basal planes. Just as the microbubbles, this might be a relaxation effect, since the core was drilled already between 2007 and 2011. Two dark bands of high bubble concentration can be seen in the picture, one on each side of the break.

Fig. 21: Microstructure map of section 201 with marked grain boundaries (blues) and labelled black dots (magenta)

After labelling the black dots, a total number of about 1500 could be found in one focal plane.

This is an approximated number, since some particles were conglomerated, making it difficult to distinguish between single black dots. Furthermore, some features could not be explicitly identified as black dots just by visible inspection, and could have also been microbubbles or other artefacts. Those features were still included in the labelling in order to characterize them in more detail using Raman spectroscopy. The distribution of the labelled particles shows two bands of high impurity concentration, which do not match with the dark bands of the bubbles. The peaks correspond to the double peak in dust concentration that can be seen in the CFA-data, indicating that for this section there is a large shift of almost 2 cm in the depth scale between CFA and fabric measurements. The distance of the bands in the microstructure mapping image matches the distance of the peaks in the plot. Furthermore, the ammonium peak might not necessarily be located in the chosen area but could also be shifted and thus included in section 101. The shift in depth scale is in agreement with the results from the cross correlations, since three out of four coefficients got stronger with a certain lag in the same direction. Outside of the bands (especially in the middle and in the area of the upper bubble layer) the concentration of black dots is far lower. No relation between the position of the particles and the grain boundaries could be found, but the upper dust peak (or band of black dots) coincides with small grain sizes (see fig. 20).

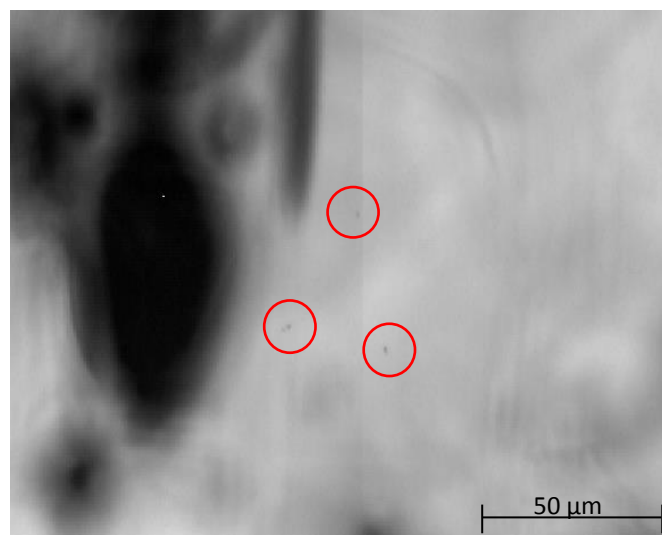


Fig. 22: Examples of black dots as they were labelled in the microstructure map

Raman spectroscopy

For section 201, 151 particles were measured with Raman spectroscopy, but only for 64 particles a spectrum could be obtained. The areas to be investigated with the Raman were chosen on the basis of the microstructure mapping image with the labelled dots. At first, areas with high concentrations were chosen, followed by areas with a lower concentration. Fig (26) shows the microstructure mapping image with the measured areas being marked with a red rectangle and a number according to their order. The rectangles are larger than the area that was actually measured for better visibility in the figure. Generally, more particles than labelled were measured due to the fact that changing the focus of the Raman microscope revealed some more black dots in the vertical dimension, which were then included in the measurements.

In this section a lot of particles were conglomerated (fig. 23 left) or even appeared to form chains (fig. 23 right), whereas not every particle belonging to such a conglomeration necessarily showed the same spectrum. Some conglomerations separated after being hit by the laser, which then allowed a measurement of the single compounds, others did not.

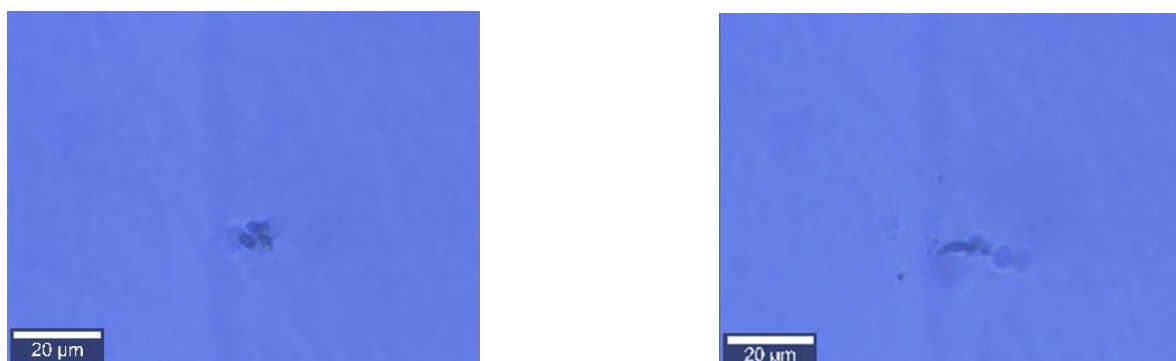


Fig. 23: Examples of black dots forming conglomerates (left) or chains (right) (observed with the Raman microscope)

The results are summarized in a pie chart for each area, which shows the amount and compositions of chemical species that could be identified with the RRuFF database. The numbers above and below each pie chart (x/y) show the total amount of particles measured (x) and the amount spectra that could be obtained, respectively (y). Four versions of the pie charts were generated in order to get a better understanding of the distribution of the chemical species. Due to the uneven distribution of the black dots, a different amount of particles was measured for each area, which complicated the statistical comparison. As some particles were conglomerated, their Raman spectrum was often analysed as a mixed signal, which was at

first still considered as one particle. As a second step the signals were counted as originating from two different particles (more could not be distinguished in the Raman spectrum) (see fig. 24), which also changes the total amount of particles showing a spectrum. For the plots with the separated signal a slightly different legend had to be employed (see fig. 25). Furthermore, it was distinguished between pie charts including only the particles that actually showed a spectrum and all measured particles (see tab. 3).

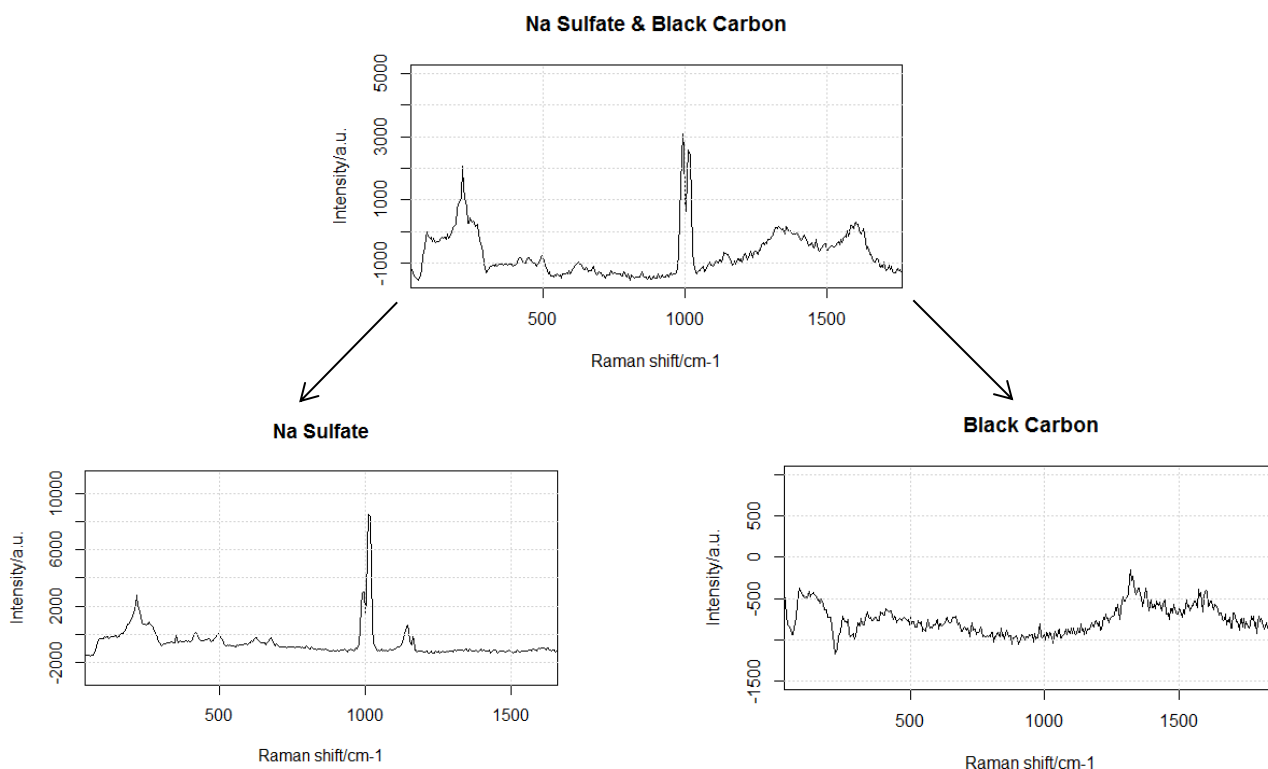
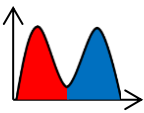
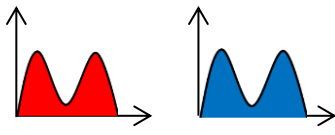


Fig. 24: Schematic drawing showing how mixed and separated signal were generated

Tab. 3: Assigning the Raman spectra into four groups

Mixed signal (see fig. 25 and appendix 10.8) 		Separated signal (see fig. 25 and appendix 10.8) 	
Including all measured particles showing a spectrum Fig(a)	Including all measured particles Fig(b)	Including all measured particles showing a spectrum Fig(c)	Including all measured particles Fig(d)

Since black carbon is always one compound of the mixed signals, the colour codes emphasize that by giving all black carbon related compositions a blue colour with varying brightness. Pure sulfate compounds are coloured in different shades of red and silica particles in green colours. The trace compounds like titan oxides are coloured purple and metal hydroxides brownish. The light grey colour was chosen for the particles that did not show a spectrum, the dark grey colour belongs to the particles whose spectra could not be identified without doubt. Since in small pie charts the colours might be difficult to distinguish the colour code is complemented by a combination of letters and numbers to guarantee a clear identification.

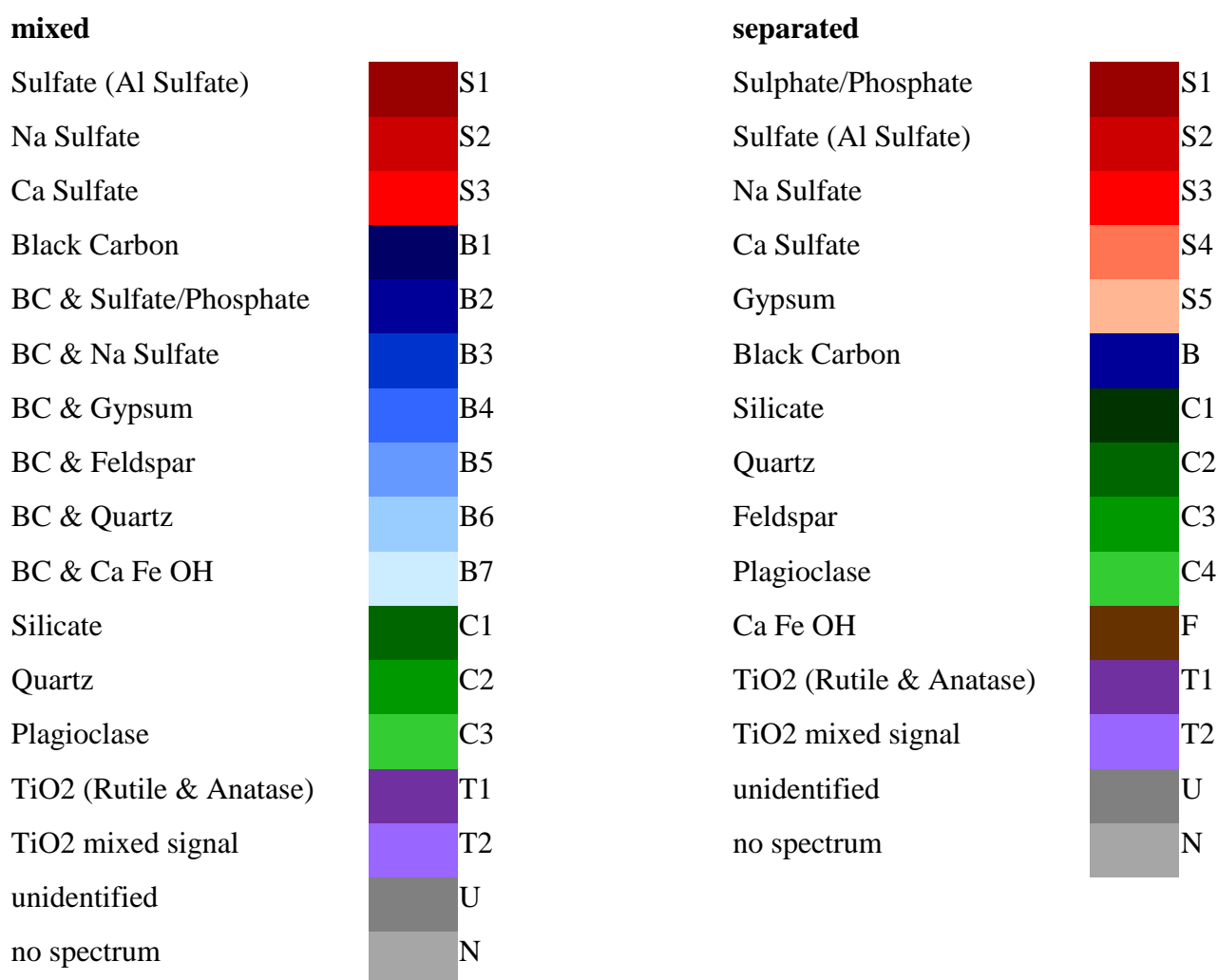


Fig. 25: Colour code for mixed and separated signals

Still, the main colours are regarded to be an appropriate method to give an overview of the composition and distribution of the chemical species for the entire section. This code was generated due to the intensity of the Raman spectrum: if the signal is weak (showing only one or two characteristic peaks) a distinction between sulphate and silica particles will still be possible whereas with a stronger signal (showing more than two peaks) different kinds of sulphates can be identified. The number of particles measured in one area varies between 4 particles in area 10 and 11 and 41 in area 2. Examples of the Raman spectra together with the reference can be found in the appendix (see appendix 10.6)

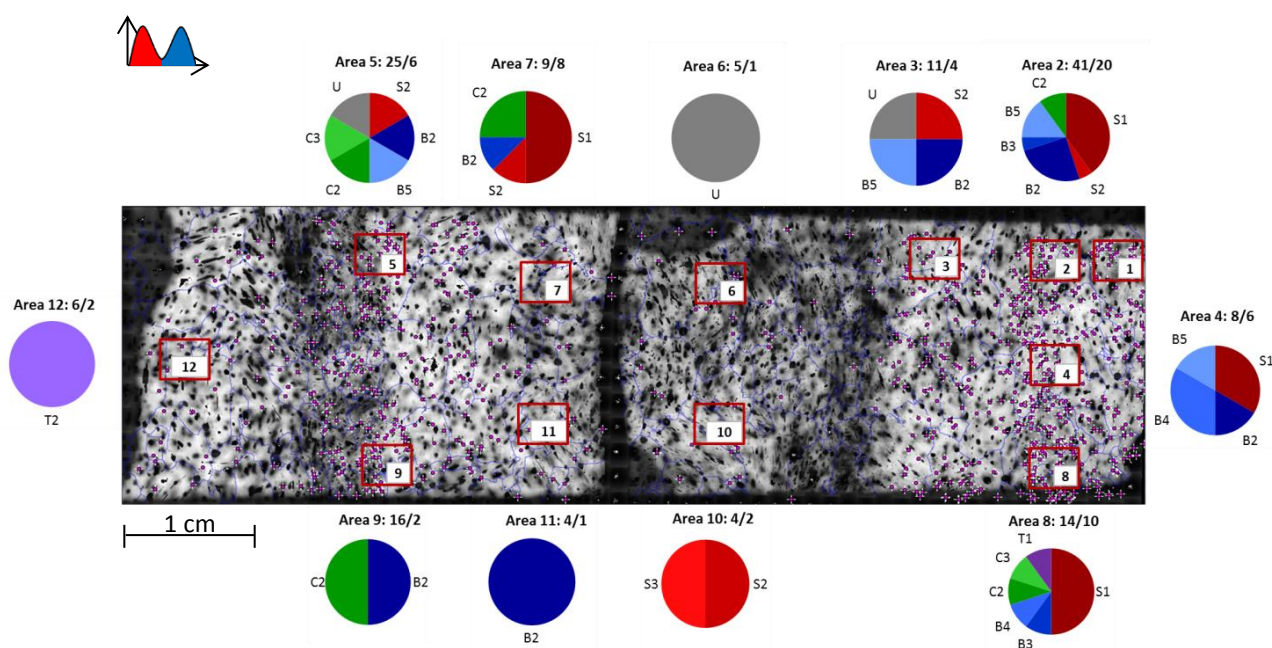


Fig. 26: Bag 1346_201: microstructure map with the pie charts including the particles with a Raman spectrum as a mixed signal

Concentrating on fig. 26 (fig. a), the major compounds measured are sulfates, black carbon (with the characteristic peaks at around 1350 and 1610 $\text{rel}^{-1}/\text{cm}$ (e.g. BEYSSAC ET AL. 2002)) and to some extent silica particles (e.g. quartz and feldspar) as well as titan oxide as a trace species. In the band related to the deeper dust peak (around 739,94 m) significantly more sulfate (possibly aluminum sulfate) occurs (e.g. area 2,7 and 8), whereas in the upper band more silica particles can be identified (e.g. area 5, 9 and 12). Quartz is the main species from the group of silica particles (e.g. area 5 and 7). The sulfates are mainly represented by sodium sulfate (e.g. area 3) and in some parts calcium sulfate (area 10). Black carbon related compounds are almost equally distributed over the entire sample. In area 5 and 6 some

particles could not be identified. The spectrum is highly complex, with Raman bands up to 2900 cm^{-1} . The particles could be identified as organic compounds, although a closer identification could not be achieved. The comparison to spectra obtained from pollen does not show any matching peaks. Area 3 shows another unidentified spectrum which is considered to be an anorganic compounds (see appendix. 10.6) In area 8 rutile as a titan oxide could be found, which can accompany sulfate in layers of volcanic ash (ABBOTT & DAVIES 2012).

Figure b (see appendix 10.8) implies that a spectrum could be obtained for approximately one third of the measured particles, which might be due to the fact that some compounds such as sea salt cannot be detected with Raman spectroscopy. Additionally, some particles tend to move away from the laser due to local heating and thus melting on the microscale. These particles cannot be measured even after several corrections of the sample position. Furthermore, regarding the amount of measured particles, a higher percentage of particles located in areas with low concentrations showed a spectrum (e.g. area 7, 10, 12). In area 1 no spectrum could be obtained which first was attributed to lack of experience with this method since it was the first area to be measured. However, an additional checking after all other spectra were measured still did not lead to successful results.

Separating the mixed signals as done for fig c and d (see appendix 10.8) leads to different percentages in the composition of the species: whereas in fig a and b sulfate and black carbon where the major components showing almost equal amounts, it can be seen in fig c and d that sulfate is the major component and black carbon just shows half of the amount of sulfate. Every pie chart includes between one and two thirds of sulfate. The figures also show that sodium aluminum sulfate and gypsum were only recorded as a mixed signal (e.g. area 7 and area 4). The upper dust peak still shows more silica particles compared to the deeper part of the sample. The amount of black carbon is approximately the same as the amount of silica particles. Except for area 10 and 12, which generally show a lower impurity concentration black carbon can be found in every measured area.

6.4 Case study bag 1346_501

Bag plot

The section 501 from bag 1346 originates from a depth between 740,12 m to 740,21 m (see fig. 20). The main features are a peak in the sodium ion concentration of 15,12 ng/g at 740,17 m and a peak in calcium of 15,64 ng/g at 740,17 m. The conductivity remains on a level of approximately $1,1 \mu\text{S/cm}$. The dust record shows a gap but is still included for the

interpretation. The dust values show a maximum peak of 8526,6 particles/ml at 740,17 m. Due to the gap it is difficult to assess the overall dust content but it seems to be lower than in section 201. The mean grain size varies between 3,65 mm² and 15,39 mm² and the eigenvalue 3 shows fluctuations between 0,50 and 0,72.

Correlations

A strong positive correlation could be found between the mean grain size and sodium with a correlation coefficient of 0,62. The eigenvalue 3 negatively correlates with sodium (cc=-0,75) (see tab. 4). When calculating the cross correlations only a small lag is sufficient to result in a stronger correlation coefficient. With a lag of 2 mm the eigenvalue 3 negatively correlates with calcium and dust both with a correlation coefficient of -0,78. Furthermore, stronger correlation with sodium (cc=-0,79) at a lag of 2 mm and with ammonium (cc=-0,63) at a lag of 6 mm is calculated. With a lag of 3 mm the mean grain size correlates with calcium (cc=0,52) and with dust at a lag of 3 mm (cc=0,48) (see appendix 10.5).

Tab. 4: The correlation coefficients for bag 1346_501. The blue colour marks the significant correlations (significance level 95%)

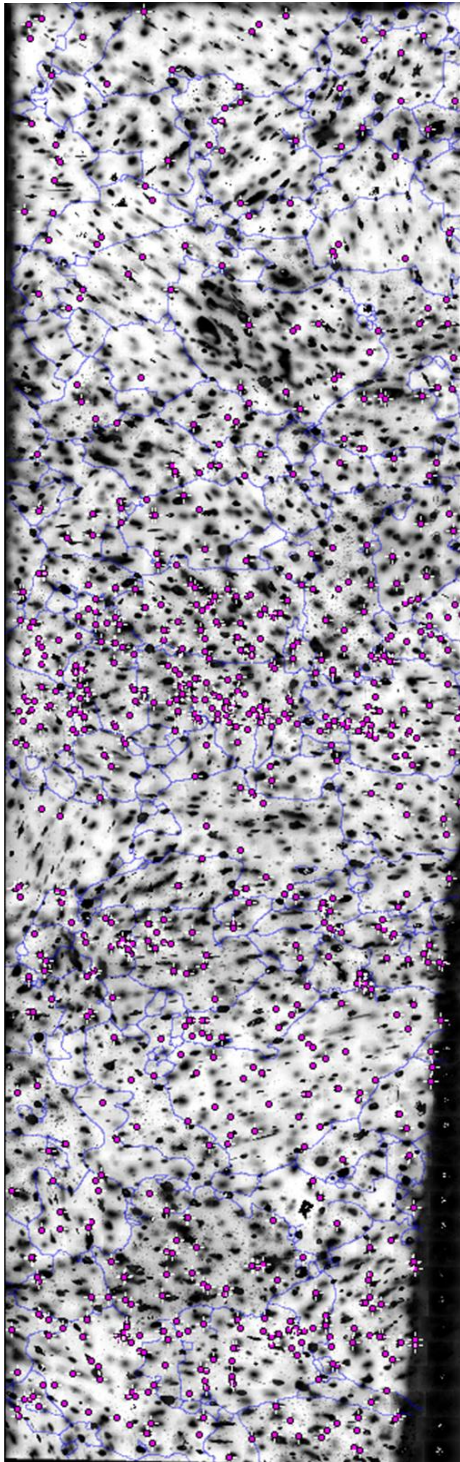
	dust	conductivity	sodium	calcium	ammonium	nitrate
mean grain size	0,558	0,102	0,620	0,562	-0,162	-0,535
eigenvalue 3	-0,570	0,608	-0,725	-0,680	-0,538	0,193

Microstructure mapping

Fig. (27) shows the microstructure map of section 501 including marked grain boundaries in blue and the labelled black dots. Basically, this section shows the same relaxation features as section 201, although the bubbles seem to be a little less elongated. The bubbles are equally distributed showing only some slightly darker areas but no bands of high concentration. The impurity concentration is lower compared to section 201; only about 1000 black dots were labelled here (focus depth: approximately 500 µm). They are clustered in distinct bands but show higher concentrations in the middle of the sample as well as in the lower parts. The areas with a higher concentration of black dots coincide with areas of higher bubble density. The grain sizes show strong variations with several large grains especially in the deeper part

of the section. Still, no connection between the black dots and the microstructure is apparent. Furthermore, small bubbles developed on the surface of some grains which might be a result of a dewing process due to irregularities in the air condition in the ice laboratory.

top



bottom

1 cm

Raman Spectroscopy

In section 501 155 particles were measured with Raman spectroscopy, of which 96 spectra were obtained (see fig. 28). Generally, a large amount of particles were too small to target precisely with the laser and thus could not be measured. Particles in this sample also showed fewer conglomerations and did not appear in chains. Fig a shows the microstructure map with the pie charts for the mixed Raman spectra for only the particles that actually showed spectra. Black carbon and sulfate are still the major components and show an equal distribution over the entire sample. In area 3 and 4 two particles were found where black carbon could be measured as a single signal. Especially towards the deeper end of the section sodium sulfate and calcium sulfate could be identified (e.g. area 4 and area 9). Compared to section 201 this sample contains less silica particles showing a single signal, which are mostly plagioclase and to some extent quartz (e.g. area 7 and area 10). In area 3, 8 and 10 quartz was also found in combination with black carbon. In area 1 anatase, another modification of TiO_2 could be found (BERGER ET AL. 1993). In area 9, a titan oxide as a mixed signal was found, but could not be identified in detail.

Fig. 27: Microstructure map of section 501 with marked grain boundaries (blues) and labelled black dots (magenta)

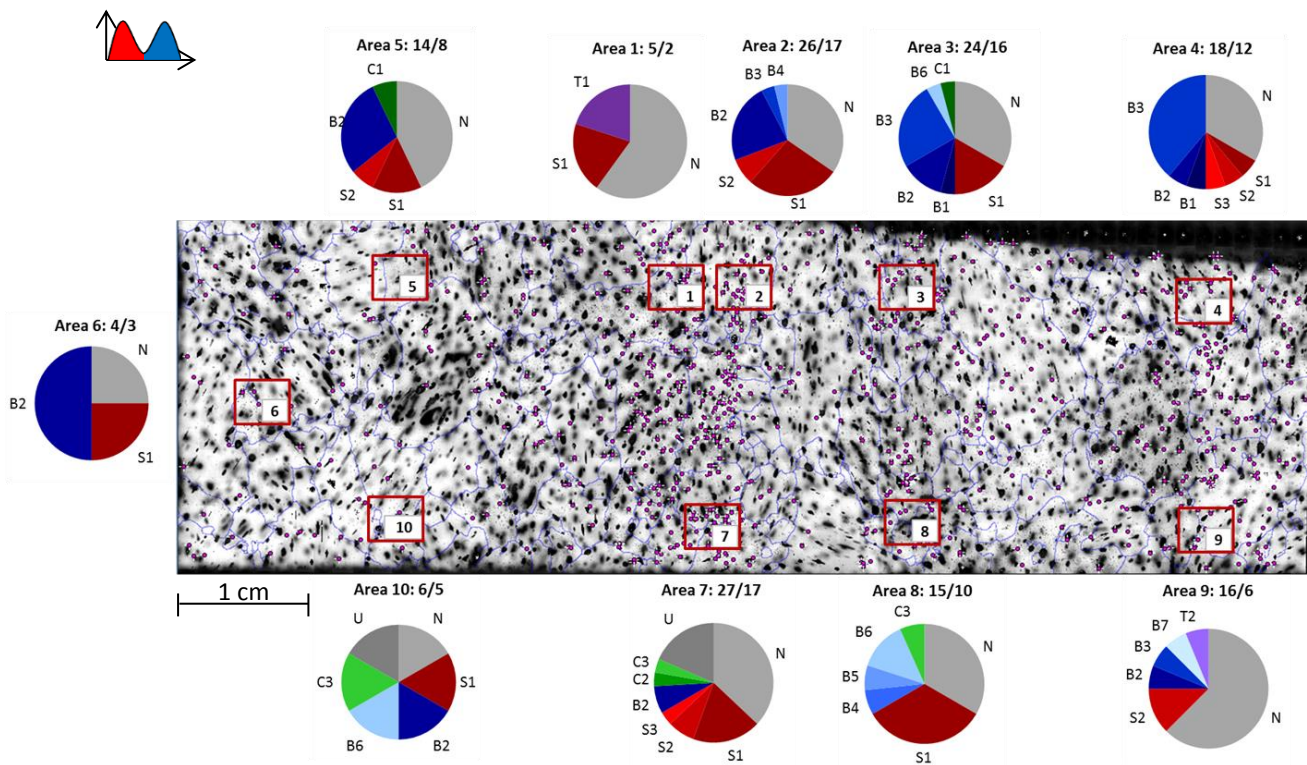


Fig. 28: Bag 1346_501: microstructure map with the pie charts including the particles with a Raman spectrum as a mixed signal

Fig. (29) shows Raman microscope images of particles that are located on a subgrain boundary or crack. These particles all showed a unique spectrum that could not be unambiguously identified, but is very likely organic material (see fig. 30). The spectrum of *Azospirillum brasilense* (see appendix 10.6) can be suggested as a possible match. All particles showing this spectrum could be related to subgrain boundaries

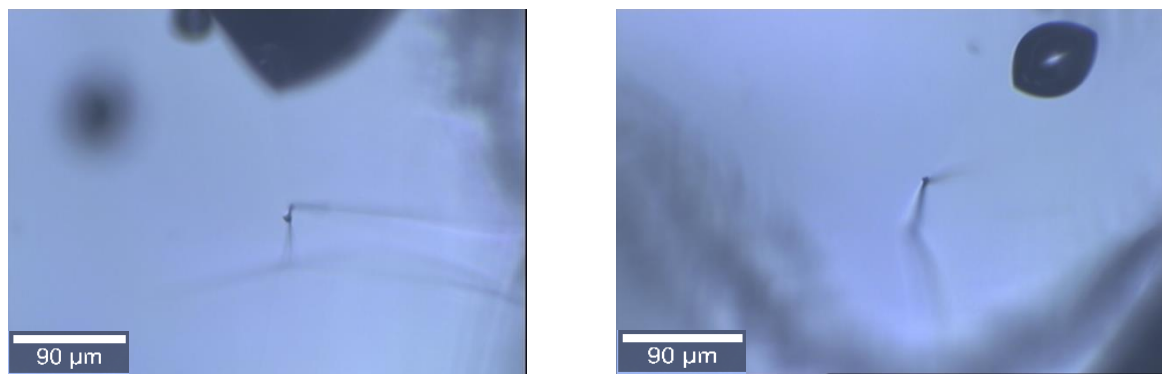


Fig. 29: Examples of black dots being located on a subgrain boundary/crack (observed with the Raman microscope)

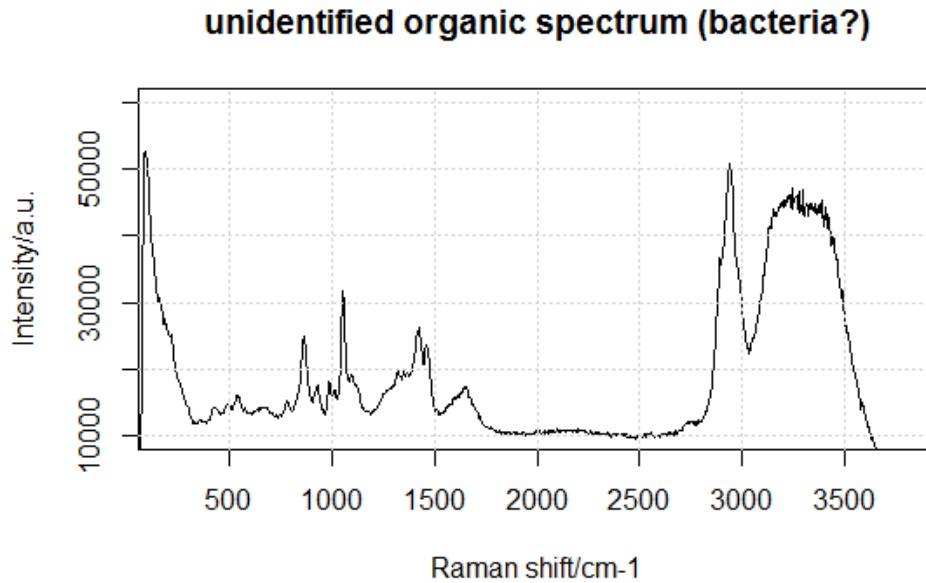


Fig. 30: Raman spectrum obtained from the organic compounds being located on a subgrain boundary/crack

Another special feature of the spectrum is the ice peak at a Raman shift between 3000 and 3600: according to DURICKOVIC ET AL. (2010) the rounded shape of the peak indicates that it is not ice but water, so that the bacteria would be inhabiting a liquid vein.

Fig b reveals that for almost two thirds of the measured particles a spectrum could be obtained which is significantly more that for the other section. This might be due to the fact that particles showed fewer conglomerations and also due to more experiences with this method after measuring high numbers of particles. Fig c and d show the pie charts with the separated signals. As in section 201 sulfate and black carbon are the major components and are equally distributed over the entire section.

6.5 Comparison of section 201 and 501

Comparing the plots and the correlation coefficients of both sections it can be determined that the depth scale is not reliable since a large shift of approximately 2 cm occurred in section 201 and the correlations (*Spearman's Rho*) remained weak. The cross correlations revealed this shift although it does not occur as a constant offset over the entire bag. Generally, more and stronger correlations could be found between the chemical parameters and the eigenvalue 3 and less correlations with the mean grains size. The correlation between the eigenvalue 3

and sodium occurred in the whole bag as well as in both sections, where it is strongest in section 501.

The microstructure mapping images show relaxation features in both sections although the elongation of the bubbles is stronger in section 201. Section 501 contains a greater variety of grain sizes but fewer bubbles. Section 201 shows a higher concentration of black dots which are located in clear bands that can be related to two peaks in the CFA data. Furthermore, the particles seem to be larger and tend to conglomerate. Comparing the Raman spectra, section 201 and 501 show an equal chemical composition of the black dots.

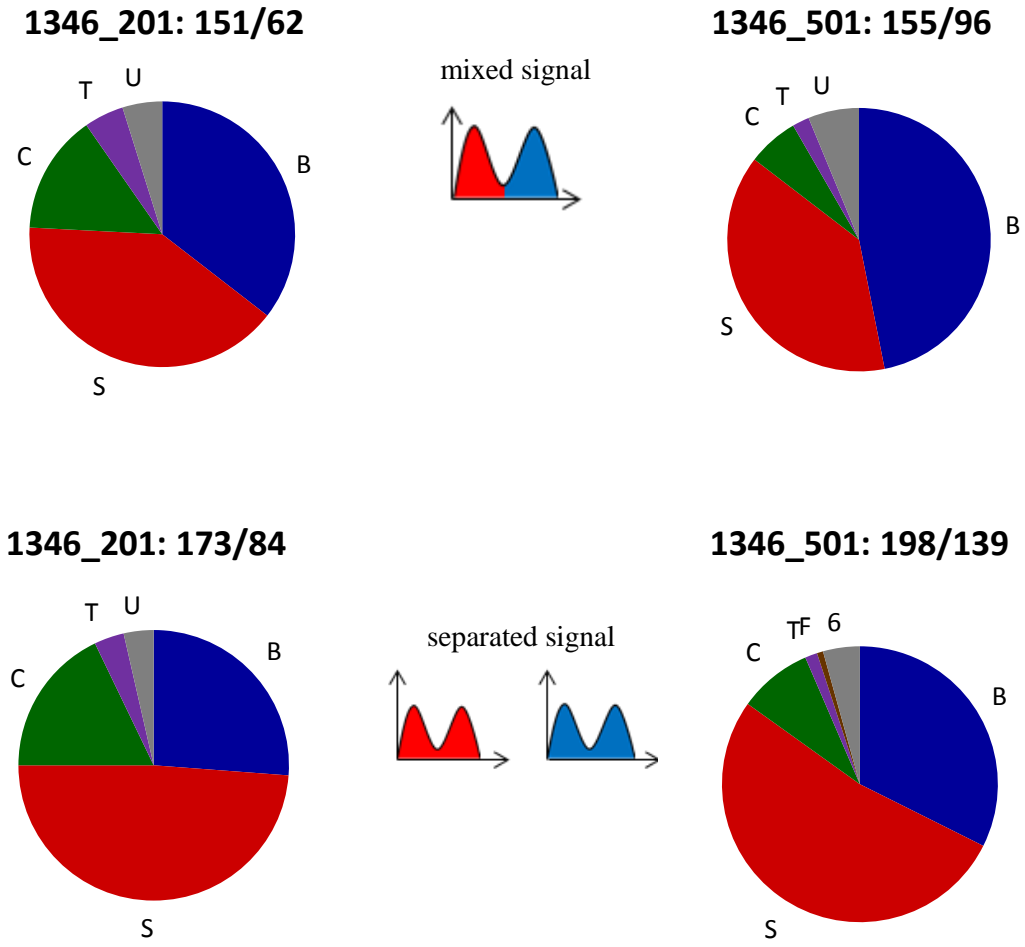


Fig. 31: Pie charts summarizing the results of section 201(left) and 501 (right) (mixed and separated signal)

Fig (31) presents the pie charts with the summarized results for each section as mixed and separated signals (see appendix 10.8). The major components are sulfate and black carbon, whereas black carbon almost always occurs as a mixed signal. Gypsum could just be identified in combination with black carbon. The sulfates often showed no clear signal so that they could not be identified in more detail. Within the group of silica particles, more plagioclase could be found in section 201 whereas more quartz was identified in section 501. The separated signals in both sections show a greater amount of sulfate than of black carbon and silica particles. In both sections some trace elements like titan oxides or metal hydroxides could be found as well as a small amount of unidentified particles. In section 501 more particles showed a spectrum than in section 201 which might be due to more practicing of the method. Generally, no carbonates were found and measurement along grain boundaries or at triple junctions also showed no spectra.

7. Discussion

7.1 Influence of the impurities on the microstructure

The main focus of this work is the identification of the impurities using Raman spectroscopy. A similar study by OYABU ET AL. (2015) who analyzed solid particles in the NEEM ice core using scanning electron microscope, energy dispersive X-ray spectroscopy (SEM-EDS) as well as Raman spectroscopy. One sample in this study from the Holocene period originating from 689,15 m depth (~3600 yrs old) can be compared with the analyzed section of bag 1346. For the sample chosen by OYABU ET AL (2015) 662 particles with a mean diameter of 2,25 μm were measured. 36,6 % of the particles could be identified as CaCO_3 , 11,1 % as CaSO_4 , 4,0 % as compounds containing calcium and chloride and 14,3 % Na_2SO_4 . 1,7 % of the particles contain sodium plus unknown compounds, 7,4 % contain sulfur, calcium and sodium and 8,6 % contain chloride, calcium and sodium. 1,7 % could not be identified. For this work, in total 306 particles were measured, whereas for 158 particles a spectrum could be obtained (see chapter 6.3 and 6.4). Similar to the results of OYABU ET AL. (2015), the sections 201 and 501 contain 24 % Na_2SO_4 and 7 % CaSO_4 . As a major difference, no carbonates were found. The different results might be due to the applied measuring techniques, since OYABU ET AL. (2015) used SEM-EDS technique, both methods operating on the surface of the sample, and

Raman spectroscopy after sublimation of the sample. Furthermore, Raman spectroscopy was only used to determine the compounds that contain calcium. For this work, the all particles were measured in situ with Raman spectroscopy. OYABU ET AL. (2014, 2015) state, that during the sublimation process, chemical reactions between acids and salts are unlikely to happen, since the number ratios of $\text{Na}_2\text{SO}_4/\text{CaSO}_4$ from the sublimation method to that from Raman method were checked with data from SAKURAI ET AL. (2011) and considered to match well (OYABU ET AL. 2014). Nevertheless, the compared ratios do not include all possible components, especially as the micro-Raman method by SAKURAI ET AL. (2011) is far from being quantitative. Thus, it can still be assumed, that different results are obtained due to the chosen methods. The identification of the Raman spectra also depends on the spectra used as a reference and might be more reliable with more than one matching peak as done by SAKURAI ET AL. (2011). Additionally, comparisons to data generated with other methods, like CFA, should be taken into account. Especially the absence of carbonates in our measurements inside the solid ice compared to the sublimation method by OYABU ET AL. (2015) may suggest formation of new compounds during sublimation, as carbonate in Greenlandic ice is known to be reduced by in-situ production of CO_2 (TSCHUMI & STAUFFER 2000). These reactions strongly depend on the acidity of the environment in the sample, which has to be evaluated (e.g. ANKLIN ET AL. 1995).

Since a variety of species could be identified, an approach was made to relate the fluctuations in plot to seasonal variations. The calcium and sodium peaks in both sections of bag 1346 indicate that this ice was accumulated during winter to spring season. Still, the different sources, ways of transport and probably residence times in the atmosphere have to be considered: dust particles mainly originate from Asian deserts whereas sodium is transported to Greenland from the surrounding oceans (e.g. FISCHER 2001, see chapter 3.4.2). Furthermore, the break in the bag that results in missing values and the depth shift of data makes it difficult to determine seasons. Ammonium as a summer signal (ANDERSEN ET AL. 2006) could not be found, neither as a solid particle nor located in grain boundaries or triple junctions, indicating that it might be incorporated in the lattice as described in chapter 3.4.4.

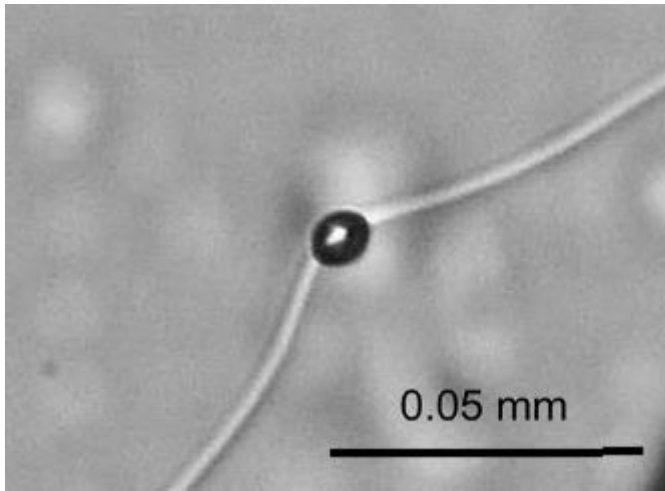


Fig. 32: Grain boundary pinning at a bubble (AZUMA ET AL. 2012)

Generally, no Raman spectra could be obtained in grain boundaries or triple junctions. Also no black dots could be determined visually to be located in those areas. Since the pinning effect is observed occurring with bubbles and clathrates (see fig. 32) (AZUMA ET AL. 2012), the black dots with an estimated size of 1-5 μm might be too small to have an impact on the grain boundaries directly. On the other hand, the grain

boundaries might be in a high velocity regime, so that dragging with release of impurities after some time rather than real pinning may occur. The impurities often appeared to be in conglomerates. The black dots that were part of such a conglomerate did not necessarily show the same spectrum, but could be of different chemical species. Since the compounds could spread after being hit by the laser, it was possible to measure the single compounds. Especially in section 201 two bands of impurities could be identified, which show a random composition of chemical species. No connection between the chemical species of the black dots and their location according to the ice microstructure could be determined. The observation that the black dots are rather close to bubbles than to grain boundaries is discussed in chapter 7.5. No carbonates were found. Regarding the organic compounds, two different species could be distinguished. One organic species was found on subgrain boundaries (or cracks) and is considered to be bacteria.

In the following the two major species (sulfate and black carbon) will be discussed in detail.

7.2 Sulfates

Most of the black dots that were measured with Raman could be identified as sulfates or mixtures of sulfates and black carbon. As described in chapter 3.4.2 sulfate can be used as a proxy for tephra layers and thus for volcanic eruptions (e.g. CLAUSEN ET AL. 1997). According to RASMUSSEN ET AL. (2013), five tephra horizons are determined for the NEEM ice core: at 1648,83 m depth, at 1615,48 m, 1664,90 m, 1677,55 m and at 1759,75 m, which also match with tephra horizons found in the NGRIP2 ice core. For the depth of bag 1346 (739,75 m-740,30 m) to exact matches could be found except for one layer in the GRIP ice

core at 736,63 m (age: approximately 3641 ± 3 yrs old), which is the only one close to the chosen bag (ABBOTT & DAVIES 2012; HAMMER ET AL. 2003). This layer was identified as originating from Aniakchak, a volcano located on the Aleutian Range of Alaska (ABBOTT & DAVIES 2012). Formerly, this layer was related to the Thera (Santorini) eruption (e.g. HAMMER ET AL. 1987; ZIELINSKI & GERMANI 1998) but after examining the geochemistry of the layer the results were reconsidered (e.g. KEENAN 2003; PEARCE ET AL. 2004). However, this tephra layer is mainly composed of SiO_2 , Al_2O_3 , TiO_2 , K_2O and other trace element (HAMMER ET AL. 2003), which do not match with results of this work, since the major components are sulfate and black carbon. The concentration of TiO_2 of the two sections of bag 1346 is considered to be too low to originate from a volcanic event (in total 5 particles that were identified as TiO_2 , could be found).

On the other hand, sulfate can originate from sea salt or biological activity (see chapter 3.4.2). Analyzing samples from Dome Fuji (East Antarctic Plateau), IIZUKA ET AL. (2013) state, that in the Holocene more than 90 % of the initial sea salt becomes sulfatized during the transport to Antarctica or in the first year after being precipitated due to the large amount of sulfuric acid in the Antarctic atmosphere (IIZUKA ET AL. 2013, IIZUKA ET AL. 2012, RÖTHLISBERGER ET AL. 2003). As observed by IIZUKA ET AL. (2013), samples from the early Holocene show, that sodium sulfate (Na_2SO_4), together with sodium chloride (NaCl) and calcium sulfate (CaSO_4) are the main components of soluble salts (see fig. 33). Fig. (33) also shows the summarized amount of sulfates obtained by Raman spectroscopy in comparison to the results of IIZUKA ET AL. (2013). Although the samples originate from different regions, parallels can be seen especially in the amount of sodium sulfate, so that similar processes occurring in Greenland can be assumed. Additionally, it has to be kept in mind that sodium chloride does not have Raman active modes and thus cannot be included in the pie chart of bag 1346. Considering sulfatization as a post-depositional process also explains, why sulfate was found almost equally distributed over both sections of bag 1346.

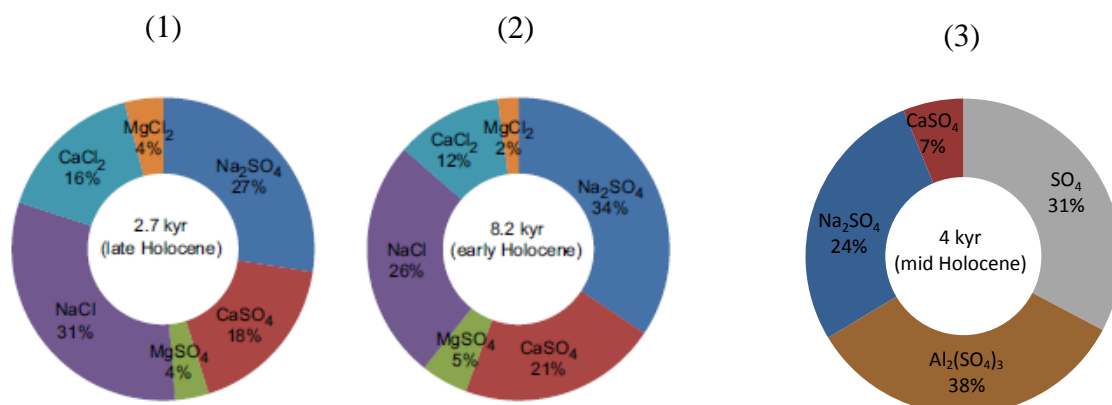


Fig. 33: Pie charts showing the results of Iizuka et al. (2013) (1 and 2) in comparison to the results of this work (3). Pie chart (3) shows the amount of sulfates of both sections 201 and 501 as separated signal.

Still, a large number of particles identified as sulfates could not be distinguished further since the Raman spectrum was too weak, so that the amount of sodium sulfate and calcium sulfate might be actually higher. On the other hand, the spectra could also be interpreted as phosphate compounds, a chemical species, that, similar to sulfate, can originate from multiple sources such as dust, sea salt, volcanoes and biogenic particles (KJER 2011). However, without clearer Raman spectra, the particles cannot be identified beyond any doubts.

7.3 Black Carbon

The black carbon found in both sections of the sample was almost equally distributed over all areas that were measured with Raman. Except for two particles, it was always found as a mixed signal. These mixed signals imply that particles of different chemical species can be internally mixed, as stated by LESINS ET AL. 2002. However, as black carbon is a product of incomplete combustion of biofuel, fossil fuel and open biomass burning (ANDREAE & CRUTZEN 1997; MING ET AL. 2008), it is initially emitted without any non-refractory material and in a hydrophobic state (WEINGARTNER ET AL. 1997, SCHWARZ ET AL. 2008b). After being exposed to the atmosphere, black carbon transforms into a hydrophilic state and thus gets internally mixed (or coated) with other materials such as sulfate or organic carbon compounds (SCHWARZ ET AL. 2008a). The result of this work that black carbon occurs in 97 % as a mixed signal can confirm these findings.

JACOBSON (2001) state, that 93 % of today's black carbon are mixed or coated with sulfate. According to LESINS ET AL. (2002) black carbon coexisting with sulfates occurs when it originates from fossil fuel burning, whereas it coexists with organic compounds when it is produced by biomass burning. Since the samples from bag 1346 are approximately 4000 years old (RASMUSSEN ET AL. 2013), wild fires in North America or Siberia are considered to be the source of black carbon (ZENNARO ET AL. 2014), which is contradicting to the obtained results of this work. Black carbon was mostly mixed with sulfates and, to some extent, with silica particles but never with organic compounds. Generally, only two different organic species were found (still to be characterized in more detail).

ZENNARO ET AL. (2014 & 2015) use Levoglucosan as a proxy for forest fires additionally to black carbon since this is a monosaccharide released during biomass burning when cellulose combustion occurs at temperatures $>300\text{ }^{\circ}\text{C}$ (GAMBARO ET AL. 2008). The increase of levoglucosan shown in fig. (34) marks the beginning of human activities altering fire regimes with a maximum at approximately 2,5 kyrs ago that is synchronous with extensive deforestation in Europe. The dashed black line marks the position of bag 1346. Since this is only the beginning of the human related burning events, more organic compounds might be expected in the following upper layers. Additionally, the high peak of the ammonium values at 739,86 m contributes to the theory of burning events. Furthermore, sulfate is one of the impurities with the highest concentration in ice due to its multiple sources (see chapter 3.4.2), and chemical compounds originating from different sources are presumed to mix in the atmosphere. Nevertheless, sulfates originating from volcanic eruptions might be related to black carbon emissions, since those eruptions can cause burning events in their surrounding areas. On the other hand, black carbon is considered to be injected into the atmosphere in convective smoke plumes residing there approximately 3 to 8 days (FLANNER ET AL. 2007; PARK ET AL. 2005), It can be questioned that the particles survive the long-range transport from remote areas of e.g. Siberia to Greenland in less than 3 days, especially since hydrophilic coatings on the particles reduce their lifetime and atmospheric loading, so that black carbon might not reach the stratosphere (STIER ET AL. 2006). However, source areas and residence time of black carbon should be reconsidered and deserve further research.

Furthermore, KEEGAN ET AL. (2014) state that black carbon sediments from Northern Hemisphere forest fires can be related to melt events occurred in Greenland in 1889 and 2012. With warm temperatures at the snow surface and without fresh accumulations, snow will age and thus change its morphology, which reduces the albedo about 14 % (FLANNER & ZENDER 2006). Additionally, black carbon can further reduce the albedo by up to 7 % (FLANNER ET

AL. 2007) and thus contribute to surface warming and accelerate melting processes (McCONNELL ET AL. 2007; JACOBSON 2001). According to SCHWARZ ET AL. (2007a) coatings can even enhance the light absorption. Since melt layers are characterized as compact, bubble-free layers (above the clathrate zone), the strong bands of impurities in section 201 containing black carbon cannot be related to melt events. Furthermore, Raman spectroscopy is a qualitative method and not appropriate to determine overall concentrations of impurities so that it is difficult to estimate the influence of black carbon on the melting process.

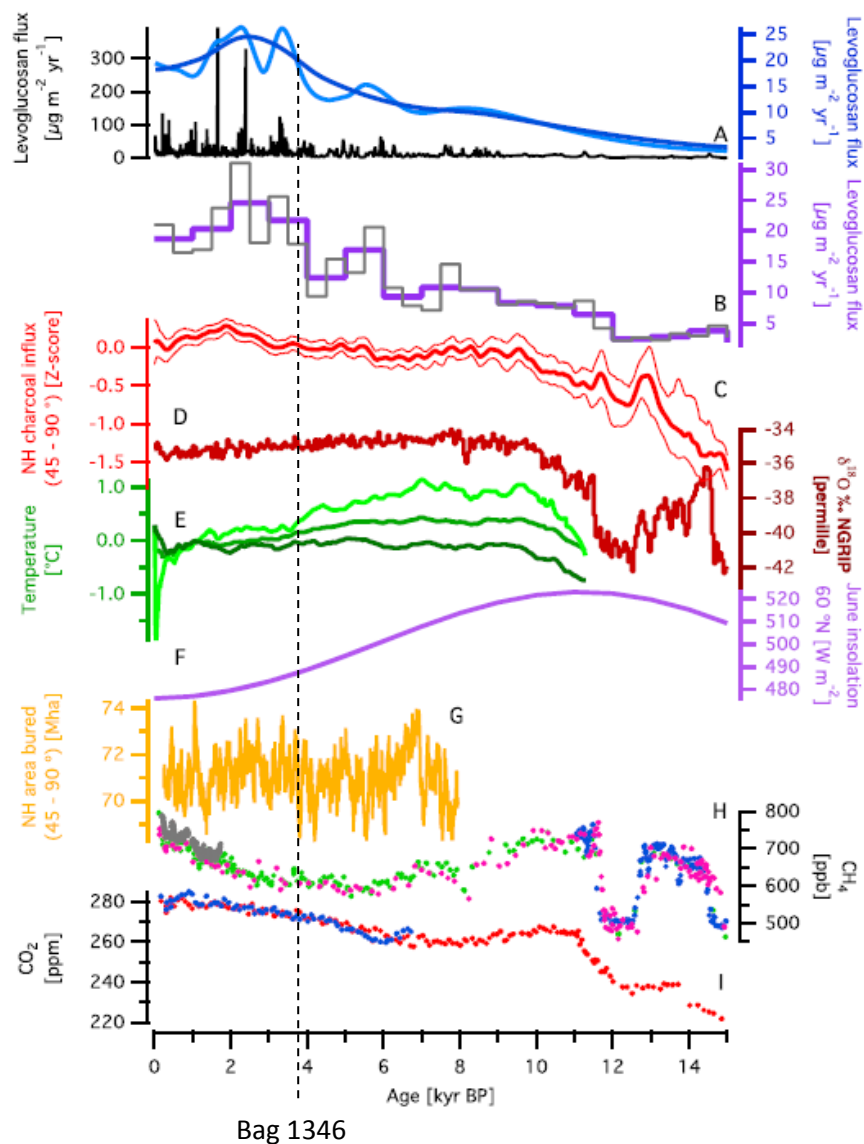


Fig. 34: Levoglucosan flux, northern hemisphere charcoal influx, temperature, June insolation, modeled burned area for high latitudes, preindustrial CH₄ flux and atmospheric CO₂ concentration over the last 15kyr (ZENARO ET AL. 2015). The dashed black line marks the position of bag 1346.

Generally, black carbon and also sulfate are equally distributed over both sections, so that they cannot be related to certain emission events. The layers of high impurity content do not show any chemical species as a dominant compound but are always a mixture of several different kinds. This indicates that the layers featuring a high impurity concentration might be related to precipitation events causing a wash-out of aerosols from the atmosphere, thus the bands would reflect the average aerosol content of the atmosphere in the Holocene according to the prevailing season.

7.4 Raman spectroscopy

Generally, Raman spectroscopy can be considered as an appropriate method for analyzing impurities in polar ice, since it is non-destructive and impurities can be identified in-situ. On the other hand, the measuring procedure, including searching the particles, focusing and shifting into the Raman mode is very time-consuming so that representative statistics are difficult to obtain in the time that is set for a master thesis. Automating the procedure would help such that changing the optical path from imaging to laser including a short walk into the ice laboratory where the Raman is situated is necessary.

Furthermore, the CrystalSleuth software refers to the spectra library of the the RRUFF database, which contains some spectra of minor quality and many components or minerals that are unlikely to find in glacier ice and thus beyond the scope of his work. Additionally, the correct identification strongly depends on the curve fitting and background correction. Raman bands can show a small offset due to the pressure in the ice crystal. Besides, some molecules, which are essential for interpreting impurities in polar ice, do not have Raman active bands (e.g. NaCl) and thus cannot be measured. Another problem is that some particles tend to move during measurements since the laser can cause local heating.

Despite these limitations, Raman spectroscopy is a useful tool to contribute to data obtained by CFA and thus get a better overview over the impurities in glacier ice, especially because particles do not get dissolved or mixed during the melting process included in the CFA method.

7.5 Relaxation

After selecting samples by correlation of CFA data and microstructure parameters, microstructure mapping images were taken in order to visually locate and count the impurities. Generally, it is difficult to assess the position of the impurities relative to the grain boundaries, since relaxation processes altered the ice microstructure. Fig. (35) shows the LASM image for section 201 of bag 1346 that was taken shortly after drilling on-site (left) and the microstructure mapping image taken for this work (right). The dashed red lines mark the part of the sample which was used for the microstructure mapping and Raman spectroscopy. LASM (Large Area Scanning Microscope) is a newly established method of optical microscopy using directed bright-field illumination so that subgrain and grain boundary features can be documented (BINDER ET AL. 2013). According to SHOJI & LANGWAY (1983), volume relaxation of preexisting air bubbles in natural glacier ice is a result of basal and non-basal slip of ice crystals after cracks are initiated due to the hydrostatic pressure difference between air bubble and atmospheric pressure. Stresses in ice caused by the overburden pressure of the covering snow and ice layers tend to become relieved when the load is removed by drilling (GOW 1971). The images in fig. (36) both show section 201 of bag 1346. In the microstructure mapping image of fig. (35) it can be seen that layers of high bubble concentration developed (marked with red arrows), which do not occur in the LASM image of fresh ice. One reason for this is that LASM is mainly a surface imaging method, while microstructure mapping using a light microscope (even in reflection) images a certain sample depth due to a rather large depth of sharpness.

LASM: bag 1346_201

Microstructure map: bag 1346_201

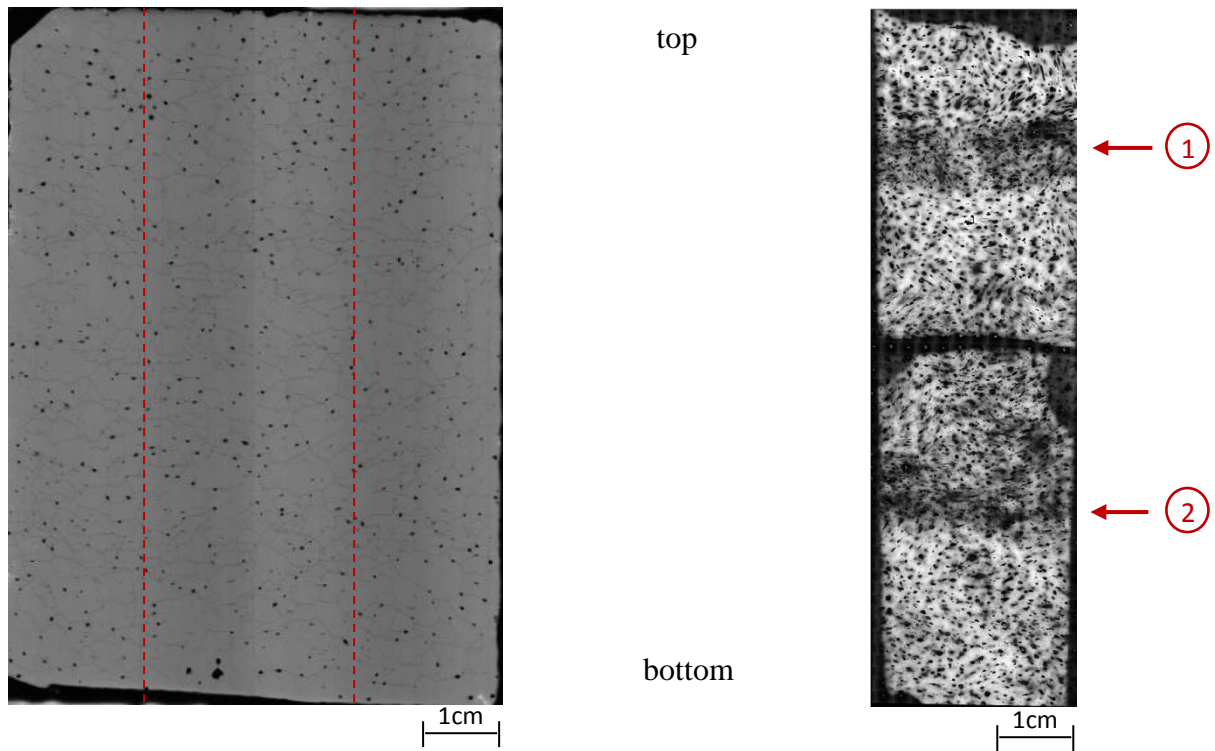


Fig. 35: The LASM image (left) in comparison to the microstructure map (right) of bag 1346_201. The red lines in the LASM image mark the part from which the microstructure map was obtained.

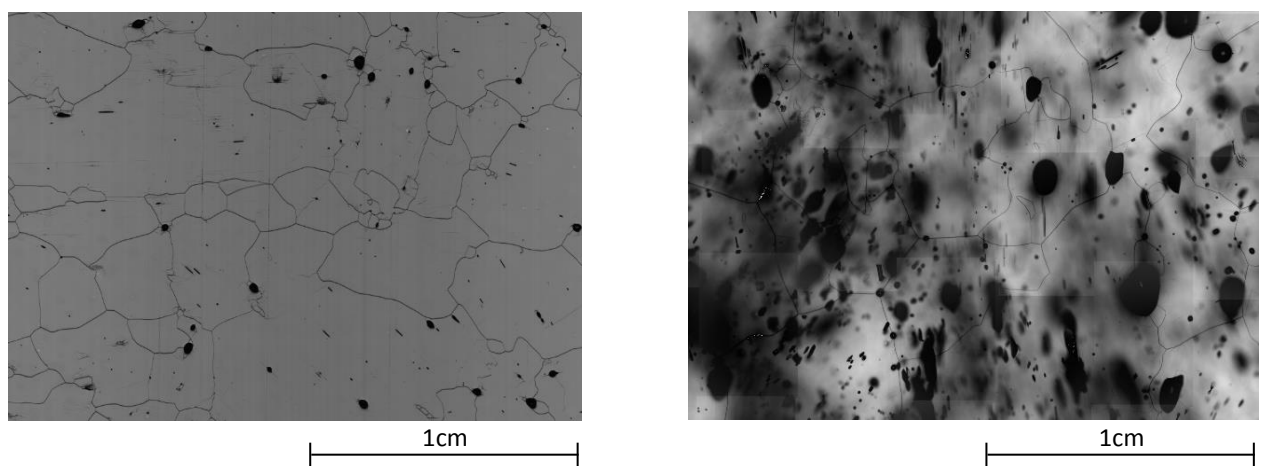


Fig. 36: A LASM image and a microstructure map of bag 1346_201 showing details of microstructural features

The images in fig do not show exactly the same sample area, since microtoming altered the surface of the sample. However, the comparison gives an impression of the changes in the ice microstructure as a result of relaxation. At first glance, the impurities seemed to be closer to bubbles than to grain boundaries, although these findings have to be reconsidered in terms of growing bubbles due to relaxation. Still, it can be assumed that relaxation processes might be influenced not only by pressure differences but also by impurity concentration. Section 201 features higher impurity content as well as a higher concentration of bubbles than section 501. Except for layer (2) in section 201 the bubble layers match with the areas of high concentration of impurities (see appendix 10.7). Since relaxation is initiated by cracks as a result of pressure differences and impurities can cause defects (e.g. dislocations, see chapter 3.3) in the crystal structure, these cracks might develop in areas of high impurity concentration. The mismatching of layer (2) might be caused by deformation processes or is simply a result of different impurity distributions that might be revealed in different foci depths of this section as shown in fig. (37), since impurity layers (also cloudy bands) can be tilted. Some bubbles can still be seen at the surface whereas it is necessary to zoom in to the sample to observe the impurities.

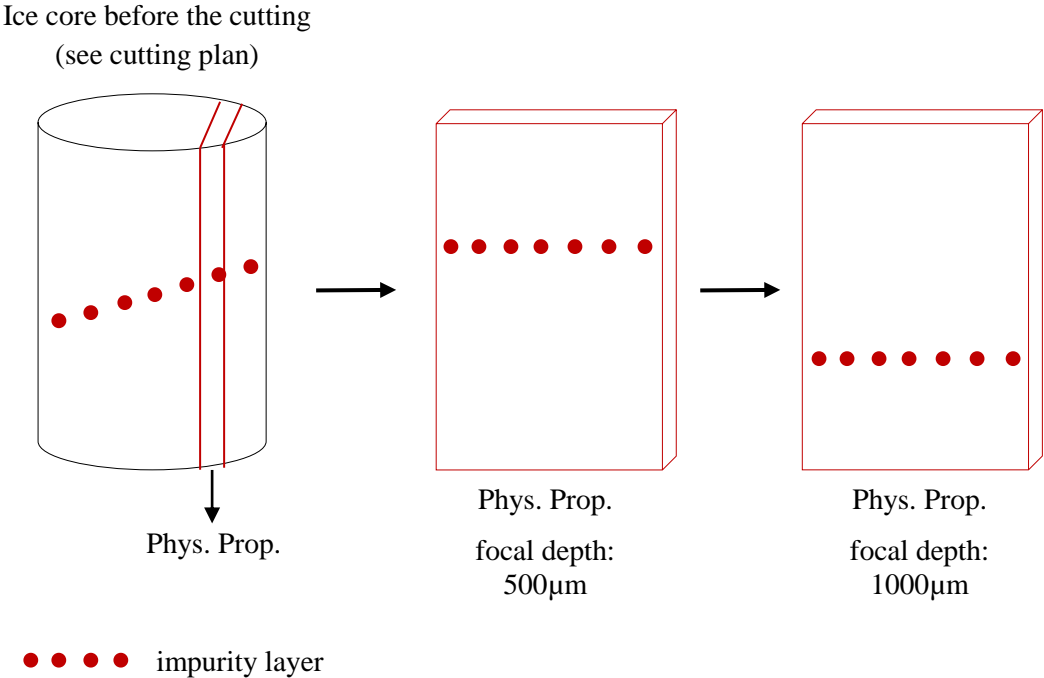


Fig. 37: Schematic drawing of the location of impurity layer n a sample in relation to different focal depths

Nevertheless, the location of impurities relative to the grain boundaries cannot be determined exactly by visual inspection of the microstructure mapping images due to those relaxational features.

7.6 Possible sources of errors

As a first step in the flow of this study, correlation coefficients were calculated between the chemical parameters and the mean grain size and eigenvalue 3, respectively (see KLEITZ 2013). Since irregularities in the depth scale of the CFA-data can occur, cross correlations were calculated in order to estimate the shift. The results (see appendix 10.5) show that the shift varies significantly within one bag. Fig. (38) shows the data for the mean grain size and dust of section 1346_201 with a shift of 17 mm (derived from the cross correlations, see appendix 10.5).

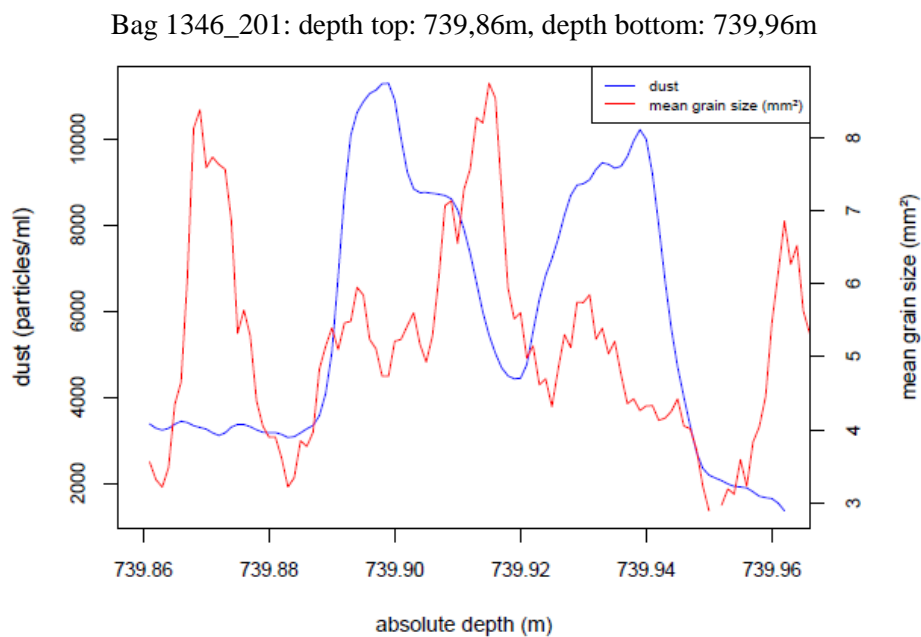


Fig. 38: Bag 1346_201: plot of dust and mean grain size with a shift of 17mm

Tab. 5: The correlation coefficients for bag 1346_201 calculated with a shift of 17 values. The blue colour marks the significant correlations (significance level 95%)

	dust	conductivity	natrium	calcium	ammonium	nitrate
mean grain size	0.314	0.107	0.318	0.413	-0.286	0.190
eigenvalue 3	-0.033	-0.246	0.424	0.458	-0.164	0.365

Visually, no correlations can be found even after shifting the data. Table (5) shows the correlations coefficients (*Spearman's Rho*) with a constant shift for section 201. Compared to correlations without the shift (see appendix 10.4), the parameters showing significant correlations changed. Thus, it can be stated that the shift occurs in the values for dust but not necessarily for the other components, as the meltwater during the CFA measurements is separated to different tubes leading to the measuring devices (see chapter 5.2). Since the data for the melt speed were not available, the irregularities in the depth scale can hardly be estimated.

Shifts in depth between the different data sets can be related to the cutting of the ice core. The cutting plan for the NEEM ice core (see fig. 39) shows that for the data records analyzed in this study measurements were on different pieces of the core. For the CFA, molten ice from the inner part of an ice core “stick” is analyzed, whereas for the physical properties and the Raman measurements small sections from the edge of the core are used. In terms of microstructure and impurities large differences can occur on smallest microscale areas. Furthermore, impurity layers in the core can be tilted due to deformation, but the cores can only be analyzed in sections parallel to the longitudinal axis of the core.

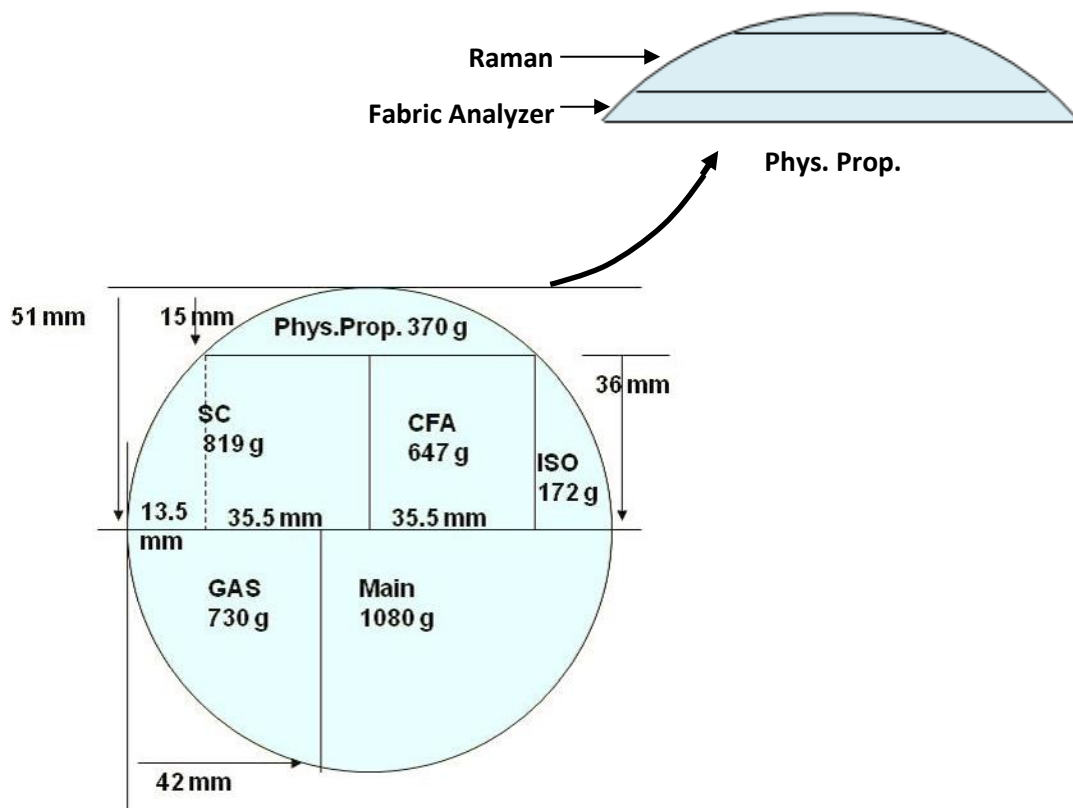


Fig. 39: The cutting plan for the NEEM ice core (NEEM FIELD SEASON 2010).

Also the cut-off during the preparation of the thin sections is not documented and it can be questioned whether the position of the added NaN's as described in chapter, is correct. There still might be correlations between the measured parameters, thus it is essential to improve and combine the measuring techniques in order to reveal these relations.

8. Summary and outlook

The aim of this work was to determine the location and chemical species of the impurities by using optical microscopy and Raman spectroscopy. Therefore, two sections of the NEEM ice core from a depth of 739,75 m to 740,30 m (bag 1346) were chosen, according to their special features shown the data from the Fabric Analyzer and CFA. Microstructure mapping images were taken for both samples and used to label and count the black dots. The black dots could

then be searched and measured in-situ with Raman spectroscopy. The two sections show a similar composition of impurities, with the main components being identified as sulfates, black carbon, silica particles and other trace species. Sulfate is considered to originate mainly from sea salt, generated by sulfatization of other inorganic compounds (IIZUKA ET AL. 2013), since the comparison with tephra layers as another possible source does not lead to matching results (ABBOTT & DAVIES 2012). Black carbon, which is mostly related to wildfires occurring in North America or Siberia (ZENARO ET AL. 2014), can be identified in mixed Raman spectra but does not imply the occurrence of burning events, since it is equally distributed over both samples. In areas of high impurity concentration no chemical species could be identified as the dominant one, so that these layers might be caused by wash-out events and thus representing the average aerosol content of the atmosphere. In contrast to previous studies (e.g. OYABU ET AL. 2015) no carbonates were found.

One to two thirds of the measured particles did not show a Raman spectrum which can be due to the fact, that e.g. NaCl does not have Raman active bands but is a major component of the impurities found in the Greenland ice sheet. Another reason might be the moving of particles due to local heating caused by the laser. Generally, no spectra could be obtained from grain boundaries or triple junctions and no pinning effect was observed.

In order to improve the statistics for the impurities found in the NEEM ice core, it is necessary to analyze more samples from different depths, especially to compare Holocene ice with samples from glacial periods. Comparisons between different ice cores should also be taken into account. Therefore, an improvement of the measuring procedure of Raman spectroscopy is essential, since the searching of particles, focusing and changing to the Raman mode is very time-consuming. Automating the system so that the focusing and changing to the Raman mode is done independently could save time and would enable to measure a statistically significant number of particles. Furthermore, the same amount of particles should be measured in every area, so that reliable comparisons can be drawn.

To confirm the finding of the organic compounds, it would be necessary to obtain a Raman spectrum of the drilling liquid used in the NEEM field campaign to exclude contamination. Additionally, Raman spectroscopy should be used to determine whether the impurity content of an ice sample differs before and after sublimation. The size of the impurities can be determined by applying the coulter counter. In general, it is of great importance to combine the measuring techniques of the physical and chemical parameters so that the same piece of the ice core is used to improve the comparability on the depth scale.

Data of future drilling projects (e.g. E-GRIP) will provide further chances to analyze the location and influence of impurities in ice.

9. References

ABBOTT, P.M.; DAVIES, S.M. (2012): Volcanism and the Greenland ice-cores: the Tephra record, *Earth-Science Reviews*, 115, pp. 173-191, doi: 10.1016/j.earscirev.2012.09.001

ALLEY, R.B.; PEREPEZKO, J. H.; BENTLEY, C. R. (1986): Grain growth in polar ice: I. Theory, *Journal of Glaciology*, 32, pp. 415-425

ALLEY, R.B. (1987): Firn densification by grain-boundary sliding: A first model, *Journal de Physique Colloques*, 48, pp. C1-249 – C1-256, doi: 10.1051/jphyscol:1987135

ALLEY, R.B. (1988): Fabrics in Polar Ice Sheets: development and prediction, *Science*, 240, p.493

ALLEY, R. B. (1992): Flow-law hypothesis for ice-sheet modeling, *Journal of Glaciology*, 38, 245-256

ALLEY, R. B. & WOODS, G. A. (1996): Impurity influence on normal grain growth in the GISP2 ice core, Greenland, *Journal of Glaciology*, 42, pp. 255-260

ANDREAE, M.O.; CRUTZEN, P.J. (1997): Atmospheric Aerosols: Biochemical Source and Role in Atmospheric Chemistry, *Science*, 276, pp. 1052-1058

ANDERSEN, K.K.; SVENSSON, A.; JOHNSEN, S.J.; RASMUSSEN, S.O.; BIGLER, M.; RÖTHLISBERGER, R.; RUTH, U.; SIGGARD-ANDERSEN, M.L.; STEFFENSEN, J.P.; DAHL-JENSEN, D.D.; VINTHER, B.M.; CLAUSEN, H.B. (2006): The Greenland Ice Core Chronology 2005, 15-42 ka. Part I: constructing the time scale, *Quaternary Science Reviews*, 25, pp. 3246-3257, doi:10.1016/j.quascirev.2006.08.002

ANKLIN, M.; BARNOLA, J.M.; SCHWANDER, J.; STAUFFER, B.; RAYNAUD, D. (2002): Processes affecting the CO₂ concentration measured in Greenland ice, *Tellus B*, 47, pp. 461-470, doi: 10.1034/j.1600-0889.47.issue4.6.x

AULT, A.P.; ZHAO, D.; EBBEN, C.J.; TAUBER, M.J.; GEIGER, F.M.; PRATHER, K.A.; GRASSIAN, V.H. (2013): Raman microscopy and vibrational sum frequency generation spectroscopy as probes of the bulk and surface compositions of size-resolved sea spray aerosol particles. *Physical Chemistry Chemical Physics*, 15, pp. 6206-6214, doi: 10.1039/c3cp43899f

AZUMA, N.; MIYAKOSHI, T.; YOKOYAMA, S.; TAKATA, M. (2012): Impeding effect of air bubbles on normal grain growth of ice, *Journal of Structural Geology*, 42, pp. 184-193, doi:10.1016/j.jsg.2012.05.005

BAKER, I.; CULLEN, D. (2003): SEM/EDS observations of impurities in polar ice: artefacts or not?, *Journal of Glaciology*, 49, pp. 184-190, doi:10.3189/172756503781830773

BARLETTA, R.E.; PRISCU, J.C.; MADERM, H.M.; JONES, W.L.; ROE, C.H. (2012): Chemical analysis of ice vein microenvironments: II. Analysis of glacial samples from Greenland and Antarctica, *Journal of Glaciology*, 58, pp. 1109-1118, doi: 10.3189/2012JoG12J112

BARNES, P.R.F. (2002): Comment on “Grain boundary ridge on sintered bonds between ice crystals” [Journal of Applied Physics, 90, 5782 (2001)], Journal of Applied Physics, 93, pp. 783-785, doi: 10.1063/1.1521800

BARNES, P.R.F.; WOLFF, E.W. (2004): Distribution of soluble impurities in cold glacial ice, Journal of Glaciology, 50, pp. 311-324, doi: 10.3189/172756504781829918

BARRIE, L. A. (1985): Atmospheric particles: Their physical and chemical characteristics and deposition processes relevant to the chemical composition of glaciers, Annals of Glaciology, 7, pp. 100-108

BERGER, H.; TANG, H.; LÉVY, F. (1993): Growth and Raman spectroscopic characterization of TiO₂ anatase single crystals, Journal of Crystal Growth, 130, pp. 108-112, doi:10.1016/0022-0248(93)90842-K

BEYSSAC, O.; GOFFÉ, B.; PETITET, J.P.; FROIGNEUX, E.; MOREAU, M.; ROUZAUD, J.N. (2002): On the characterization of disordered and heterogeneous carbonaceous material by Raman spectroscopy, Spectrochimica Acta Part A, 59, pp. 2267-2276, doi: 10.1016/S1386-1425(03)00070-2

BIGLER, M.; WAGENBACH, D.; FISCHER, H.; KIPFSTUHL, J.; MILLER, H.; SOMMER, S.; STAUFFER, B. (2002): Sulphate record from a northeast Greenland ice core over the last 1200 years based on continuous flow analysis, Annals of Glaciology, 35, pp. 250-256, doi: 10.3189/172756402781817158

BIGLER, M.; SVENSSON, A.; STEFFENSEN, J.P.; KAUFMANN, P. (2007): A new continuous high-resolution detecting system for sulphate in ice cores, Annals of Glaciology, 45, pp. 178-182 doi: 10.3189/172756407782282471

BINDER, T.; GARBE, C.S.; WAGENBACH, D.; FREITAG, J.; KIPFSTUHL, S. (2013): Extraction and parametrization of grain boundary networks in glacier ice, using a dedicated method auf automatic image analysis, *Journal of Microscopy*, 250, pp. 130-141, doi: 10.1111/jmi.12029

BISCAYE, P.E.; GROUSSET, F.E.; REVEL, M.; VAN DER GAAST, S.; ZIELINSKI, G.A.; VAARS, A.; KUKLA, G. (1997): Asian provenance of glacial dust (stage 2) in the Greenland Ice Sheet Project 2 Ice Core, Summit, Greenland, *Journal of Geophysical Research*, 102, pp. 26,765-26,782, doi: 10.1029/97JC01249

BLACKFORD, J. R. (2007): Sintering and Microstructure of ice: a review, *Journal of Physics D: Applied Physics*, 40, pp. R355-R385. doi:10.1088/0022-3727/40/21/R02

BLUNIER, T.; SCHWANDER, J. (2000): Gas enclosure in ice: age difference and fractionation, *Physics of Ice Core Records*, Hokkaido University Press, pp. 307-326

BORY, A. J.-M.; P. E. BISCAYE; A. M. PIOTROWSKI ET AL. (2003): Regional variability of ice core dust composition and provenance in Greenland, *Geochemistry, Geophysics, Geosystems*, 4, p. 1107, doi:10.1029/2003GC000627

BURAKHAM, R.; HIGUCHI, K.; OSHIMA, M.; GRUDPAN, K.; MOTOMIZU, S. (2004): Flow injection spectrophotometry coupled with a crushed barium sulfate reactor column for the determination of sulfate ion in water samples, *Talanta*, 64, pp. 1147-1150, doi: 10.1016/j.talanta.2004.05.001

BURT, J. E.; BARBER, G. M. (1996): *Elementary Statistics for Geographers*, 2nd ed., pp. 383-412; New York (The Guilford Press)

CASTERLNAU, O.; DUVAL, P.; LEBENSOHN, R.A.; CANOVA, G.R. (1996): Viscoplastic modeling of texture development in polycrystalline ice with a self-consistent approach: Comparison with bound estimates, *Journal of Geophysical Research*, 101, pp. 13851-13868, doi: 10.1029/96JB00412

CLAUSEN, H.B.; HAMMER, C.U.; HVIDBERG, C.S.; DAHL-JENSEN, D.; STEFFENSEN, J.P.; KIPFSTUHL, J.; LEGRAND, M. (1997): A comparison of the volcanic records over the past 4000 years from the Greenland Ice Core Project and Dye 3 Greenland ice cores, *Journal of Geophysical Research*, 102, pp. 26,707-26,723, doi: 10.1029/97JC00587

COLE-DAI, J.; BUDNER, D.M.; FERRIS, D.G. (2006): High speed, high resolution, and continuous chemical analysis of ice cores using a melter and ion chromatography, *Environmental Science and Technology*, 40, pp. 6764-6769, doi: 10.1021/es061188a

CUFFEY, K. M. & PATERSON, W. S. B. (2010): *The Physics of Glaciers*, 4th ed., pp. 11-27; Elsevier

CULLEN, D.; BAKER, I. (2000): Correspondence. The chemistry of grain boundaries in Greenland ice, *Journal of Glaciology*, 46, pp. 703-706, doi: 10.3189/172756500781832783

CULLEN, D.; BAKER, I. (2001): Observations of impurities in ice, *Microscopy Research and Technique*, 55, pp. 198-207, doi: 10.1002/jemt.10000

DAMOAH, R.; SPICHTINGER, N.; FORSTER, C.; JAMES, P.; MATTIS, I.; WANDINGER, U.; BEIRLER, S.; WAGNER, T.; STOHL, A. (2004): Around the world in 17 days – hemispheric-scale transport of forest fire smoke from Russia in May 2003, *Atmosphere Chemistry and Physics*, 4, pp. 1311-1321, doi: 10.5194/acp-4-1311-2004

DASH, J.G.; FU, H.; WETTLAUFER, J.S. (1995): The premelting of ice and its environmental consequences, *Reports on Progress in Physics*, 58, pp. 115-167

DELLA LUNGA, D.; MÜLLER, W.; RASMUSSEN, S.O.; SVENSSON, A. (2014): Location of cation impurities in NGRIP deep ice revealed by cryo-cell UV-laser-ablation ICPMS, *Journal of Glaciology*, 60, pp. 970- 988, doi: 10.3189/2014JoG13J199

DELMAS, R.; BOUTRON, C. (1977): Sulfate in Antarctic Snow: Spatio-temporal Distribution, *Atmospheric Environment*, 12, pp. 723-728, doi: 10.1016/0004-6981(78)90253-6

DIBB, J.E.; JAFFREZO, J.L.; LEGRAND, M. (1992): Initial findings of recent investigations of air-snow relationships in the Summit region of the Greenland ice sheet, *Journal of Atmospheric Chemistry*, 14, pp. 167-180, doi: 10.1007/BF00115232

DANSGAARD, W.; JOHNSEN, S.J.; CLAUSEN, H.B.; DAHL-JENSEN, D.; GUNDESTRUP, N.S.; HAMMER, C.U.; HVIDBERG, C.S.; STEFFENSEN, J.P.; SVEINBJÖRNDOTTIR, A.E.; JOUZEL, J.; BOND, G. (1993): Evidence for general instability of past climate from 250-kyr ice core record, *Nature*, 364, pp. 218-220, doi:10.1038/364218a0

DURICKOVIC, I; CLAVERIE, R.; BOURSON, P.; MARCHETTI, M.; CHASSOT, J.M.; FONTANA, M.D. (2010): Water-ice phase transition probed by Raman spectroscopy, *Journal of Raman Spectroscopy*, 42, pp. 1408-1412, doi: 10.1002/jrs.2841

DUVAL, P. & CASTELNAU, O. (1995): Dynamic Recrystallization of Ice in Polar Ice Sheets, *Journal de Physique IV*, 5, pp. 197-205, doi: 10.1051/jp4:1995317

DUVAL, P. & MONTAGNAT, M. (2000): Rate controlling processes in the creep of polar ice, influence of grain boundary migration associated with recrystallization, *Earth and Planetary Science Letters*, 183, pp. 179-186, doi:10.1016/S0012-821X(00)00262-4

EICHLER, J. (2013): C-Axis Analysis of the NEEM ice core. An approach based on digital image processing, Alfred-Wegener-Institut für Polar- und Meeresforschung, Bremerhaven.

EISEN, O. (2007): Direct evidence for continuous radar reflector originating from changes in crystal-orientation fabric, *The Cryosphere*, 1, pp. 1-10, doi: 10.5194/tc-1-1-2007

FARIA, S. H.; FREITAG, J., KIPFSTUHL, S. (2010): Polar ice structure and the integrity of ice-core paleoclimate records, *Quaternary Science Reviews*, 29, pp. 338-351, doi: 10.1016/j.quascirev.2009.10.016

FARIA, H.S.; WEIKUSAT, I.; AZUMA, N. (2014a): The microstructure of polar ice. Part I: Highlights from ice core research, *Journal of Structural Geology*, 61, pp. 2-20, doi: 10.1016/j.jsg.2013.09.010

FARIA, H.S.; WEIKUSAT, I.; AZUMA, N. (2014b): The microstructure of polar ice. Part II: State of the art, *Journal of Structural Geology*, 61, pp. 21-49, doi: 10.1016/j.jsg.2013.11.003

FISCHER, H.; WAGENBACH, D. (1996): Large-scale spatial trends in recent firn chemistry along an east-west transect through central Greenland, *Atmospheric Environment*, 30, pp. 3227-3238, doi:10.1016/1352-2310(96)00092-1

FISCHER, H.; WAGENBACH, D.; KIPFSTUHL, J. (1998): Sulfate and nitrate firn concentrations on the Greenland ice sheet. 2. Temporal anthropogenic deposition changes, *Journal of Geophysical Research*, 103, pp. 21,935-21942, doi: 10.1029/98JD01885

FISCHER, H. (2001): Imprint of large-scale atmospheric transport patterns on sea-salt records in northern Greenland ice cores, *Journal of Geophysical Research*, 106, pp. 1-8, doi: 10.1029/2000JD000175

FISCHER, H.; SIGGAARD-ANDERSEN, M.-L.; RUTH, U. ET AL. (2007): Glacial/Interglacial changes in mineral dust and sea-salt records in polar ice cores: sources, transport, and deposition, *Reviews of Geophysics*, 45, RG1002, doi: 10.1029/2005RG000192

FLANNER, M.; ZENDER, C. (2006): Linking snowpack microphysics and albedo evolution, *Journal of Geophysical Research*, 111, D12208, doi: 10.1029/2005JD006834

FLANNER, M.G.; ZENDER, C.S.; RANDERSON, J.T.; RASCH, P.J. (2007): Present-day climate forcing and response from black carbon in snow, *Journal of Geophysical Research*, 112, D11202, doi: 10.1029/2006JD008003

FOSSEN, H. (2011): *Structural Geology*, 3rd ed., pp. 203-216; Cambridge (Cambridge University Press)

FUHRER, K.; NEFTEL, A.; ANKLIN, M.; MAGGI, V. (1993): Continuous measurements of hydrogen peroxide, formaldehyde, calcium and ammonium concentrations along the new grip ice core from summit, Central Greenland. *Atmospheric Environment*, 27, pp. 1873-1880, doi: 10.1016/0960-1686(93)90292-7

FUHRER, K.; WOLFF, E.W.; JOHNSEN, S.J. (1999): Timescales for dust variability in the Greenland Ice Core Project (GRIP) ice core in the last 100,000 years, *Journal of Geophysical Research*, 104, pp. 31,043-31,052, doi: 10.1029/1999JD900929

FUKAZAWA, H.; SUGIYAMA, K.; MAE, S.; NARITA, H.; HONDOH, T. (1998): Acid ions at triple junction of Antarctic ice observed by Raman scattering, *Geophysical Research Letters*, 25, pp. 2845-2848, doi: 10.1029/98GL02178

GAMBARO, A.; ZANGRANDO, R.; GABRIELLI, P.; BARBANTE, C.; CESCONE, P. (2008): Direct determination of levoglucosan at the picogram per milliliter level in Antarctic ice by high-performance liquid chromatography/electrospray ionization triple quadrupole mass spectrometry, *Annals of Chemistry*, 80, pp. 1649-1655, doi: 10.1021/ac701655x

GLENN, J.W. (1955): The creep of polycrystalline ice, *Proceedings of the Royal Society*, 228, pp. 519-538, doi: 10.1098/rspa.1955.0066

GOW, A.J. (1971): Relaxation of Ice in Deep Drill Cores from Antarctica, *Journal of Geophysical Research*, 76, pp. 2533-2541

HAMMER, C.U.; CLAUSEN, H.B.; FRIEDRICH, W.L.; TAUBER, H. (1987): The Minoan eruption of Santorini in Greece dated to 1645 BC?, *Nature*, 328, pp. 517-519, doi: 10.1038/328517a0

HAMMER, C.U.; KURAT, G.; HOPPE, P.; GRUM, W.; CLAUSEN, H.B. (2003): Thera eruption date 1645 BC confirmed by new ice core data? In: Bietak, M. (Ed.), *The Synchronization of Civilization in the Eastern Mediterranean*, Austrian Academy of Science, Vienna, pp. 87-94

HOBBS, P.V. (1974): *Ice Physics*. Oxford: Clarendon Press

HODKIEWICZ, J. (2010): Characterizing Carbon Material with Raman Spectroscopy, Thermo Fisher Scientific, Madison, WI, USA

HOOKE, R. LEB. (1998): Principles of Glacier Mechanics, pp. 13-64, Upper Saddle River/New Jersey (Prentice Hall)

HÖRHOLD, M. W.; LAEPPLER, T.; FREITAG, J. ET AL. (2012): On the impact of impurities on the densification of polar firn, Earth and Planetary Science Letters 325-326, pp. 93-99, doi: 10.1016/j.epsl.2011.12.022

HUA, L. (1999): An integrated wind erosion modeling system with emphasis on dust emission and transport, University of New South Wales

HUEN, J.; WEIKUSAT, C.; BAYER-GIRALDI, M.; WEIKUSAT, I.; RINGER, L.; LÖSCHE, K. (2014): Confocal Raman microscopy of frozen bread dough, Journal of Cereal Science, 60, pp. 555-560, doi: 10.1016/j.jcs.2014.07.012

HUTTERLI, M. A.; CRUEGER, T.; FISCHER, H. ET AL. (2006): The influence of regional circulation patterns on wet and dry mineral dust and sea salt deposition over Greenland, Climate Dynamics, 28, pp. 635-647, doi: 10.1007/s00382-006-0211-z

INTERNATIONAL PANEL ON CLIMATE CHANGE (2013): Climate Change 2013. The Physical Science Basis, Cambridge University Press

IZUKA, Y.; TSUCHIMOTO, A.; HOSHIMA, Y.; SAKURAI, T.; HANSSON, M.; KARLIN, T.; FUJITA, K.; NAKAZAWA, F.; MOTOYAMA, H.; FUJITA, S. (2012): The rates of sea salt sulfatization in the atmosphere and surface snow of inland Antarctica, *Journal of Geophysical Research*, 117, D04308, doi: 10.1029/2011JD016378

IZUKA, Y.; DELMONTE, B.; OYABU, I.; KARLIN, T.; MAGGI, V.; ALBANI, S.; FUKUI, M.; HONDOH, T.; HANSSON, M. (2013): Sulphate and chloride aerosols during Holocene and last glacial periods preserved in Talos Dome Ice Core, a peripheral region of Antarctica, *Tellus B*, 20197, doi: 10.3402/tellusb.v65i0.20197

JACKA, T. H. & JUN, L. (2000): Flow rates and crystal orientation fabrics in compression of polycrystalline ice at low temperatures and stresses, In: HONDOH, T. (ed.): *Physics of Ice Core Records*: 83-102, Hokkaido University Press

JACOBSON, M.Z. (2001): Strong radiative heating due to the mixing state of black carbon in atmospheric aerosols, *Letters to Nature*, 409, pp. 695-697, doi: 10.1038/35055518

JOHNSEN, S.J.; CLAUSEN, H.B.; DANSGAARD, W.; GUNDESTRUP, N.S.; HAMMER, C.U.; ANDERSEN, U.; ANDERSEN, K.K.; HVIDBERG, C.S.; DAHL-JENSEN, D.; STEFFENSEN, J.P.; SHOJI, H.; SVEINBJÖRNSDÓTTIR, Á.E.; WHITE, J.; JOUZEL, J.; FISHER, D. (1997): The $\delta^{18}\text{O}$ record along the Greenland Ice Core Project deep ice core and the problem of possible Eemian climatic instability, *Journal of Geophysical Research*, 102, pp. 26,397-26,410, doi: 10.1029/97JC00167

JONES, S.J.; GLEN, J.W. (1968): The Effect of Dissolved Impurities on the Mechanical Properties of Ice Crystals, *Philosophical Magazine*, 19, pp. 13-24, doi: 10.1080/14786436908217758

KAMNEV, A.A.; TARANTILIS, P.A.; ANTONYUK, L.P.; BESPALOVA, L.A.; POLISSIOU, M.G.; COLINA, M.; GARDINER, P.H.E.; IGNATIV, V.V. (2001): Fourier transform Raman spectroscopic characterization of cells of the plant-associated soil bacterium *Azospirillum brasilense* Sp7, *Journal of Molecular Structure*, 536-564, pp. 199-207

KAUFMANN, P.R.; FEDERER, U.; HUTTERLI, M.A.; BIGLER, M.; SCHÜPBACH, S.; RUTH, U.; SCHMITT, J.; STOCKER, T.F. (2008): An Improved Continuous Flow Analysis System for High-Resolution Field Measurements on Ice Cores, *Environmental Science & Technology*, 42, pp. 8044-8050, doi: 10.1021/es8007722

KEEGAN, K.M.; ALBERT, M.R., MCCONNELL, J.R.; BAKER, I. (2014): Climate change and forest fires synergetically drive widespread melt events of the Greenland Ice Sheet, *Proceedings of the National Academy of Sciences*, 111, pp. 7964-7967, doi: 10.1073/pnas.1405397111

KEENAN, D.J. (2003): Volcanic ash retrieved from GRIP ice core is not from Thera, *Geochemistry, Geophysics, Geosystems*, 4, 1097, doi: 10.1029/2003GC000608

KIPFSTUHL, S.; HAMANN, I.; LAMBRECHT, A.; FREITAG, J.; FARIA, S.H.; GRIGORIEV, D.; AZUMA, N. (2006): Microstructure mapping: a new method for imaging deformation-induced microstructural features of ice on the grain scale, *Journal of Glaciology*, 52, pp. 398-406, doi: 10.3189/172756506781828647

KIPFSTUHL, S.; FARIA, S.H.; AZUMA, N.; FREITAG, J.; HAMANN, I.; KAUFMANN, P.; MILLER, H.; WEILER, K.; WILHELMS, F. (2009): Evidence of dynamic recrystallization in polar firn, *Journal of Geophysical Research*, 114, pp. B05204, doi: 10.1029/2008JB005583

KJÆR, H.A.; SVENSSON, A.; VALLELONGA, P.; KETTNER, E.; SCHÜPBACH, S.; BIGLER, M.; STEFFENSEN, J.P., HANSSON, M.E. (2011): First continuous phosphate record from Greenland ice cores, *Climate of the Past Discussions*, 7, pp. 3959-3989, doi: 10.5194/cpd-7-3959-2011

KLEITZ, I. (2013): Physikalische Eigenschaften und Spurenstoffe im grönländischen Eis: Korrelationsberechnungen zwischen Korngröße bzw. Eigenwert und Spurenstoffkonzentrationen an ausgewählten Stücken des NEEM-Eiskerns, Alfred-Wegener-Institut für Polar- und Meeresforschung, Bremerhaven

KURAMOTO, T.; GOTO-AZUMA, K.; HIRABAYASHI, M. ET AL. (2011): Seasonal variations of snow chemistry at NEEM, Greenland, *Annals of Glaciology*, 52, pp. 193-200, doi: 10.3189/172756411797252365

LAI, P.; GHERMANDI, G.; CECCHI, R.; MAGGI, V.; RIONTINO, C.; HONG, S.; CANDELONE, J.P.; BOUTRON, C. (1997): Distribution of Ca, Fe, K, and S between soluble and insoluble material in the Greenland Ice Core Project ice core, *Journal of Geophysical Research*, 102, pp. 26,615-26,623, doi: 10.1029/96JC02660

LAVOUÉ, D.; LIOUSSE, C.; CACHIER, H. (2000): Modeling of carbonaceous particles emitted by boreal and temperate wildfires at northern latitudes, *Journal of Geophysical Research*, 105, pp. 26871-26,890, doi: 10.1029/2000JD900180

LEGRAND, M.R.; DELMAS, R.J. (1988): Soluble impurities in four Antarctic ice cores over the last 30 000 years, *Annals of Glaciology*, 10, pp. 116-120

LEGRAND, M.; DE ANGELIS, M.; STAFFELBACH, T.; NEFTEL, A.; STAUFFER, B. (1992): Large perturbations of ammonium and organic acids content in the Summit-Greenland ice core. Fingerprint from forest fires? *Geophysical Research Letters*, 19, pp. 473-475

LESINS, G.; CHYLEK, P.; LOHMANN, U. (2002): A study of internal and external mixing scenarios and its effect on aerosol optical properties and direct radiative forcing, *Journal of Geophysical Research*, 107, 4094, doi: 10.1029/2001JD000973

LEWIS, R.; SCHWARTZ, E. (2004): *Sea Salt Aerosol Production: Mechanisms, Methods, Measurements and Models – A Critical Review*, American Geophysical Union, Washington DC

LOWE, D.J. (2011): Tephrochronology and its application: a review, *Quaternary Geochronology*, 6, pp. 107-153, doi: 10.1016/j.quageo.2010.08.003

MADSEN, B.C.; MURPHY, R.J. (1981): Flow injection and photometric determination of sulfate in rainwater with methylthymol blue, *Analytical Chemistry*, 53, pp. 1924-1926, **doi:** 10.1021/ac00235a046

MASIELLO, C.A. (2004): New directions in black carbon organic geochemistry, *Marine Chemistry* 92, pp. 201-213, doi: 10.1016/j.marchem.2004.06.043

MCCONNELL, J.R.; EDWARDS, R.; KOK, G.L.; FLANNER, M.G.; ZENDER, C.S.; SALTZMANN, E.S.; ANTA, J.R.; PASTERIS, D.R.; CARTER, M.M.; KAHL, J.D.W. (2007): 20th-Century Industrial Black Carbon Emissions Altered Arctic Climate Forcing, *Science*, 317, pp. 1381-1384, doi: 10.1126/science.1144856

MING, J.; CACHIER, H.; XIAO, C.; QIN, D.; KANG, S.; HOU, S.; XU, J. (2008): Black carbon record based on a shallow Himalayan ice core and its climatic implications, *Atmospheric Chemistry and Physics*, 8, pp. 1343-1352

MONTAGNAT, M.; AZUMA, N.; DAHL-JENSEN, D.; EICHLER, J.; FUJITA, S.; GILLET-CHAULET, F.; KIPFSTUHL, S.; SAMYN, D.; SVENSSON, A.; WEIKUSAT, I. (2014): Fabric along the NEEM ice core, Greenland, and its comparison with GRIP and NGRIP ice cores, *The Cryosphere*, 8, 1129-1138

MÜLLER, G. & RAITH, M. (1993): *Methoden der Dünnschliffmikroskopie*, 4th ed., pp. 37-92; Clausthaler Tektonische Hefte Nr. 14

NEEM COMMUNITY MEMBERS (2013): Eemian interglacial reconstructed from a Greenland folded ice core, *Nature*, 493, pp. 489-494, doi: 10.1038/nature11789

NEFF, P.D. (2014): A review of the brittle zone in polar ice cores, *Annals of Glaciology*, 55, pp. 72-82, doi: 10.3189/2014AoG68A023

OHNO, H.; IGARASHI, M.; HONDOH, T. (2005): Salt inclusions in polar ice core: Location and chemical form of water-soluble impurities, *Earth and Planetary Science Letters*, 232, pp. 171-178, doi: 10.1016/j.epsl.2005.01.001

ÓLADÓTTIR, B.A.; SIGMARSSON, O.; LARSEN, G.; THONDARSON, T. (2008): Katla volcano, Iceland: magma composition, dynamics and eruption frequency as recorded by Holocene tephra layers, *Bulletin of Volcanology*, 70, pp. 475-493, doi: 10.1007/s00445-007-0150-5

OYABU, I.; IZUKA, Y.; UEMURA, R.; HIRABAYASHI, M.; MOTOYAMA, H.; SAKURAI, T.; SUZUKI, T.; HONDOH, T. (2014): Chemical composition of sulfate and chloride salts over the last termination reconstructed from the Dome Fuji ice core, inland Antarctica, *Journal of Geophysical Research: Atmospheres*, 119, pp. 14,045-14,058, doi: 10.1002/2014JD022030

OYABU, I.; IZUKA, Y.; FISCHER, H.; SCHÜPBACH, S.; GFELLER, G.; SVENSSON, A.; FUKUI, M.; STEFFENSEN, J.P.; HANSSON, M. (2015): Chemical composition of solid particles present in the Greenland NEEM ice core over the last 110,000 years, *Journal of Geophysical Research: Atmospheres*, 120, doi:10.1002/2015JD023290

PALAIS, J.M.; KIRCHNER, S.; DELMAS, R.J. (1990): Identification of some global volcanic horizons by major element analysis of fine ash in Antarctic ice, *Annals of Glaciology*, 14, pp.216-220

PARK, R.J.; JACOB, D.J.; PALMER, P.I.; CLARKE, A.D.; WEBER, R.J.; ZONDLO, M.A.; EISELE, F.L.; BANDY, A.R.; THORNTON, D.C.; SACHSE, G.W.; BOND, T.C. (2005): Export efficiency of black carbon aerosol, in continental outflow: Global implications, *Journal of Geophysical Research*, 110, D11205, doi: 10.1029/2004JD005432

PATERSON, W.S.B. (1991): Why ice age ice is sometimes “soft”, *Cold Regions Science and Technology*, 20, pp. 75-98, doi: 10.1016/0165-232X(91)90058-O

PATERSON, W. S. B. (1994): *The Physics of Glaciers*, 3rd ed., pp. 8-409, Elsevier

PEARCE, N.J.G.; WESTGATE, J.A.; PREECE, S.J.; EASTWOOD, W.J.; PERKINS, W.T. (2004): Identification of Aniakchak (Alaska) tephra in Greenland ice core challenges the 1645 BC date for Minoan eruption of Santorini, *Geochemistry, Geophysics, Geosystems*, 5, Q03005, doi: 10.1029/2003GC000672

PETERNELL, M.; KOHLMANN, F.; WILSON, C. J. L. ET AL. (2009): A new approach to crystallographic orientation for apatite fission track analysis: Effect of crystal morphology and implications by automation, *Chemical Geology*, 265, pp. 529-533 doi: 10.1016/j.chemgeo.2009.05.021

PETERNELL, M.; RUSSELL-HEAD, D. S.; WILSON, C. J. L. (2010): A technique for recording polycrystalline structure and orientation during in situ deformation cycles of rock analogues using an automated fabric analyser. *Journal of Microscopy*, 242, pp. 181-188, doi: 10.1111/j.1365-2818.2010.03456.x.

PETRENKO, V. F. & WHITWORTH, R. W. (1999): *Physics of Ice*, pp. 10-222; Oxford (Oxford University Press)

PYNE, S.J. (2001): The fires this time, and next, *Science* 294, pp. 1005-1006 doi: 10.1126/science.1064989

RASMUSSEN, S.O.; ANDERSEN, K.K.; JOHNSEN, S.J.; BIGLER, M.; MCCORMACK, T. (2005): Deconvolution-based resolution enhancement of chemical ice core records obtained by continuous flow analysis, *Journal of Geophysical Research*, 110, D17304, doi: 10.1029/2004JD005717

RASMUSSEN, S.O.; ANDERSEN, K.K.; SVENSSON, A.M.; STEFFENSEN, J.P.; VINTHER, B.M.; CLAUSEN, H.B.; SIGGAARD-ANDERSEN, M.L.; JOHNSEN, S.J.; LARSEN, L.B.; DAHL-JENSEN, D.; BIGLER, M.; RÖTHLISBERGER, R.; FISCHER, H.; GOTO-AZUMA, K.; HANSSON, M.E.; RUTH, U. (2006): A new Greenland ice core chronology for the last glacial termination, *Journal of Geophysical Research*, 111, D06102, doi: 10.1029/2005JD006079

RAMUSSEN, S.O.; ABBOTT, P.M.; BLUNIER, T.; BOURNE, A.J.; BROOK, E., BUCHARDT, S.L.; BUIZERT, C.; CHAPPELLAZ, J.; CLAUSEN, H.B.; COOK, E.; DAHL-JENSEN, D.; DAVIES, S.M.; GUILLEVIC, M.; KIPFSTUHL, S.; LAEPPEL, T.; SEIERSTAD, I.K.; SEVERINGHAUS, J.P., STEFFENSEN, J.P.; STOWASSER, C.; STOWASSER, C.; SVENSSON, A.; VALLELONGA, P.; VINTHER, B.M.; WILHELMS, F.; WINSTRUP, M. (2013): A first chronology for the North Greenland Eemian Ice Drilling (NEEM) ice core, *Climate of the Past*, 9, pp. 2713-2730, doi: 10.5194/cp-9-2713-2013

REMPEL, A.W.; WADDINGTON, E.D.; WETTLAUFER, J.S.; WORSTER MG (2001): Possible displacement, of the climate signal in ancient ice by premelting and anomalous diffusion, *Nature*, 411, pp. 568-571, doi: 10.1038/35079043

REMPEL, A.W.; WADDINGTON, E.D.; WETTLAUFER, J.S. (2002): Anomalous diffusion of multiple impurity species: predicted implications for the ice core climate records, *Journal of Geophysical Research*, 107, pp. 2330, doi: 10.1029/2002JB001857

RÖTHLISBERGER, R.; BIGLER, M.; HUTTERLI, M.; SOMMER, S.; STAUFFER, B.; JUNGHANS, H.G.; WAGENBACH, D. (2000): Technique for Continuous High-Resolution Analysis of Trace Substances in Firn and Ice Cores, *Environmental Science & Technology*, 34, pp. 338-342, doi: 10.1021/es9907055

RÖTHLISBERGER, R.; MULVANEY, R.; WOLFF, E.W.; HUTTERLI, M.A.; BIGLER, M.; DE ANGELIS, M.; HANSSON, M.E.; STEFFENSEN, J.P.; UDISTI, R. (2003): Limited dechlorination of sea-salt aerosols during the last glacial period: Evidence from the European Project for Ice Coring in Antarctica (EPICA) Dome C ice core, *Journal of Geophysical Research*, 108, 4526, doi: 10.1029/2003JD003604

RUTH, U. (2002): Concentration and Size Distribution of Microparticles in the NGRIP Ice Core (Central Greenland) during the Last Glacial Period, Institut für Umweltphysik, Universität Heidelberg

RUTH, U.; WAGENBACH, D.; STEFFENSEN, J. P. ET AL. (2003): Continuous record of microparticle concentration and size distribution in the central Greenland NGRIP ice core during the last glacial period, *Journal of Geophysical Research*, 108, pp. 4098 doi: 10.1029/2002JD002376

RUTH, U.; BIGLER, M.; RÖTHLISBERGER, R.; SIGGAARD-ANDERSEN, M.L.; KIPFSTUHL, S.; GOTO-AZUMA, K.; HANSSON, M.E.; JOHNSEN, S.J.; LU, H.; STEFFENSEN, J.P. (2007): Ice core evidence for a very tight link between North Atlantic and East Asian glacial climate, *Geophysical Research letters*, 34, L03706, doi: 10.1029/2006GL027876

SAKURAI, T.; OHNO, H.; HORIKAWA, S.; IZUKA, Y.; UCHIDA, T.; HIRAKAWA, K.; HONDOH, T. (2011): The chemical forms of water-soluble microparticles preserved in the Antarctic ice sheet during Termination I, *Journal of Glaciology*, 57, pp. 1027-1032, doi: 10.3189/002214311798843403

SCHÖNWIESE, C.-D. (2006): *Praktische Statistik für Meteorologen und Geowissenschaftler*, 4th ed., pp. 119-223, Stuttgart (Gebrüder Borntraeger Verlagsbuchhandlung)

SCHULSON, E. M. & DUVAL, P. (2009): *Creep and Fracture of Ice*, pp. 15-90, Cambridge (Cambridge University Press)

SCHWARZ, J.P.; GAO, R.S.; SPACKMAN, J.R.; WATTS, L.A.; THOMSON, D.S.; FAHEY, D.W.; RYERSON, T.B.; PEISCHL, J.; HOLLOWAY, J.S.; TRAINER, M.; FROST, G.J.; BAYNARD, T.; LACK, D.A.; DE GOUW, J.A.; WARNEKE, C.; DEL NEGRO, L.A. (2008a): Measuring of the mixing state, mass, and optical size of individual black carbon particles in urban and biomass burning emissions, *Geophysical Research Letters*, 35, L13810, doi: 10.1029/2008GL033968

SCHWARZ, J.P.; SPACKMAN, J.R.; FAHEY, D.W.; GAO, R.S.; LOHMAN, U.; STIER, P.; WATTS, L.A.; THOMSON, D.S.; LACK, D.A.; PFISTER, L.; MAHONEY, M.J.; BAUMGARDER, D.; WILSON, J.C.; REEVES, J.M. (2008b): Coatings and their enhancement of black carbon light absorption in the tropical atmosphere, *Journal of Geophysical Research*, 113, D03203, doi: 10.1029/2007JD009042

SEILER, W.; CRUTZEN, P.J. (1980): Estimates of gross and net flux of carbon between the biosphere and the atmosphere from biomass burning, *Climate Change*, 2, pp. 207-247, doi: 10.1007/BF00137988

SHOJI, H.; LANGWAY, C.C. (1983): Volume Relaxation of Air Inclusions in a Fresh Ice Core, *Journal of Physical Chemistry*, 87, pp. 4111-4114, doi: 10.1021/j100244a600

SIGG, A.; FUHRER, K.; ANKLIN, M.; STAFFELBACH, T.; ZURMÜHLE, D. (1994): A Continuous Analysis Technique for trace species in ice, *Environmental Science & Technology*, 28, pp. 204-209, doi: 10.1021/es00051a004

SMITH, E.; DENT, G. (2005): *Modern Raman Spectroscopy. A practical approach*, John Wiley & Sons, Ltd, Chichester, UK, doi: 10.1002/0470011831.ch1

STEFFENSEN, J. P. (1997): The size distribution of microparticles from selected segments of the Greenland Ice Core Project ice core representing different climate periods, *Journal of Geophysical Research*, 102, pp. 26,755-26,763, doi: 10.1029/97JC01490

STIER, P.; SEINFELD, J.H.; KINNE, S.; FEICHTER, J.; BOUCHER, O. (2006): Impact of nonabsorbing anthropogenic aerosols on clear-sky atmospheric absorption, *Journal of Geophysical Research*, 111, D18201, doi: 10.1029/2006JD007147

STOHL, A. (2006): Characteristics of atmospheric transport into the Arctic troposphere, *Journal of Geophysical Research*, 111, D11306, doi: 10.1029/2005JD006888

SURMA, J. (2011): *Die Orientierung der C-Achsen im NEEM-Eiskern (Grönland)*, Institut für Geologie und Mineralogie, Universität zu Köln

SVENSSON, A.; NIELSEN, S.W.; KIPFSTUHL, S.; JOHNSEN, S.J.; STEFFENSEN, J.P.; BIGLER, M.; RUTH, U.; RÖTHLISBERGER, R. (2005): Visual stratigraphy of the North Greenland Ice Core Project (NorthGRIP) ice core during the last glacial period, *Journal of Geophysical Research*, 110, D02108, doi: 10.1029/2004JD005134

TAMMEN, A. (2012): Mikrostruktur im Eis: Hochaufgelöste Korngrößen- und c-Achsenanalyse im NEEM-Kern (Grönland), Johannes Gutenberg-Universität Mainz

TSCHUMI, J.; STAUFFER, B. (2000): Reconstructing past atmospheric CO₂ concentrations based on ice-core analyses: open questions due to in situ production of CO₂ in the ice, *Journal of Glaciology*, 46, pp. 45-53, doi: 10.3189/172756500781833359

THORSTEINSSON, T.; KIPFSTUHL, J.; EICKEN, H. ET AL. (1995): Crystal size variations in Eemian age ice from the GRIP ice core, Central Greenland, *Earth and Planetary Science Letters*, 131, pp. 381-394, doi: 10.1016/0012-821X(95)00031-7

THORSTEINSSON, T. (1996): Textures and Fabrics in the GRIP ice core, in relation to climate history and ice deformation, *Berichte der Polarforschung*, 205, Alfred-Wegener-Institut für Polar- und Meeresforschung Bremerhaven

TURNER, C.S.M.; JONES, R.T. (2010): Does Agulhas Current amplify global temperatures during super-interglacial?, *Journal of Quaternary Science*, 25, pp. 839-843, doi: 10.1002/jqs.1423

VALLON, M.; PETIT, J.R.; FABRE, B. (1976): Study of an ice core to the bedrock in the accumulation zone of an alpine glacier, *Journal of Glaciology*, 17, pp. 13-28

WALLBRECHER, E. (1986): Tektonische und Gefügeanalytische Arbeitsweisen, Stuttgart (Ferdinand Enke Verlag)

WEERTMANN, J. (1964): Continuum distribution of dislocations on faults with finite friction, Bulletin of the Seismological Society of America, 54, pp. 1035-1058

WEIKUSAT, I.; KIPFSTUHL, J. (2010): Crystal c-axes (fabric) of ice core samples collected from the NEEM ice core, Alfred-Wegener-Institut, Helmholtz-Zentrum für Polar- und Meeresforschung, unpublished dataset #744004

WEIKUSAT, I.; DE WINTER, D. A. M.; PENNOCK, G. M ET AL. (2010): Cryogenic EBSD on ice: preserving a stable surface in a low pressure SEM, Journal of Microscopy, 242, pp. 295-310, doi: 10.1111/j.1365-2818.2010.03471.x

WEIKUSAT, I.; MIYAMOTO, A.; FARIA, S. H. ET AL. (2011): Subgrain boundaries in Antarctic ice quantified by X-ray Laue diffraction, Journal of Glaciology, 57, pp. 85-94, doi: 10.3189/002214311795306628

WEIKUSAT, C.; FREITAG, J.; KIPFSTUHL, S. (2012): Raman spectroscopy of gaseous inclusions in EDML ice core: first results – microbubbles, Journal of Glaciology, 58, pp. 761-766, doi: 10.3189/2012JoG11J222

WEIKUSAT, C.; KIPFSTUHL, S.; WEIKUSAT, I. (2015): Raman tomography of natural air hydrates, Journal of Glaciology, 61, pp. 923-930, doi: 10.3189/2015JoG15J009

WEINGARTNER, E.; BURTSCHER, H.; BALTENSBERGER, H. (1997): Hygroscopic properties of carbon and diesel soot particles, *Atmospheric Environment*, 31, pp. 2311-2327, doi: 10.1016/S1352-2310(97)00023-X

WEIßBACH, S. (2011): Saisonaler Eintrag von Spurenstoffen in das grönländische Eis und deren Auswirkung auf die Verdichtung von Firn: Fallstudie an einem ausgewählten Firnkernstück aus Nordgrönland, Technische Universität Bergakademie Freiberg

WILSON, C. J. L.; RUSSEL-HEAD, D. S.; KUNZE, K. ET AL. (2007): The analysis of quartz c-axis fabrics using a modified optical microscope, *Journal of Microscopy*, 227, 30-41 doi: 10.1111/j.1365-2818.2007.01784.x

WOLFF, E.W.; MULVANEY, R.; OATES, K. (1988): The location of impurities in Antarctic ice, *Annals of Glaciology*, 11, pp. 194-197

WOLFF, E. W.; FISCHER, H.; FUNDEL, F.; RUTH, U.; TWARLOH, B.; LITTOT, G. C.; MULVANEY, R.; RÖTHLISBERGER, R.; DE ANGELIS, M.; BOUTRON, C. F.; HANSSON, M.; JONSELL, U.; HUTTERLI, M. A.; LAMBERT, F.; KAUFMANN, P.; STAUFFER, B.; STOCKER, T. F.; STEFFENSEN, J. P.; BIGLER, M.; SIGGAARD-ANDERSEN, M. L.; UDISTI, R.; BECAGLI, S.; CASTELLANO, E.; SEVERI, M.; WAGENBACH, D.; BARBANTE, C.; GABRIELLI, P.; GASPARI, V. (2006): Southern Ocean sea-ice extent, productivity and iron flux over the past eight glacial cycles, *Nature*, 440, pp. 491–496, doi: 10.1038/nature04614M3

YUNG, Y.T.; LEE, T.; WANG, C.H.; SHIEH, Y.T. (1996): Dust: A diagnostic of the hydrologic circle during the last glacial maximum, *Science*, 271, pp. 962-962, doi: 10.1126/science.271.5251.962

ZENNARO, P.; KEHRWALD, N.; MCCONNELL, J.R.; SCHÜPBACH, S.; MASELLI, O.J.; MARLON, J.; VALLELONGA, P.; LEUENBERGER, D.; ZANGRANDO, R.; SPOLAOR, A.; BORROTTI, M.; BARBARO, E.; GAMBARO, A.; BARBANTE, C. (2014): Fire in ice: two millennia of boreal forest fire history from the Greenland NEEM ice core, *Climate of the Past*, 10, pp. 1905-1924, doi: 10.5194/cp-10-1905-2014

ZENNARO, P.; KEHRWALD, N.; MARLON, J.; RUDDIMAN, W.F.; BRÜCHER, T.; AGOSTINELLI, C.; DAHL-JENSEN, D.; ZANGRANDO, R.; GAMBARO, A.; BARBANTE, C. (2015): Europe on fire three thousand years ago: Arson or climate?, *Geophysical Research Letters*, 42, pp. 5023–5033, doi: 10.1002/2015GL064259

ZIELINSKI, G.A.; GERMANI, M.S. (1998): New Ice-Core Evidence Challenges the 1620's BC age for the Santorini (Minoan) Eruption, *Journal of Archaeological Science*, 25, pp. 279-289, doi: 10.1006/jasc.1997.0227

UNIVERSITY OF COPENHAGEN: NEEM (North Greenland Eemian Ice Drilling)

http://neem.dk/about_neem/ (20.10.2015)

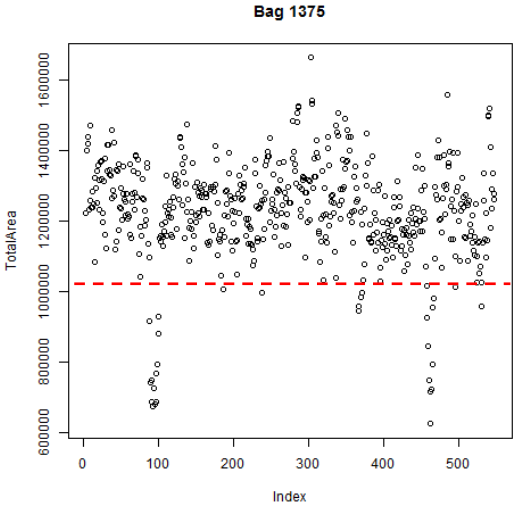
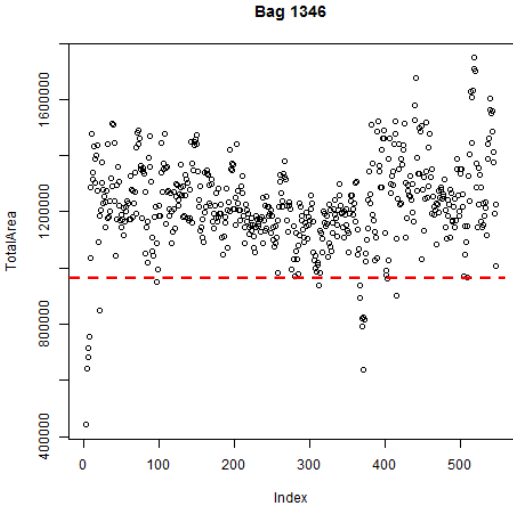
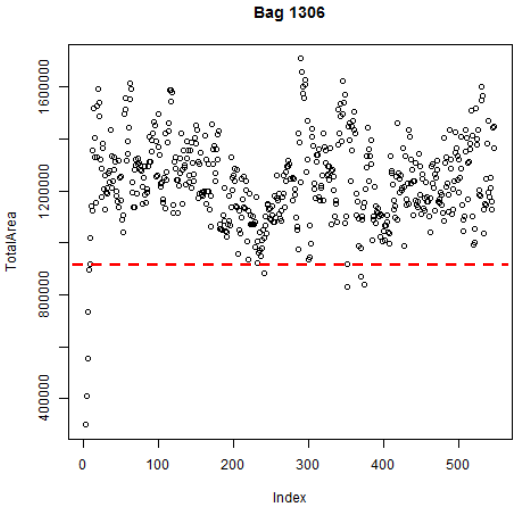
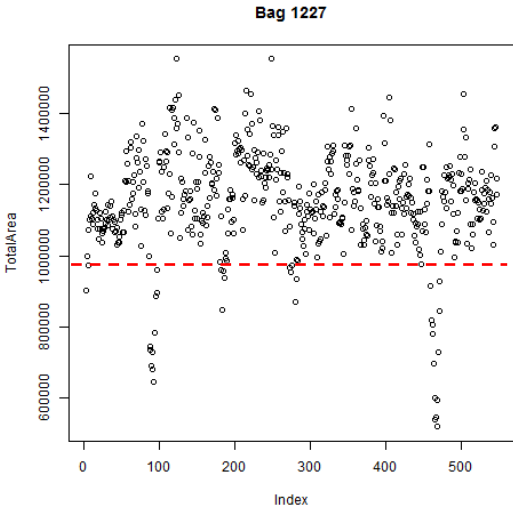
The RRUFF Project:

<http://rruff.info/>(21.10.2015)

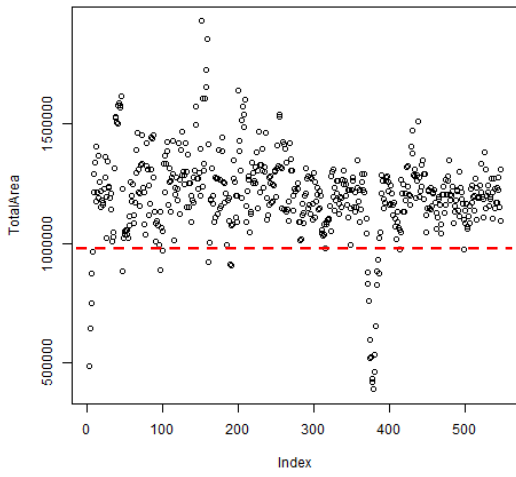
10. Appendix

10.1 Plot of the total area (all bags)

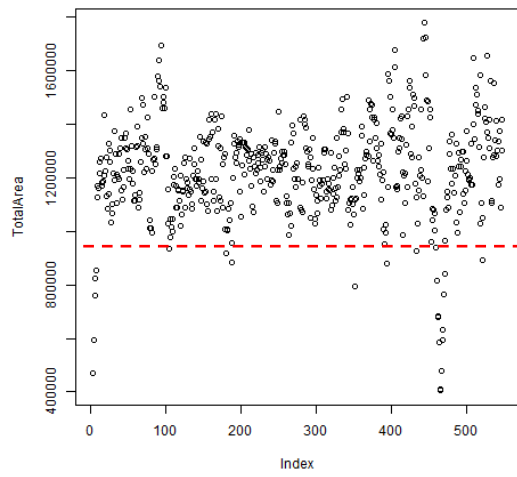
The graphs show the plot for the total area calculated from the mean grain size (pixel) and the number of grains. The values below the dashed red line had been removed.



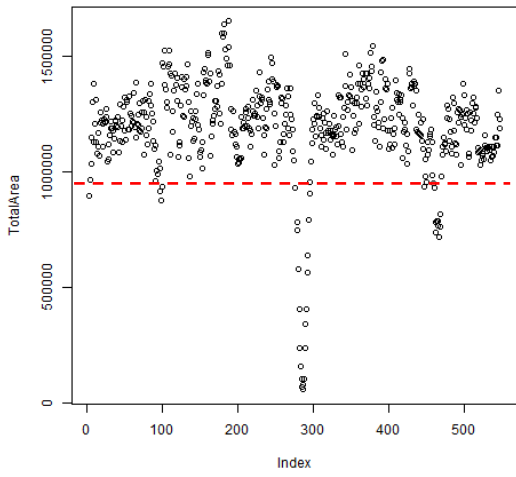
Bag 1426



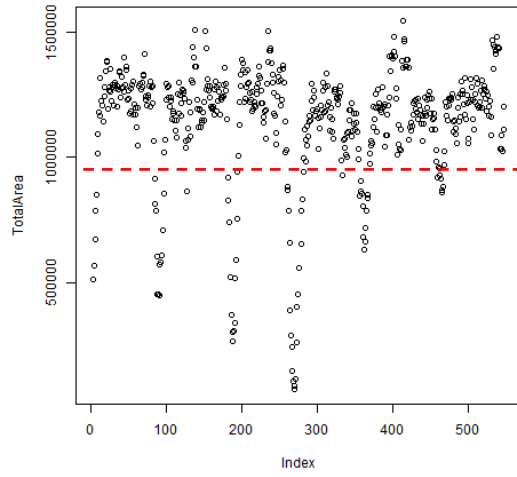
Bag 1496



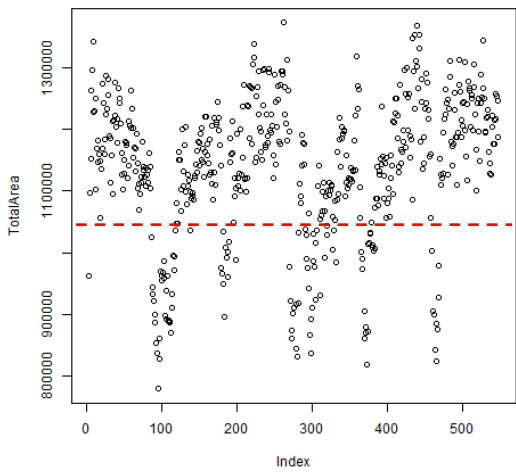
Bag 1815



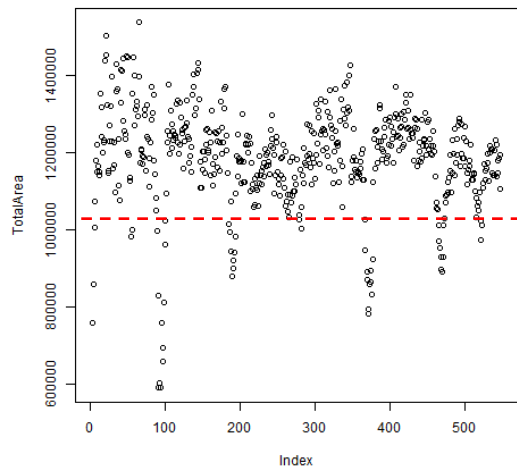
Bag 3356



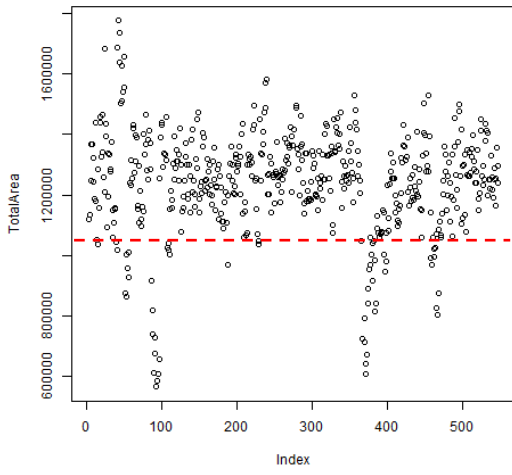
Bag 3876



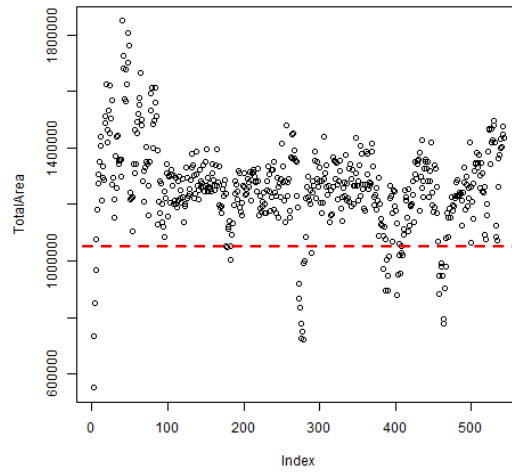
Bag 3906



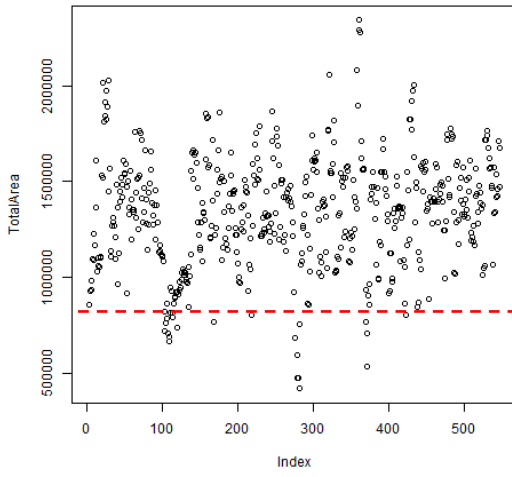
Bag 3956



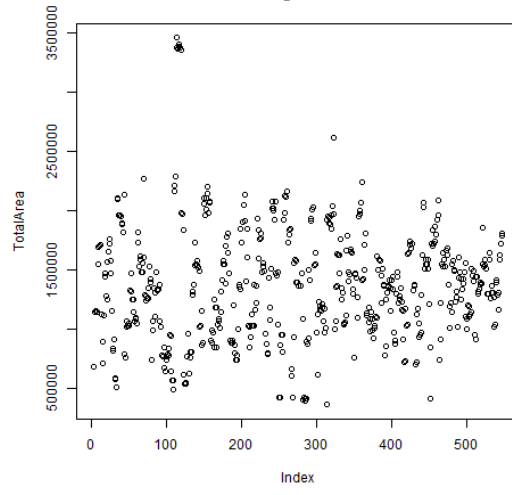
Bag 4006



Bag 4106



Bag 4196



10.2 Results of the Shapiro-Wilk-Test

The tables give the p-values for all compounds which should be $<0,05$ for not normally distributed data

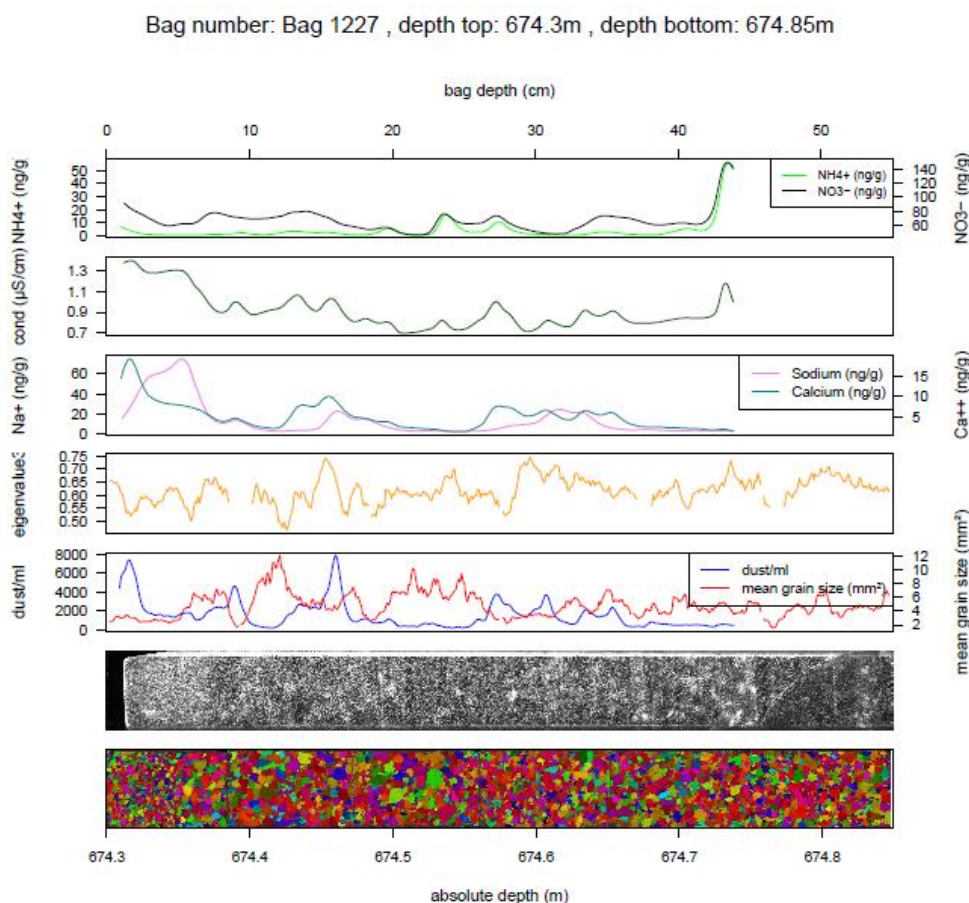
Bag nr	conductivity (p)	sodium (p)	calcium (p)	dust (p)
1227	4,42E-19	5,33E-28	2,13E-20	2,76E-23
1306	2,59E-06	1,01E-14	7,48E-18	1,40E-20
1346	7,37E-27	2,95E-19	9,60E-22	3,30E-22
1375	1,48E-06	3,32E-09	5,47E-12	2,95E-18
1426	7,35E-06	4,81E-20	2,41E-20	1,54E-25
1496	1,08E-11	5,96E-17	3,35E-13	1,70E-18
1815	7,11E-05	8,70E-12	6,57E-13	1,71E-14
3356	4,66E-06	1,45E-10	1,90E-07	2,02E-18
3876	2,23E-05	8,94E-11	6,18E-21	4,94E-29
3906	3,82E-16	5,15E-12	1,34E-11	7,69E-07
3956	8,54E-08	6,00E-10	1,18E-09	6,29E-09
4006	4,81E-13	1,50E-04	3,95E-02	4,40E-04
4106	5,79E-19	2,44E-09	3,01E-09	3,14E-14
4196	7,77E-08	2,27E-05	1,29E-03	4,66E-03

Bag nr	ammonium (p)	nitrate (p)	mean grain size (p)	eigenvalue 3 (p)
1227	1,72E-35	4,24E-25	2,99E-12	5,71E-02
1306	6,49E-21	5,77E-15	3,70E-16	7,47E-06
1346	1,92E-31	5,36E-07	1,09E-19	1,93E-07
1375	1,99E-25	3,04E-06	6,96E-07	3,21E-03
1426	1,34E-25	3,97E-21	2,50E-24	1,30E-05
1496	3,84E-31	1,37E-04	6,48E-12	4,69E-05
1815	6,47E-17	3,23E-05	5,11E-10	4,67E-05
3356	4,21E-18	5,69E-11	1,23E-04	5,24E-16
3876	4,60E-28	2,68E-12	6,18E-04	1,79E-12
3906	1,50E-26	5,56E-10	4,59E-08	3,25E-14
3956	2,75E-22	6,09E-20	4,26E-05	4,61E-10
4006	2,80E-23	1,58E-09	2,88E-04	4,67E-16
4106	4,57E-15	2,29E-09	1,30E-13	1,07E-20
4196	4,47E-25	2,20E-11	1,26E-16	1,22E-13

10.3 All bag plots

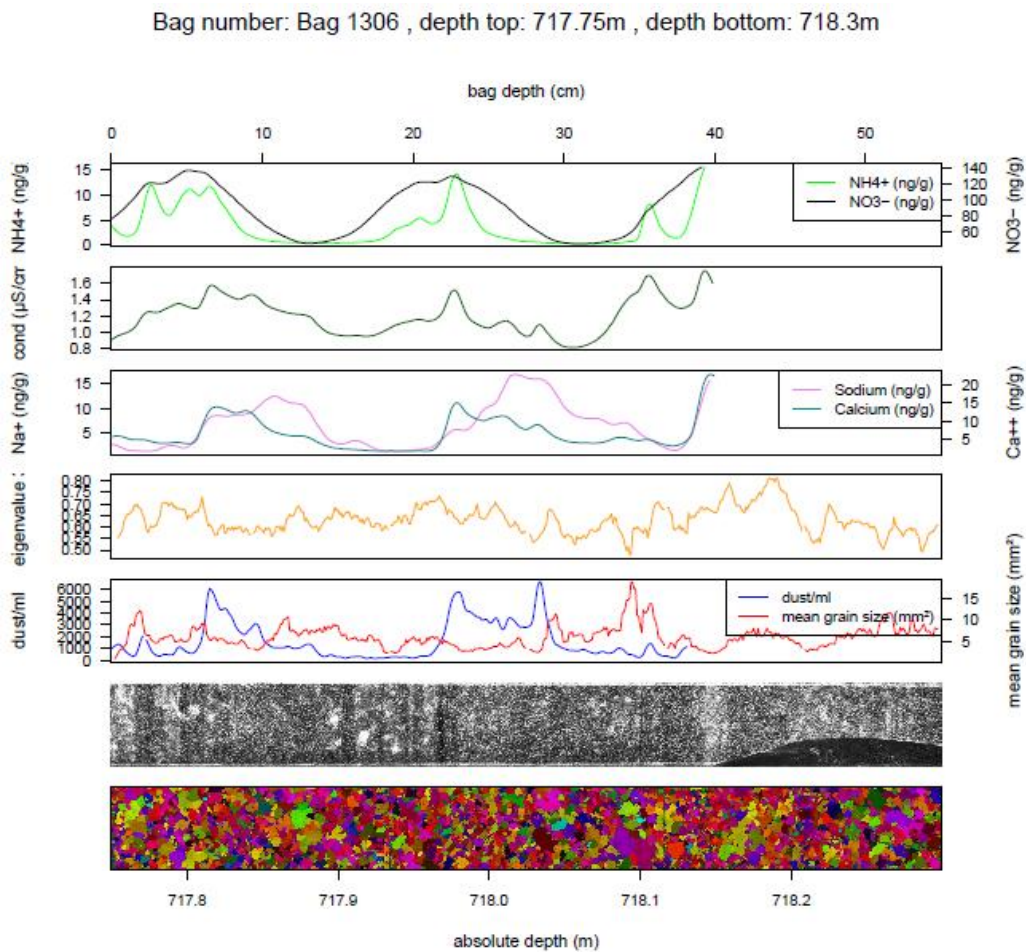
Bag 1227

This core section comes from a depth between 674,30 m and 674,85 m. After plotting the total area and removing the spikes, 94,43 % of the values for the mean grain size and 93,69 % of the values for the eigenvalue 3 could be used. The plot shows the maximum peaks for ammonium (56,30 ng/g) and nitrate (149,36 ng/g) at the end of the bag where a piece of the core broke off, indicating a possible contamination. The conductivity seems to correlate with ammonium and nitrate as well as with calcium. Sodium and calcium have their maxima of 75,01 ng/g and 19,10 ng/g, respectively, in the shallower part of the bag. The maximum peak of calcium is related to a peak in dust content. The linescan image confirms this connection, showing a bright part at the top which likely presents an area of high impurity concentration. Additionally, the mean grain size is smaller in that area (approx. from 674,30 m to 674,35 m) compared to the rest of the bag. The eigenvalue 3 fluctuates between 0,50 and 0,75, and, together with the trend image, showing that the c-axes do not appear to have a preferred orientation. Significant negative correlations could be found between the mean grain size and dust ($cc=-0,46$) as well as between the mean grain size and sodium ($cc=-0,53$). Calcium shows a weak negative correlation with the eigenvalue 3 of $-0,10$.



Bag 1306

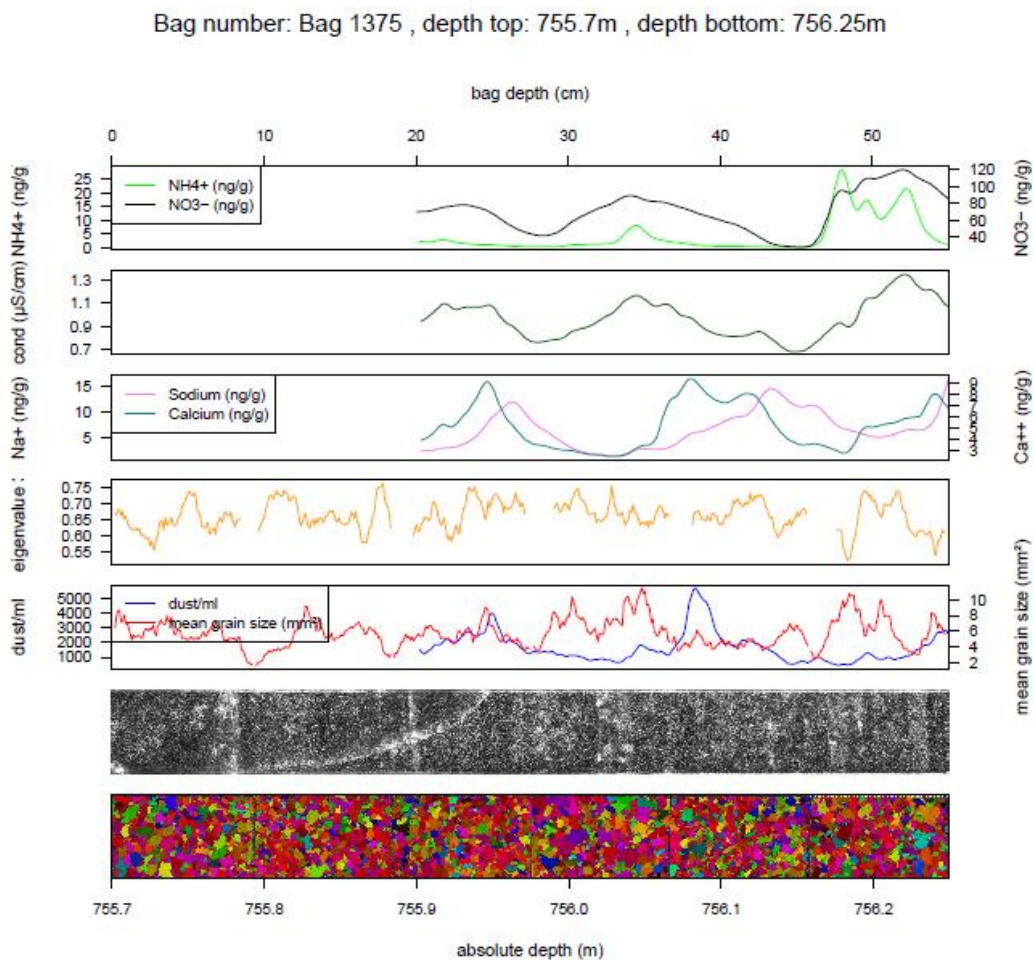
Bag 1306 comes from a depth between 717,75 m and 718,30 m. 98,70 % of the data for the mean grain size and 99,63 % of the data for the eigenvalue 3 could be included. Conductivity, ammonium and calcium show a major peak in the middle of the bag at around 717,98 m, which can be related to a peak in dust content. Sodium reaches a maximum value of 16,90 ng/g at 718,03 m. Nitrate shows very uniform variations which might be caused by disturbances during measuring. The eigenvalue fluctuated between 0,50 and 0,80 showing, together with the trend image, the same picture as in the previous bag. The highest value of the mean grain size can be found at approx. 718,10 m. In this bag the linescan image reveals several cloudy bands which could not be related to peaks in the dust content. Especially from 717.98 m to 718,04 m small grain sizes go together with relatively high dust content. Some weak correlations could be found between the eigenvalue 3 and dust ($cc=-0,16$), conductivity ($cc=0,11$), calcium ($cc=-0,13$) and nitrate ($cc=0,45$).



Bag 1375

For bag 1375 (755,7 m to 756,25 m depth) 93,32 % of the values for the mean grain size and 87,01 % of the values for the eigenvalue 3 could be included.

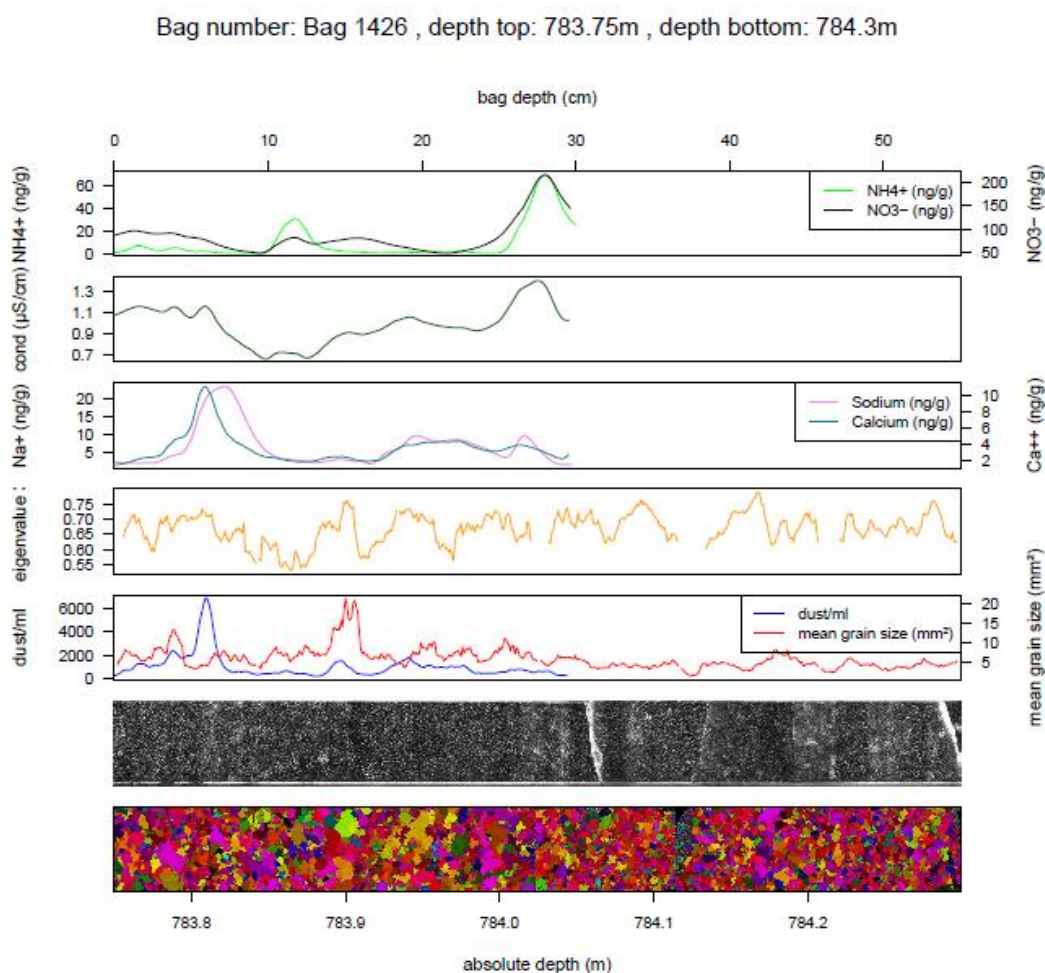
Bag 1375 shows a high content in ammonium and nitrate in the deeper part of the bag. Since ammonium shows several distinct peaks, the increase is not considered to originate from contamination. Ammonium reaches its maximum amount of 28,30 ng/g at around 756,18 m. Visually, sodium seems to show a negative correlation with nitrate. The variations in calcium go together with the major dust peaks (e.g. at around 755,98 m or 756,09 m). The dust peaks cannot be related to cloudy bands to be seen in the linescan image. The c-axes still remain without any preferred orientation. Negative correlations exist between the mean grain size and calcium with a correlation coefficient of -0,44 as well as between the eigenvalue 3 and ammonium ($cc=-0,21$) and the eigenvalue 3 and nitrate ($cc=-0,19$).



Bag 1426

This ice core section has been derived from a depth between 783,75 m to 784,30 m. For the mean grain size, 93,88 % of the data could be used; for the eigenvalue 3 92,95 % were included. CFA data could just be obtained down to a depth of 784,05 m due to a fracture of the core section. In this bag the content of nitrate and ammonium is very high, both showing a maximum around 822,75 m (nitrate 215,2 ng/g; ammonium 69,70 ng/g) and seem to be related to the conductivity graph. Calcium (11,10 ng/g) and sodium (23,40 ng/g) show peaks in the beginning of the bag at about 783.82 m that correlate with a maximum in the dust content. According to the trend image, the part that broke off shows smaller grain sizes and a slightly increased eigenvalue 3 compared to the rest of the bag. In the linescan image no cloudy bands could be identified.

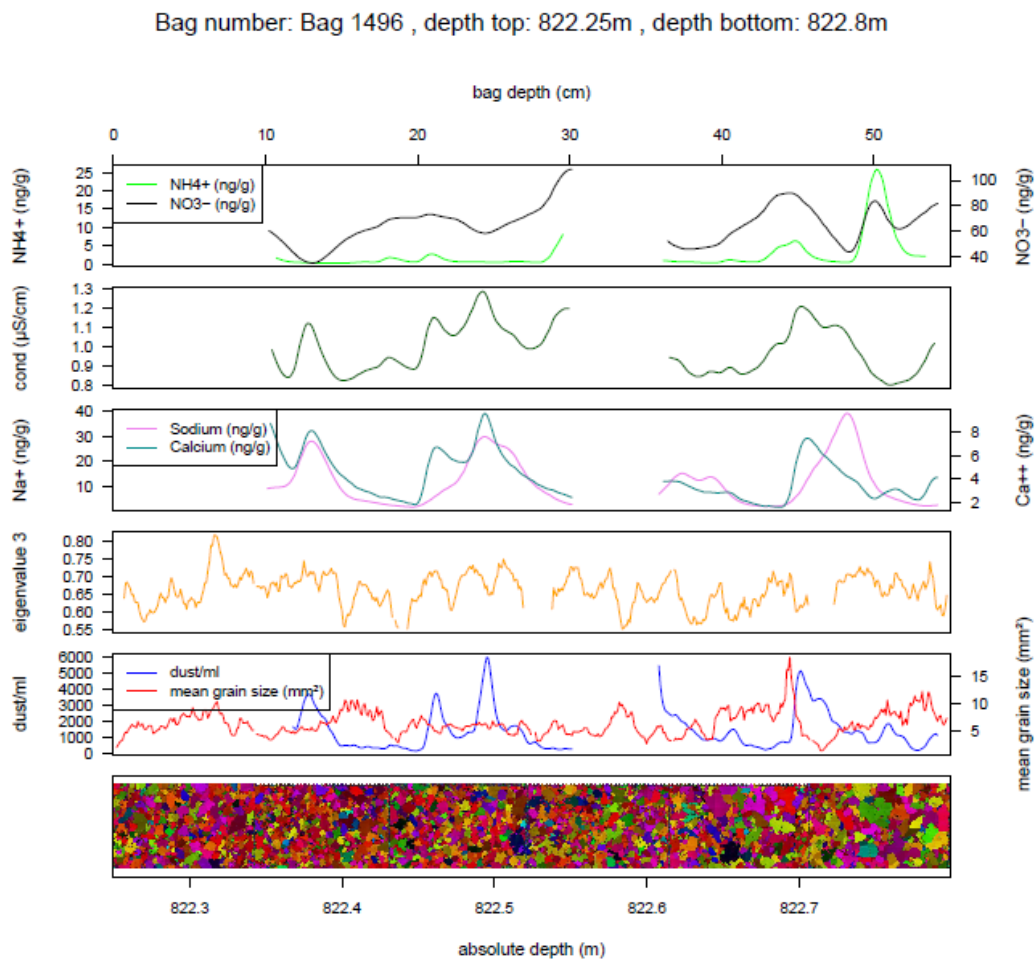
The mean grain size negatively correlates with the conductivity ($cc=-0,12$), with sodium ($cc=-0,21$) and with calcium ($-0,13$). It shows a positive correlation with ammonium ($cc=0,13$). Furthermore, the eigenvalue 3 positively correlates with the conductivity ($cc=0,49$) and with nitrate ($cc=0,21$).



Bag 1496

Bag 1496 comes from a depth between 822,25 m to 822,80 m. 95,73 % of the values calculated for the mean grain size and 92,39 % of the data for the eigenvalue 3 could be used. The core was broken twice so that no linescan image could be obtained. The conductivity in this bag is mostly related to the signal of the calcium ions which reaches a maximum of 9,5 ng/g at 822,50 m. Calcium also goes together with the dust signal. Maximum values of ammonium (25,70 ng/g) and nitrate (83,70 ng/g) can be seen at approximately 822,75 m. The x-axes still do not show a preferred orientation and thus the eigenvalue 3 varies between 0,55 and 0,80. Compared to the rest of the bag, some larger grains developed at the deeper end of the bag (also with no preferred orientation of the c-axes).

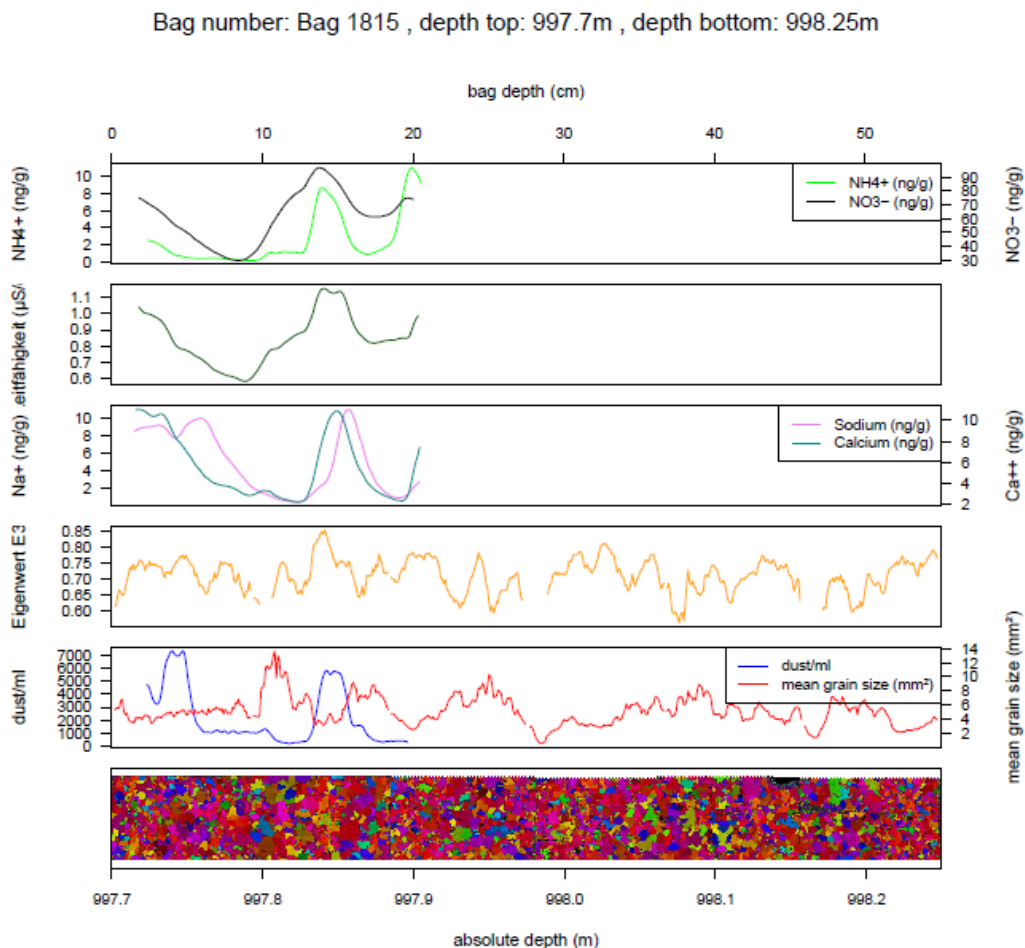
In this bag the mean grain size correlates with several compounds: negative correlations could be found with sodium ($cc=-0,47$) and calcium ($cc=-0,44$), positive correlations occur with ammonium ($cc=0,12$) and nitrate ($cc=0,16$).



Bag 1815

This core section comes from a depth between 997,70 m to 998,25 m. After plotting the total area, 92,58 % of the data for the mean grain size and 93,69 % of the data for the eigenvalue could be used.

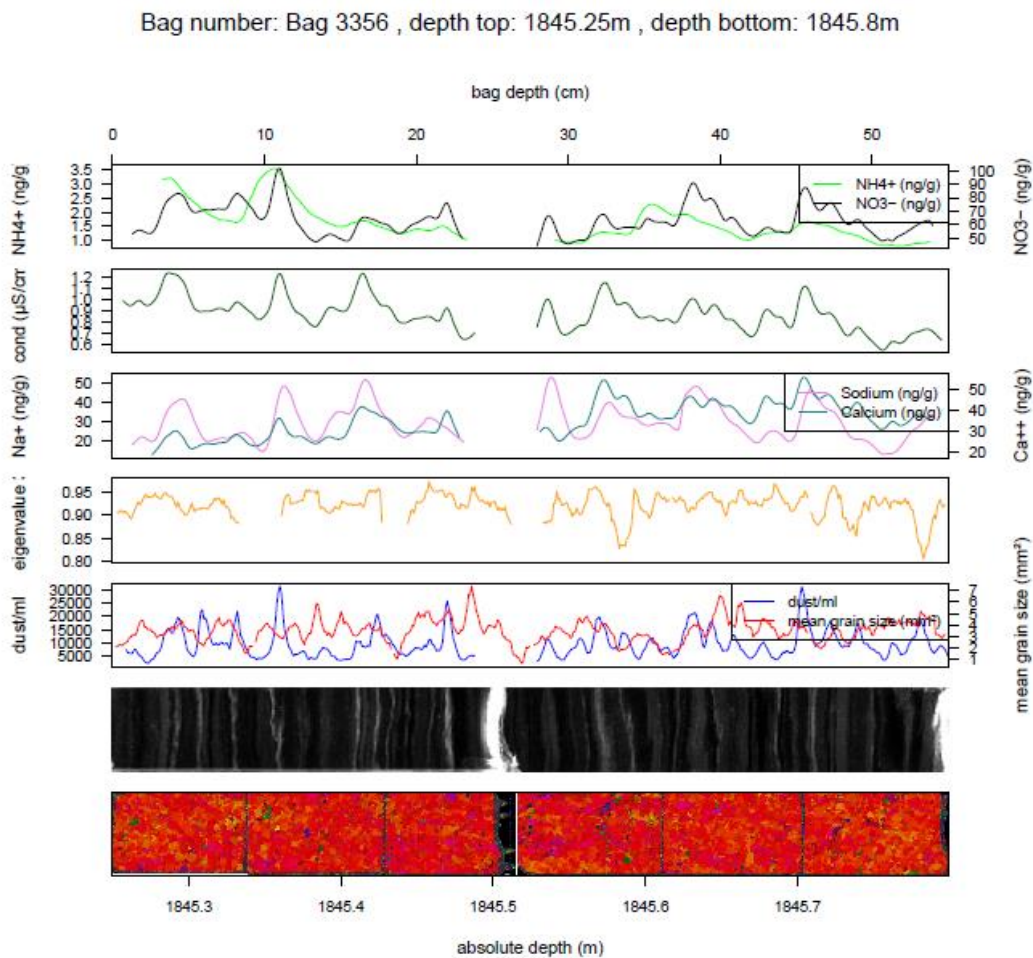
Since the largest part of the core broke off, no full interpretation can be given. Nevertheless, it can be determined that all ions and the conductivity peak together with the eigenvalue 3 and dust at around 997,84 m reaching their maximum values. The mean grain size shows strong fluctuations and for the remaining part of the bag cannot be related to the dust content. Compared to the previous bags, the data for the eigenvalue 3 show a slight increase which can also be seen in the colours of the grains in the trend image. The mean grain size shows weak negative correlations with sodium ($cc=-0,19$) and nitrate ($cc=-0,26$).



Bag 3356

This bag (845,25 m to 1845,80 m depth) shows one break on the middle of the core. After plotting the total area, 88,50 % of the data for the mean grain size and 87,20 % of the data for the eigenvalue 3 could be included in the plot.

As it can be seen in the plot, the conductivity positively correlates with the record of the major ions. The average amount of nitrate-ions is 63,59 ng/g, whereas the curve shows a strong maximum at 1845,36 m which is at 101,49 ng/g and a minimum at 1845,53 m (44,58 ng/g). The eigenvalue 3 varies between 0,84 and 0,96 showing that the c-axes of the crystals show a strong fabric. The cloudy bands seen in the linescan image can be related to peaks in the dust content of the sample (e.g. at 1845,48 m). The calculations reveal significant correlation coefficients between mean grain size and conductivity ($cc=-0,17$) and between mean grain size and sodium ($cc=-0,10$). The eigenvalue 3 correlates with dust ($cc=-0,10$) and ammonium ($cc=0,12$).

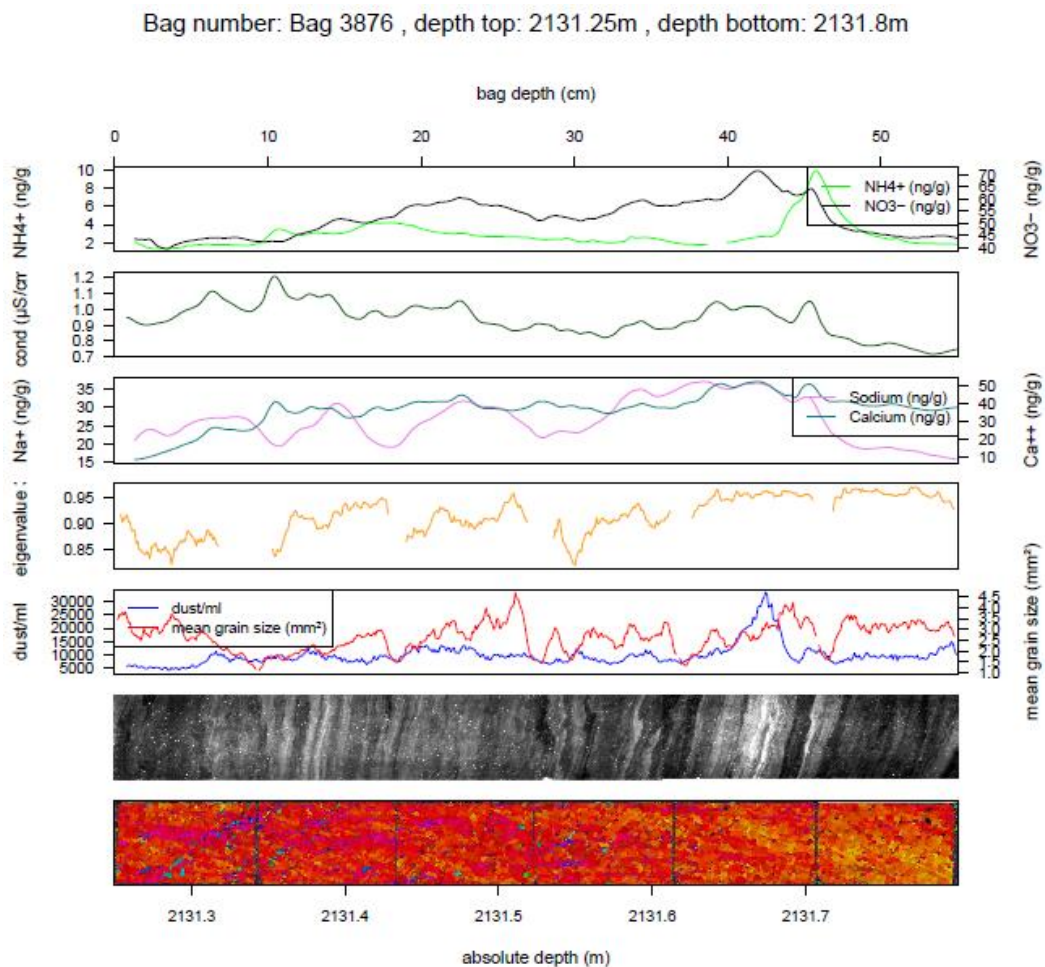


Bag 3876

For bag 3876 (2131,25 m to 2131,80 m depth), 90,17 % of the data for the mean grain size and 84,60 % of the data for the eigenvalue 3 could be included.

The maximum of the ammonium values (9,80 ng/g) can be related to peaks of calcium and sodium at about 2131,72 m, but are not coincident with the major peak in dust. This peak can be clearly seen in the linescan image, which shows several strong cloudy bands slightly tilted due to large scale deformation. The maximum of the dust content at 2131,68 m correlates with the nitrate concentration and with a stronger cloudy band whereas the peak in the other ion concentrations rather fit to a weaker cloudy band at 2131,72 m. In the first (upper) half of the bag, cloudy bands do not match the dust peaks. Compared to the previous bags, the mean grain sizes are smaller and the eigenvalue 3 is increased. Especially in the section 101 and 601 of the bag some fluctuations of the eigenvalue 3 can be seen, which are reflected in the trend image by some blue and yellow coloured bands.

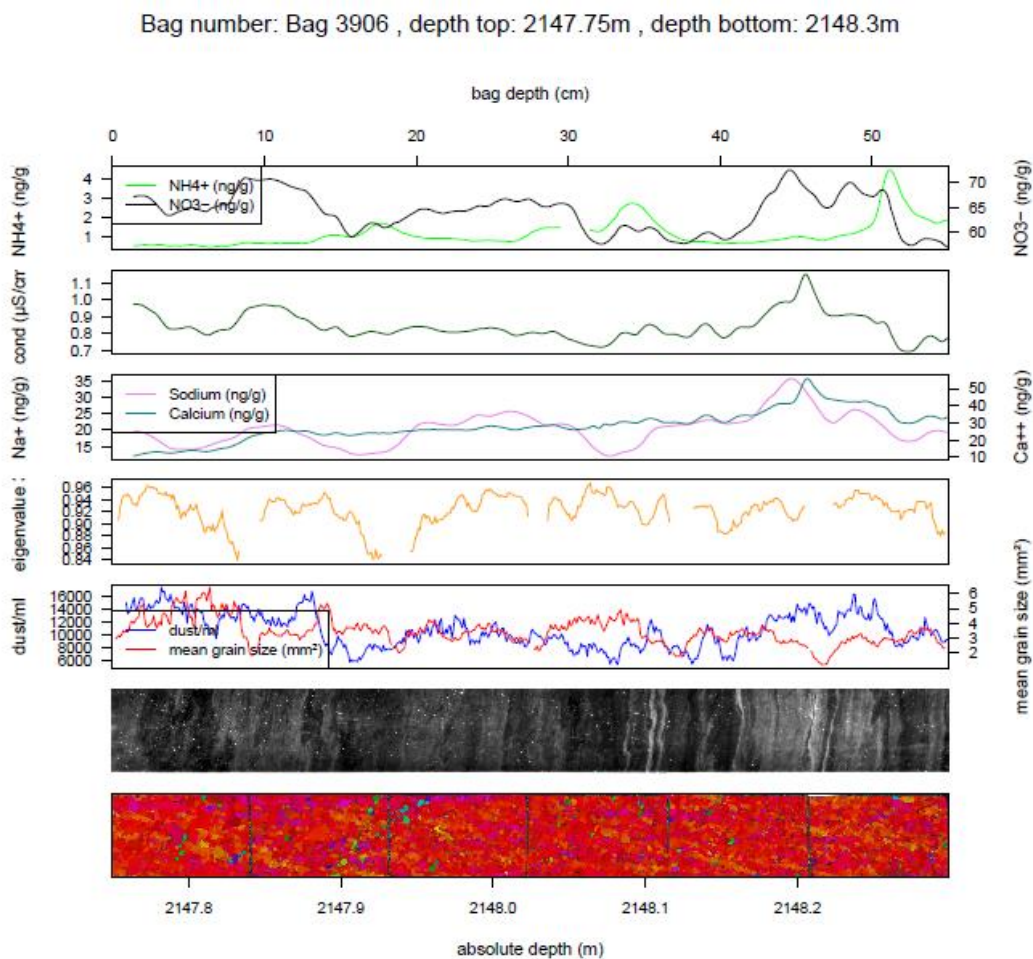
The mean grain size shows some weak correlations with dust ($cc=0,13$), with conductivity ($cc=-0,40$), with calcium ($cc=0,12$) and with nitrate ($cc=0,15$).



Bag 3906

Bag 3906 comes from a depth of 2147,75 m to 2148,30 m, and 92,95 % of the values for the mean grain size and 86,09 % of the data for the eigenvalue 3 could be used.

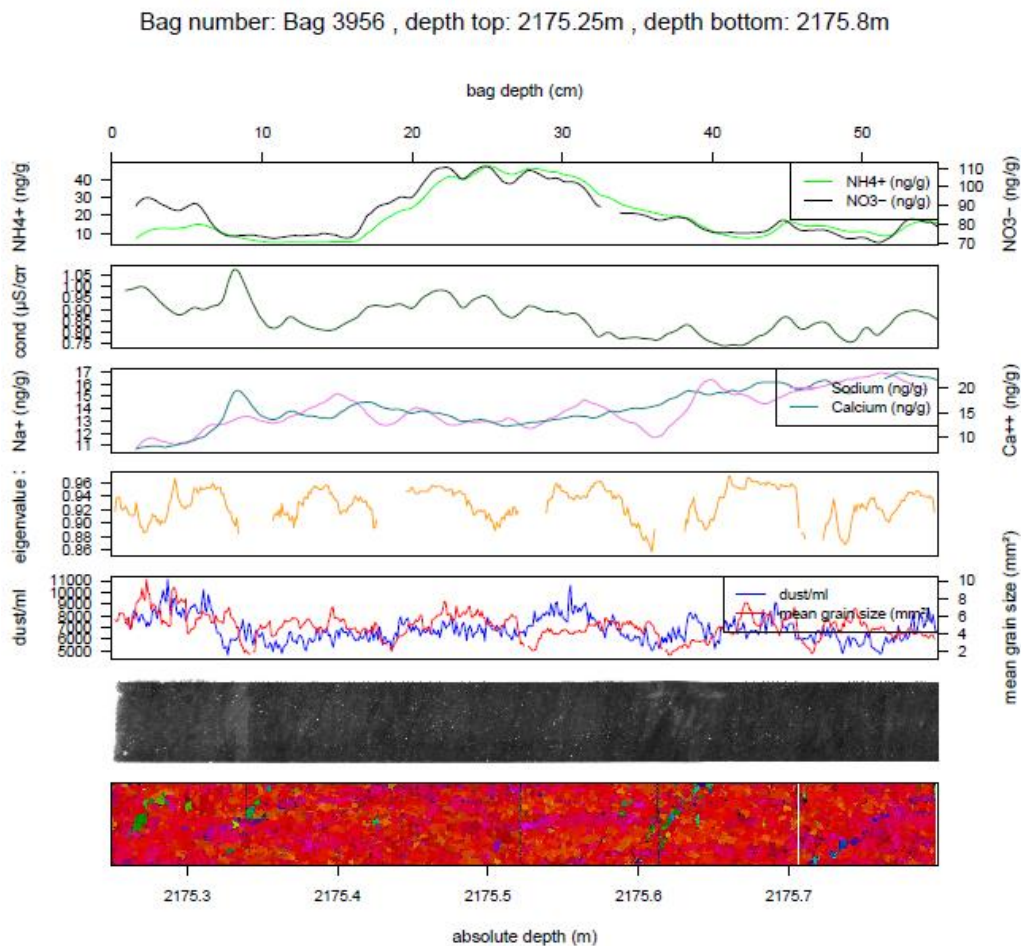
The major peaks of the ions can be found towards the deeper end of the bag, where they can be related to cloudy bands in the linescan image. Sodium shows stronger fluctuations than calcium and has its maximum peak of 35,80 ng/g at 2148,19 m. The c-axes are strongly orientated, although the eigenvalue 3 slightly decreases around 2147,93 m where a band of green coloured grains indicate a kink band in the trend image. The dust content measured with the CFA seems to be related to the cloudy bands at the deeper end of the bag at approx. 2148,21 m. No correlations could be found between dust and the mean grain size. Still, the mean grain size correlates with calcium ($cc=-0,57$) and with nitrate ($cc=-0,13$). The eigenvalue 3 correlates with the conductivity ($cc=0,14$) and as well weakly with calcium ($cc=0,09$).



Bag 3956

For this bag (2175,25 m to 2175,80 m depth). 93,50 % of the data for the mean grain size and 84,04 % of the data for the eigenvalue 3 were included.

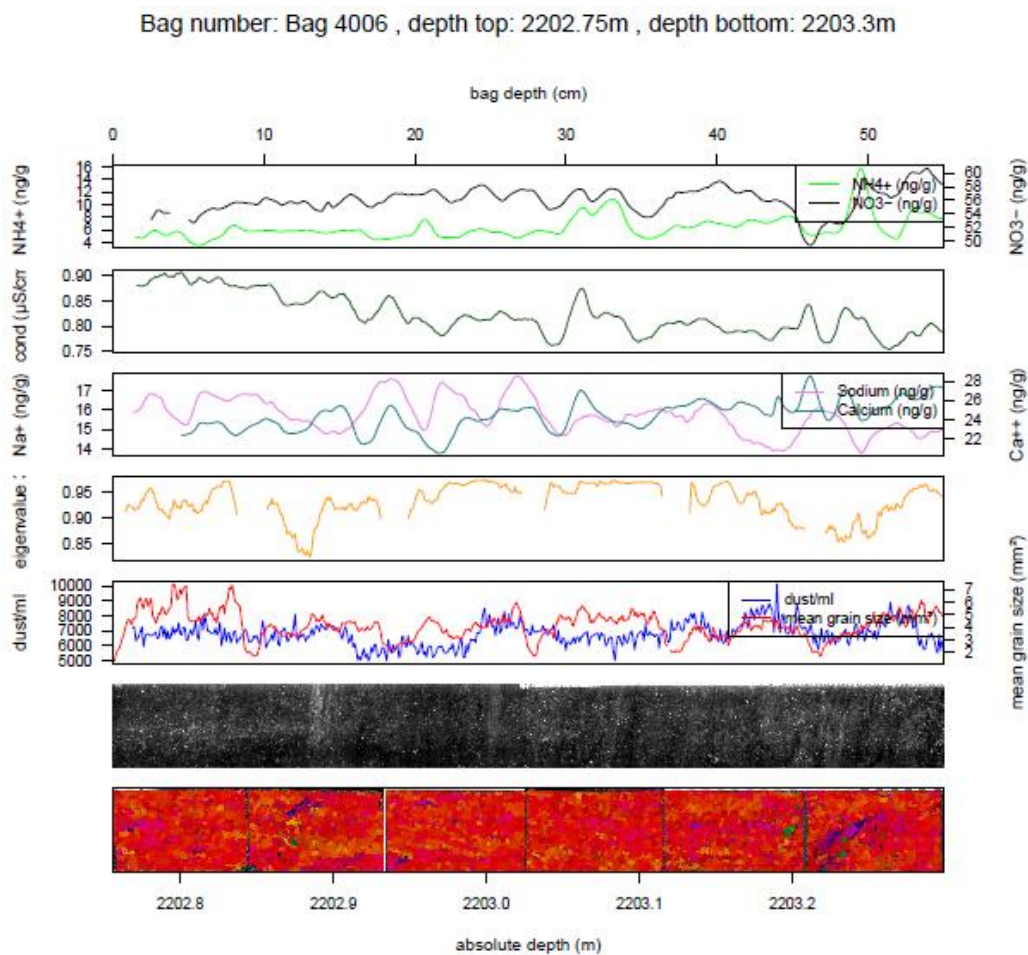
High amounts of nitrate and ammonium could be found especially in the middle of the bag, where both show maximum peaks at 2175,51 m (ammonium 45,90 ng/g and nitrate 108,80 ng/g). In this bag the calcium peaks do not go together with the dust peaks. The dust content is generally lower than in the previous bags and no cloudy bands could be identified in the linescan image. The grain sizes remain small and the eigenvalue 3 varies between 0,86 and 0,96, showing a strong orientation of the grains with exception of some green and blue coloured bands in the sections 501 and 601 at the end of the bag. Correlations could be found between the eigenvalue 3 and nitrate ($cc=0,12$). Furthermore the mean grain size correlates with dust ($cc=0,10$), with conductivity ($cc=0,16$) and with calcium ($cc=-0,37$).



Bag 4006

For bag 4006 (2202,75 m to 2203,30 m depth). 94,62 % of the values for the mean grain size and 84,23 % of the data for the eigenvalue 3 could be used.

In this bag nitrate and ammonium show their maxima at around 2203,24 m. The conductivity is slightly decreasing, while the values of the ions do not. It might also be due to some difficulties during measuring. Sodium strongly fluctuates and shows three major peaks of approximately 17 ng/g between 2202,92 m and 2203,05 m. Calcium reaches its maximum of 28,2 ng/g at 2203,21 m. Cloudy bands that can be related to the dust content could not be identified. The grain sizes still remain small, although some individual bigger grains with different orientations can be identified. The eigenvalue 3 varies between 0,85 and 0,95. The mean grain size shows weak correlations with dust ($cc=0,10$), with conductivity ($cc=0,15$) and with sodium ($cc=-0,15$). The eigenvalue 3 correlates with dust ($cc=-0,17$) and with conductivity ($cc=-0,13$).

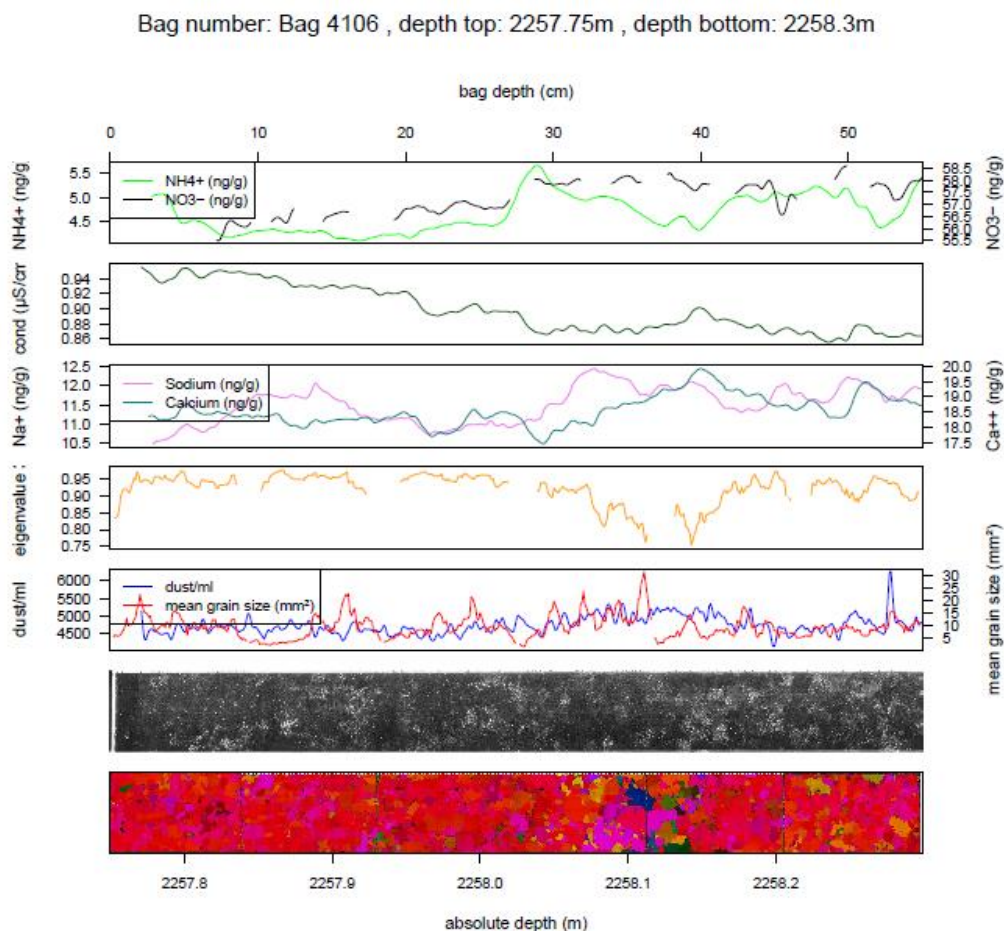


Bag 4106

For this core section (2257,75 m to 2258,30 m depth), 97,77 % of the data for the mean grain size and 84,42 % of the data for the eigenvalue 3 could be included.

Since the conductivity is decreasing again although the values of all other ions are increasing, there might be another factor influencing the curve. The values for the nitrate ions for this bag show too many gaps to be regarded as reliable data. Ammonium and calcium show a slight increase, whereas ammonium reaches a maximum peak of 5,60 ng/g at around 2258,04 m. Still, the ammonium content in this bag is relatively low. The dust content does not show major variations and thus cannot be related to any cloudy bands in the linescan image. According to the trend image some larger grains with different orientations of the c-axes developed around 2258,10 m which are also reflected by the decreasing curve of the eigenvalue 3 in this area. Generally, the mean grain size increased again compared to the previous bags. The dust peak at the deeper end of the bag at around 2258,28 m cannot be related to peaks of the amount of the major ions.

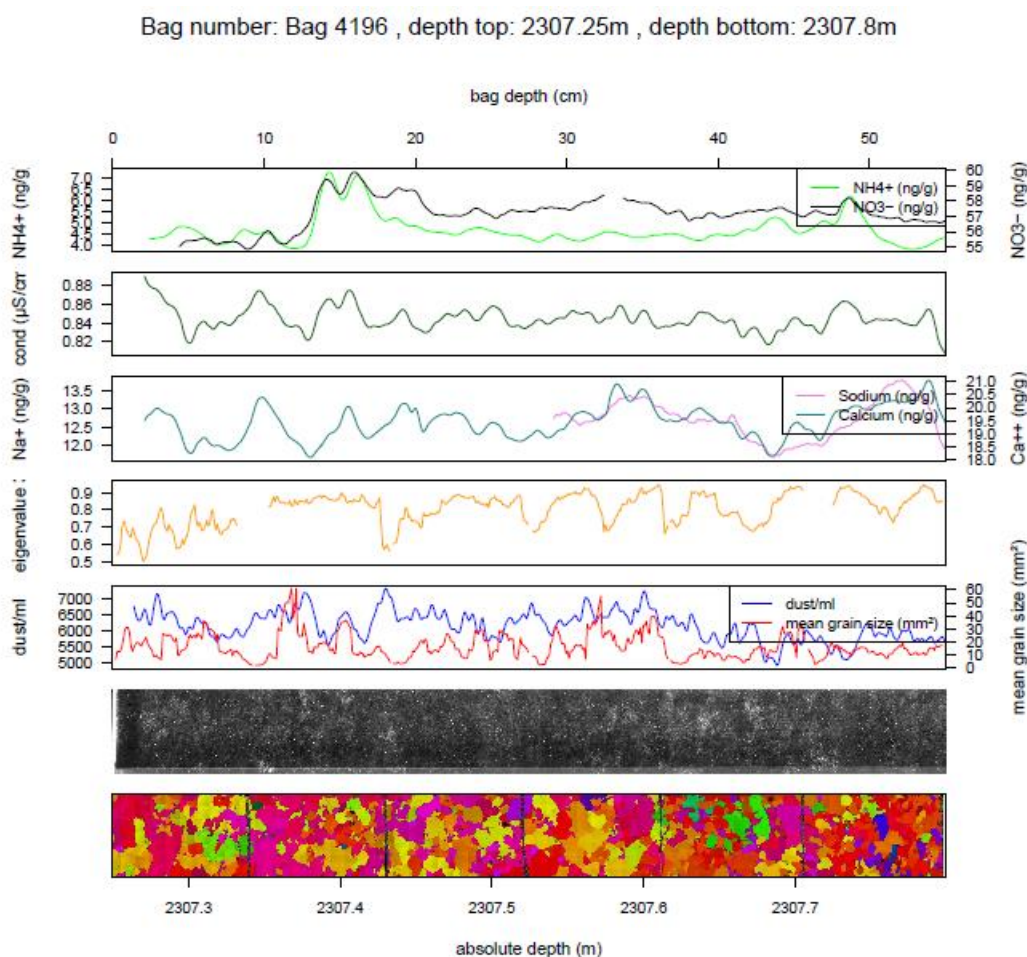
The mean grain size correlates with conductivity ($cc=-0,12$) and with ammonium ($cc=0,10$), whereas the eigenvalue 3 correlates with dust ($cc=-0,62$), with conductivity ($cc=0,43$), with calcium ($cc=-0,47$) and with nitrate ($cc=-0,67$).



Bag 4196

This bag comes from a depth between 2307,25 m to 2307,80 m. After plotting the total area, all data for the mean grain size and 92,95 % of the data for the eigenvalue 3 could be used.

The dust content in this bag still remains on a low level compared to the other bags while strong variations in the mean grain size and in the eigenvalue 3 occur. The eigenvalue fluctuates between 0,50 and 0,90 showing again a great variety of c-axis orientations. The mean grain size strongly increased in this depth of the NEEM ice core. The linescan image reveals no areas of high impurity concentrations. Nitrate and ammonium reach their maxima in the upper half of the core while calcium and sodium peak in the lower half. The only correlation to be found was between the eigenvalue 3 and nitrate with a correlation coefficient of 0,16.



10.4 Correlation coefficients for the chemical and physical parameters

The blue colour marks the statistically significant correlations (significance level 95%).

Every table gives the correlation coefficient (e.g. “dust”) and the corresponding p-value (e.g. “dust (p)”).

Bag 1306	dust	dust (p)	conductivity	conductivity (p)	sodium	sodium (p)
mean grain size	-0,269	1,26E+07	-0,044	0,380	-0,053	0,298
eigenvalue 3	-0,164	0,002	0,115	0,023	-0,307	0,000

Bag 1306	calcium	calcium (p)	ammonium	ammonium (p)	nitrate	nitrate (p)
mean grain size	-0,274	3,31E+06	-0,312	3,67E+04	-0,357	5,48E+00
eigenvalue 3	-0,133	0,008	0,351	1,27E+02	0,451	1,41E-06

Bag 1346	dust	dust (p)	conductivity	conductivity (p)	sodium	sodium (p)
mean grain size	0,137	0,006	0,103	0,036	0,212	1,18E+09
eigenvalue 3	-0,302	4,45E+05	-0,048	0,351	-0,195	1,34E-04

Bag 1346	calcium	calcium (p)	ammonium	ammonium (p)	nitrate	nitrate (p)
mean grain size	0,276	6,54E+04	-0,101	0,039	0,118	0,019
eigenvalue 3	-0,182	3,31E-04	-0,190	2,04E-04	0,096	0,071

Bag 1375	dust	dust (p)	conductivity	conductivity (p)	sodium	sodium (p)
mean grain size	-0,323	9,44E+04	0,280	1,54E+07	-0,447	3,66E-04
eigenvalue 3	0,078	0,180	-0,088	0,133	-0,042	0,479

Bag 1375	calcium	calcium (p)	ammonium	ammonium (p)	nitrate	nitrate (p)
mean grain size	-0,447	3,63E-04	0,343	7,26E+03	0,361	5,16E+02
eigenvalue 3	0,089	0,130	-0,213	2,30E-04	-0,195	0,001

Bag 1426	dust	dust (p)	conductivity	conductivity (p)	sodium	sodium (p)
mean grain size	0,064	0,281	-0,116	0,048	-0,206	4,05E-04
eigenvalue 3	0,454	1,84E-01	0,490	3,13E-04	0,090	0,132

Bag 1426	calcium	calcium (p)	ammonium	ammonium (p)	nitrate	nitrate (p)
mean grain size	-0,134	0,023	0,128	0,029	0,045	0,447
eigenvalue 3	0,349	2,32E+05	-0,100	0,095	0,209	4,44E-04

Bag 1496	dust	dust (p)	conductivity	conductivity (p)	sodium	sodium (p)
mean grain size	-0,394	6,04E-01	-0,406	6,36E-02	-0,472	1,65E-08
eigenvalue 3	0,279	3,07E+07	0,361	1,27E+03	0,381	2,40E+00

Bag 1496	calcium	calcium (p)	ammonium	ammonium (p)	nitrate	nitrate (p)
mean grain size	-0,435	9,45E-06	0,121	0,022	0,164	0,001
eigenvalue 3	0,381	4,69E+01	0,026	0,638	-0,053	0,329

Bag 1815	dust	dust (p)	conductivity	conductivity (p)	sodium	sodium (p)
mean grain size	-0,445	9,61E+03	-0,355	7,42E+07	-0,188	0,010
eigenvalue 3	0,440	3,39E+05	0,462	9,66E+03	0,130	0,082

Bag 1815	calcium	calcium (p)	ammonium	ammonium (p)	nitrate	nitrate (p)
mean grain size	-0,424	1,55E+05	-0,387	8,05E+06	-0,255	0,001
eigenvalue 3	0,481	8,59E+01	0,551	4,19E-01	0,395	9,21E+06

Bag 3356	dust	dust (p)	conductivity	conductivity (p)	sodium	sodium (p)
mean grain size	-0,025	0,577	-0,168	1,66E-04	-0,098	0,033
eigenvalue 3	-0,103	0,028	0,036	0,450	-0,001	0,985

Bag 3356	calcium	calcium (p)	ammonium	ammonium (p)	nitrate	nitrate (p)
mean grain size	-0,041	0,379	-0,290	4,53E+04	-0,056	0,222
eigenvalue 3	-0,007	0,895	0,122	0,014	0,044	0,358

Bag 3876	dust	dust (p)	conductivity	conductivity (p)	sodium	sodium (p)
mean grain size	0,126	0,003	-0,399	8,42E-08	-0,039	0,370
eigenvalue 3	0,353	1,26E+00	-0,293	1,94E+04	0,032	0,501

Bag 3876	calcium	calcium (p)	ammonium	ammonium (p)	nitrate	nitrate (p)
mean grain size	0,115	0,008	0,068	0,123	0,148	0,001
eigenvalue 3	0,478	5,53E-13	0,316	1,39E+03	0,320	5,63E+02

Bag 3906	dust	dust (p)	conductivity	conductivity (p)	sodium	sodium (p)
mean grain size	0,005	0,909	-0,186	1,78E+09	-0,530	1,30E-25
eigenvalue 3	0,232	4,66E+06	0,140	0,003	0,175	1,67E-04

Bag 3906	calcium	calcium (p)	ammonium	ammonium (p)	nitrate	nitrate (p)
mean grain size	-0,573	2,12E-33	-0,306	1,64E+02	-0,127	0,003
eigenvalue 3	0,093	0,047	0,031	0,515	0,219	2,11E+08

Bag 3956	dust	dust (p)	conductivity	conductivity (p)	sodium	sodium (p)
mean grain size	0,102	0,019	0,161	1,95E-04	-0,211	1,15E+08
eigenvalue 3	0,337	2,34E+01	-0,013	0,788	0,089	0,063

Bag 3956	calcium	calcium (p)	ammonium	ammonium (p)	nitrate	nitrate (p)
mean grain size	-0,375	2,49E-04	-0,080	0,066	0,075	0,088
eigenvalue 3	0,043	0,373	0,016	0,736	0,119	0,014

Bag 4006	dust	dust (p)	conductivity	conductivity (p)	sodium	sodium (p)
mean grain size	0,104	0,017	0,148	0,001	-0,148	0,001
eigenvalue 3	-0,174	2,10E-04	-0,135	0,004	0,268	7,79E+05

Bag 4006	calcium	calcium (p)	ammonium	ammonium (p)	nitrate	nitrate (p)
mean grain size	-0,055	0,225	0,037	0,402	0,075	0,093
eigenvalue 3	-0,037	0,448	0,008	0,869	0,317	2,09E+02

Bag 4106	dust	dust (p)	conductivity	conductivity (p)	sodium	sodium (p)
mean grain size	0,059	0,177	-0,123	0,005	-0,011	0,803
eigenvalue 3	-0,620	2,83E-34	0,431	2,03E-07	-0,521	1,64E-17

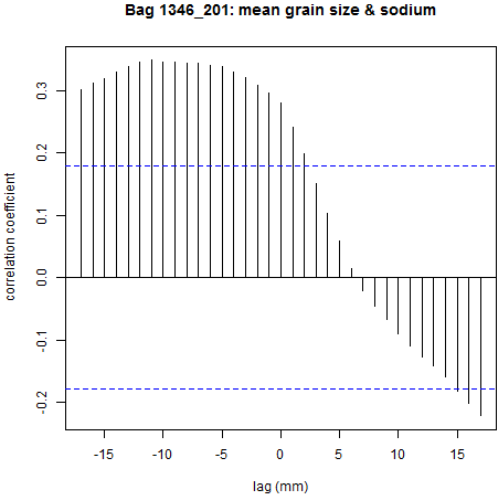
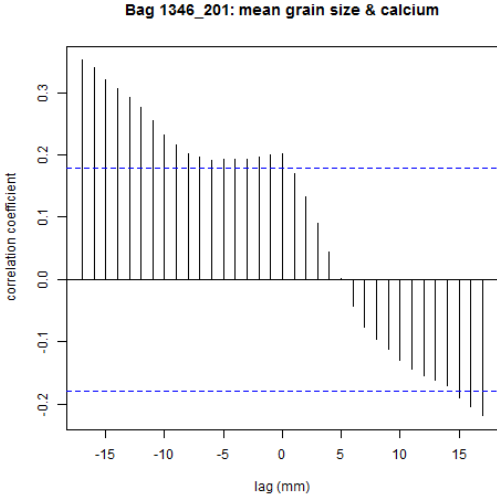
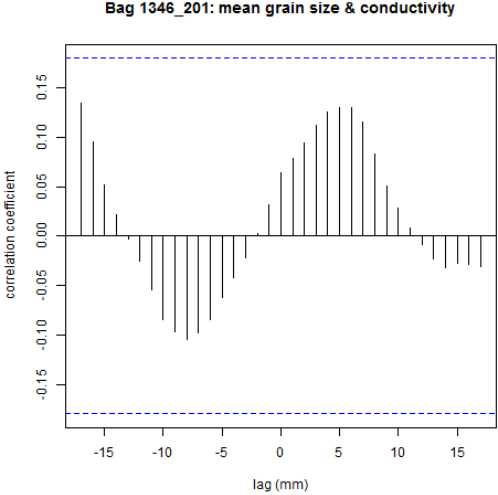
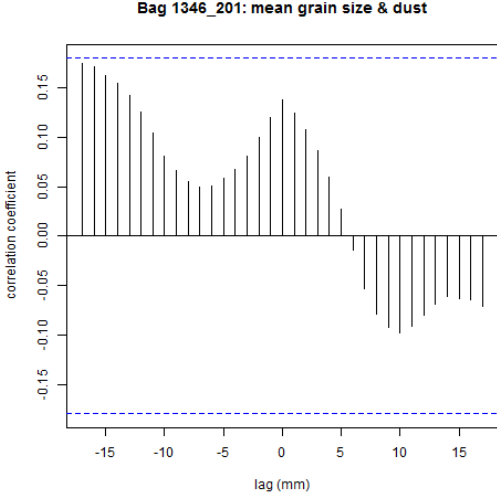
Bag 4106	calcium	calcium (p)	ammonium	ammonium (p)	nitrate	nitrate (p)
mean grain size	-0,020	0,658	0,105	0,018	0,237	3,10E+09
eigenvalue 3	-0,473	1,23E-11	-0,406	1,10E-04	-0,666	7,54E-26

Bag 4196	dust	dust (p)	conductivity	conductivity (p)	sodium	sodium (p)
mean grain size	0,183	2,33E+09	-0,039	0,380	0,074	0,239
eigenvalue 3	-0,209	3,16E+08	0,308	4,32E+02	-0,053	0,413

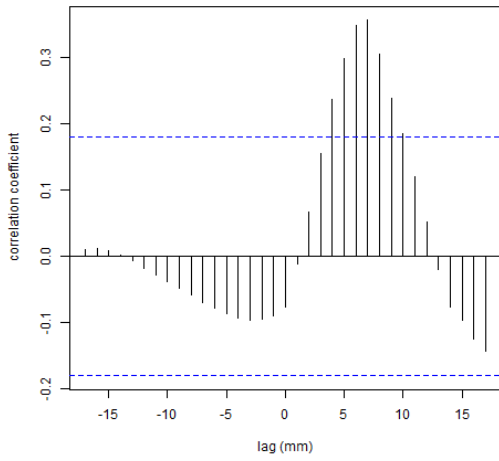
Bag 4196	calcium	calcium (p)	ammonium	ammonium (p)	nitrate	nitrate (p)
mean grain size	-0,078	0,074	-0,072	0,102	0,078	0,086
eigenvalue 3	0,289	8,99E+03	-0,024	0,604	0,160	0,001

10.5 Cross correlations for sections 201 and 501 of bag 1346

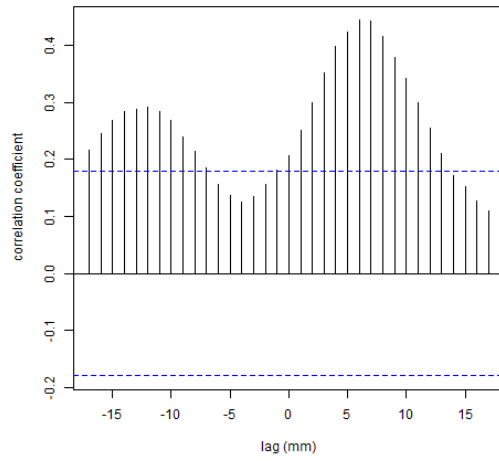
Values above the dashed blue line are statistically significant.



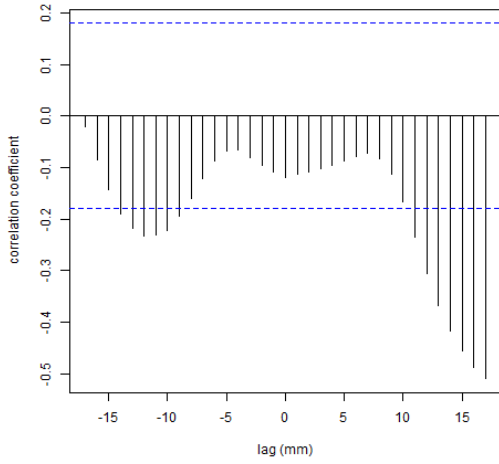
Bag 1346_201: mean grain size & ammonium



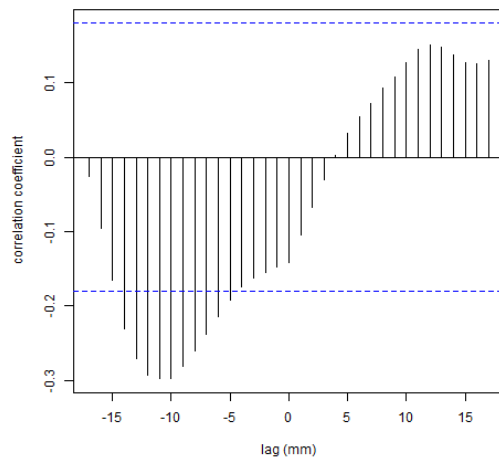
Bag 1346_201: mean grain size & nitrate



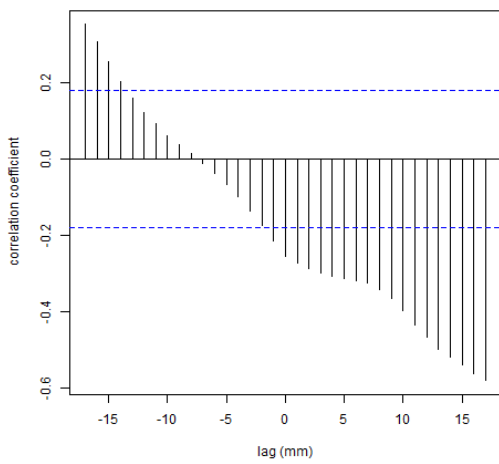
Bag 1346_201: eigenvalue 3 & dust



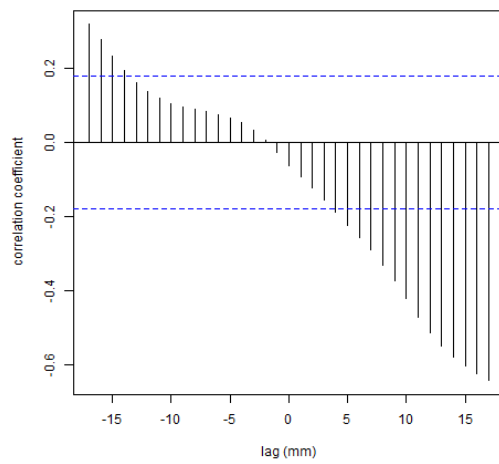
Bag 1346_201: eigenvalue 3 & conductivity



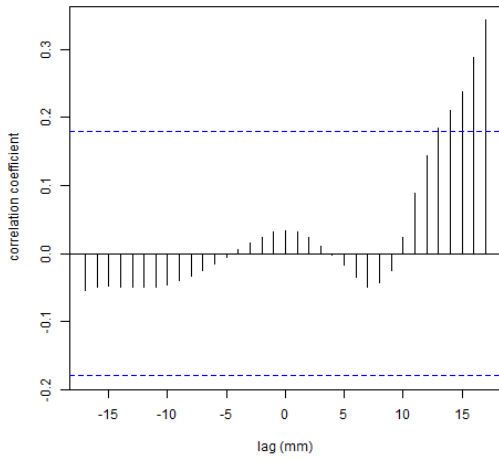
Bag 1346_201: eigenvalue 3 & calcium



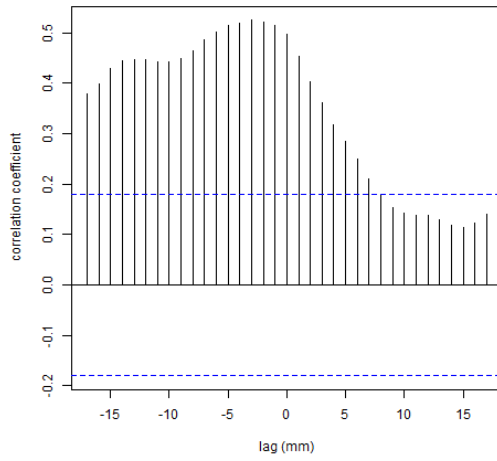
Bag 1346_201: eigenvalue 3 & sodium



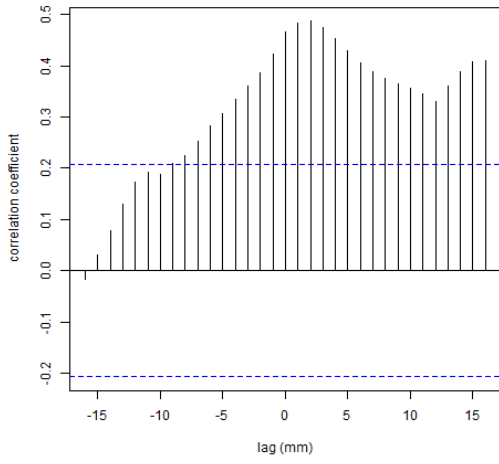
Bag 1346_201: eigenvalue 3 & ammonium



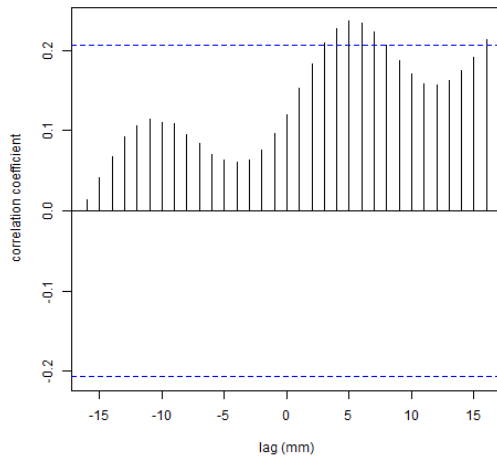
Bag 1346_201: eigenvalue 3 & nitrate



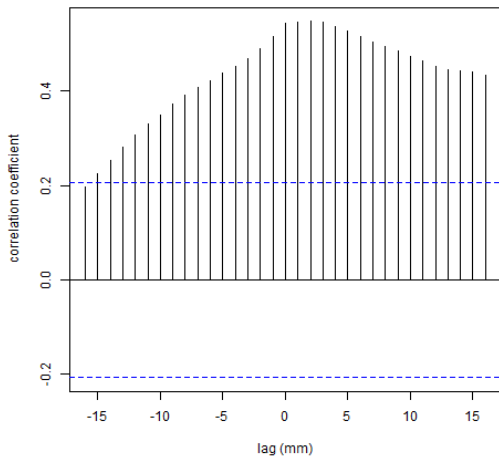
Bag 1346_501: mean grain size & dust



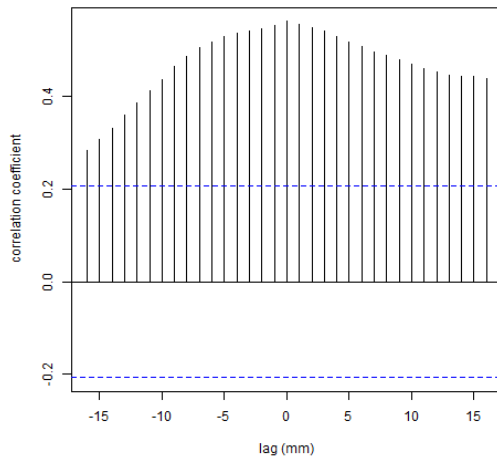
Bag 1346_501: mean grain size & conductivity



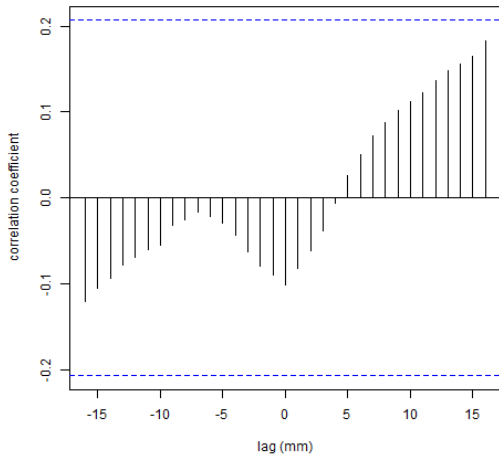
Bag 1346_501: mean grain size & calcium



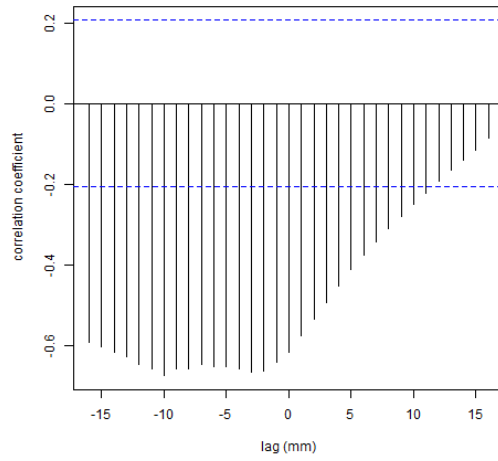
Bag 1346_501: mean grain size & sodium



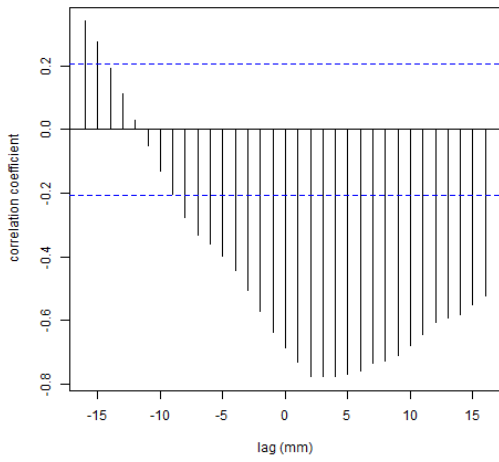
Bag 1346_501: mean grain size & ammonium



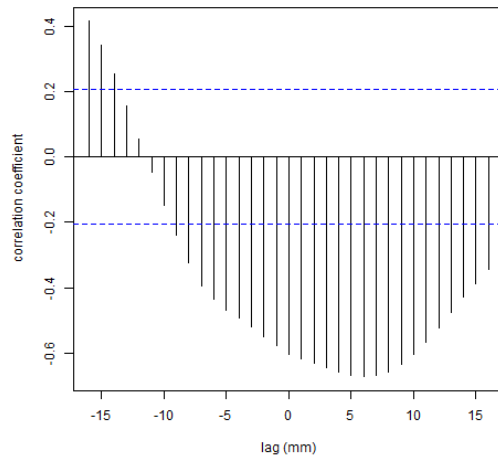
Bag 1346_501: mean grain size & nitrate



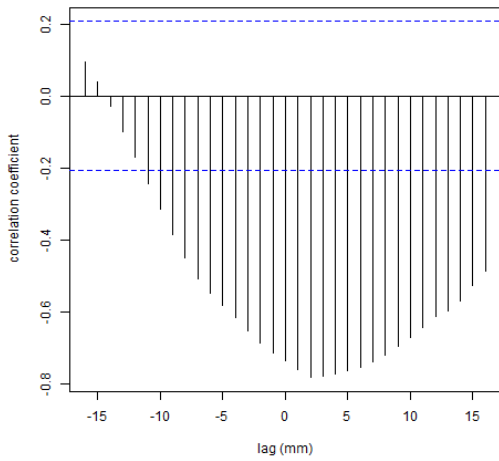
Bag 1346_501: eigenvalue 3 & dust



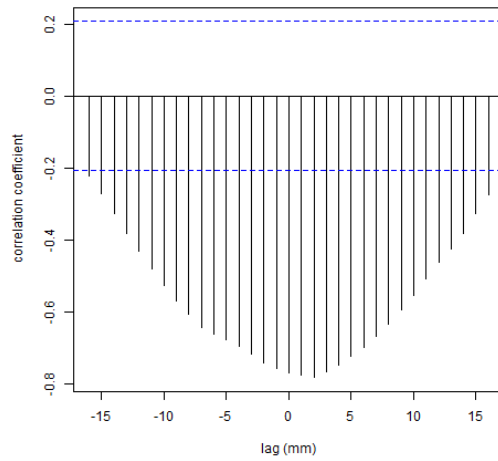
Bag 1346_501: eigenvalue 3 & conductivity

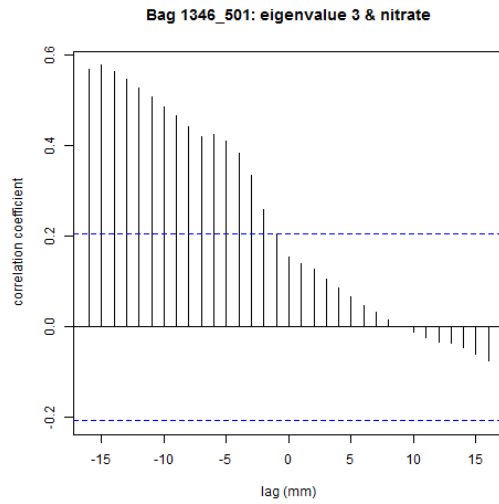
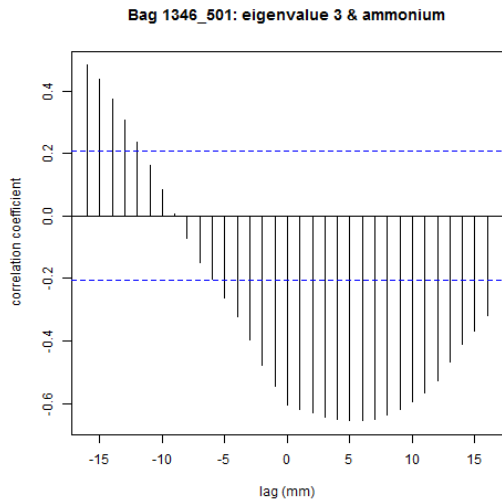


Bag 1346_501: eigenvalue 3 & calcium



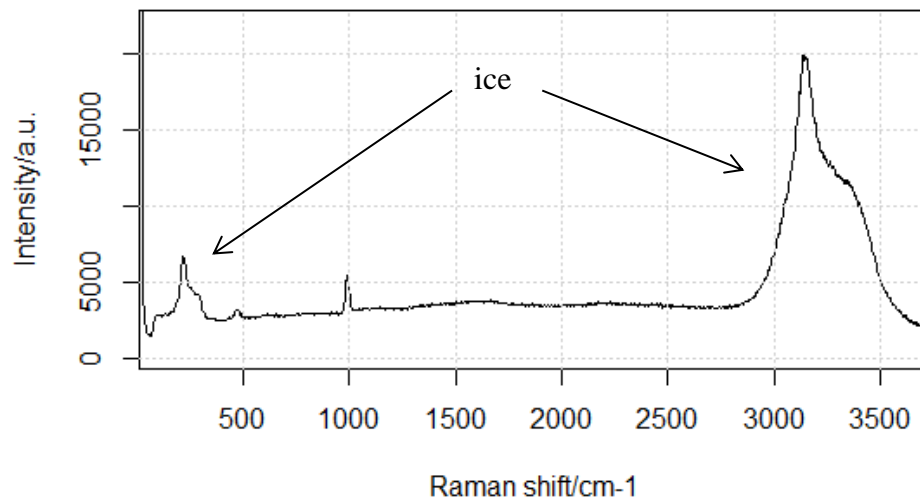
Bag 1346_501: eigenvalue 3 & sodium



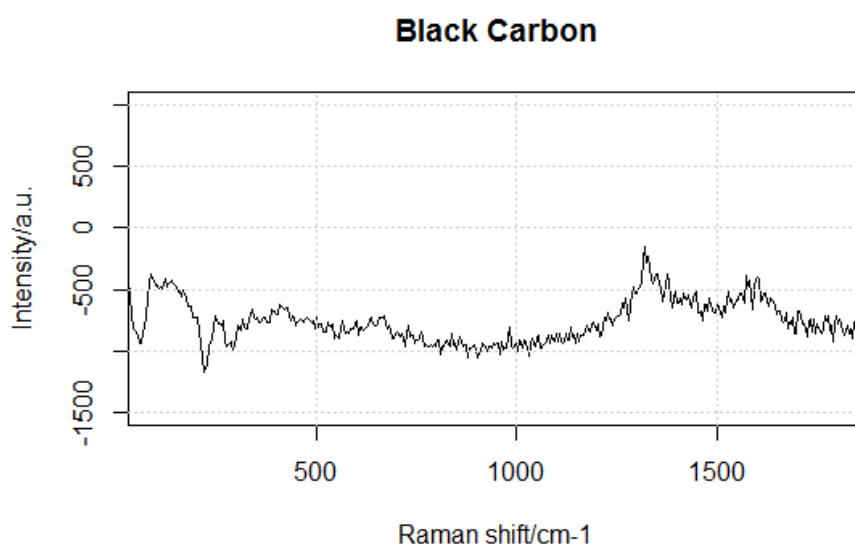
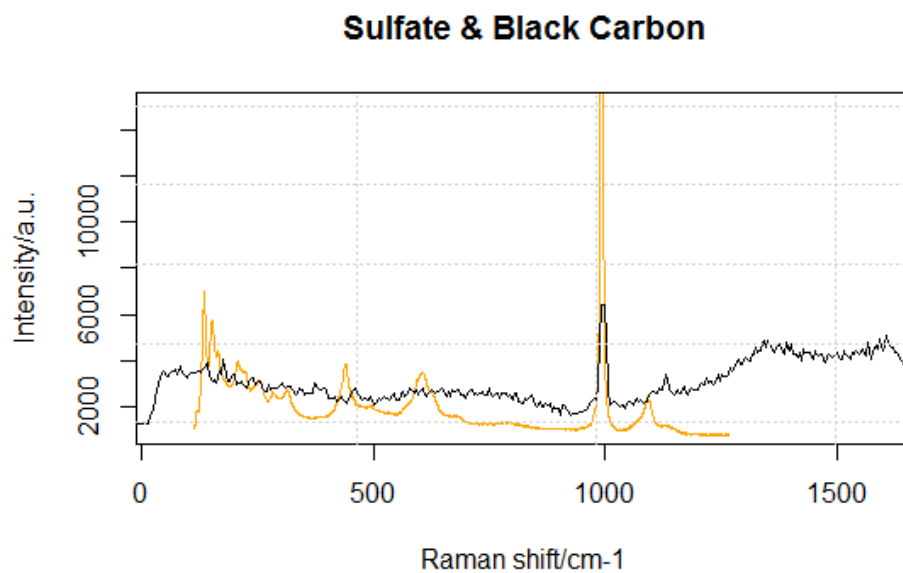


10.6 Examples for the Raman spectra

Sulfate (including ice spectrum)

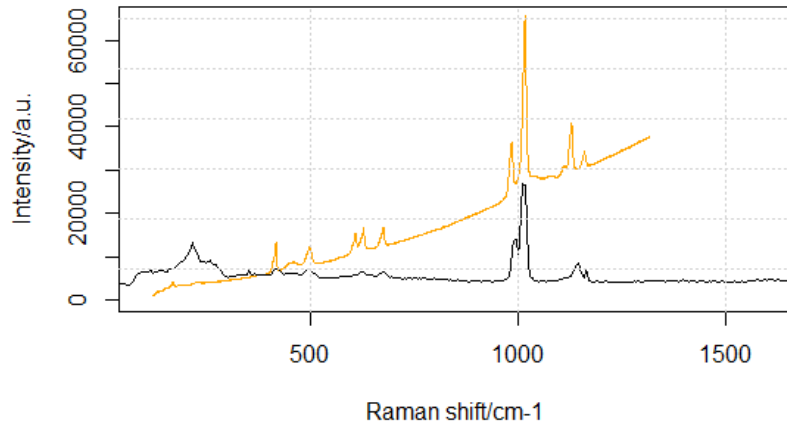


The black graphs show the spectra obtained for this work (with background correction); the orange graphs show the reference spectra (taken from the RRUFF database).

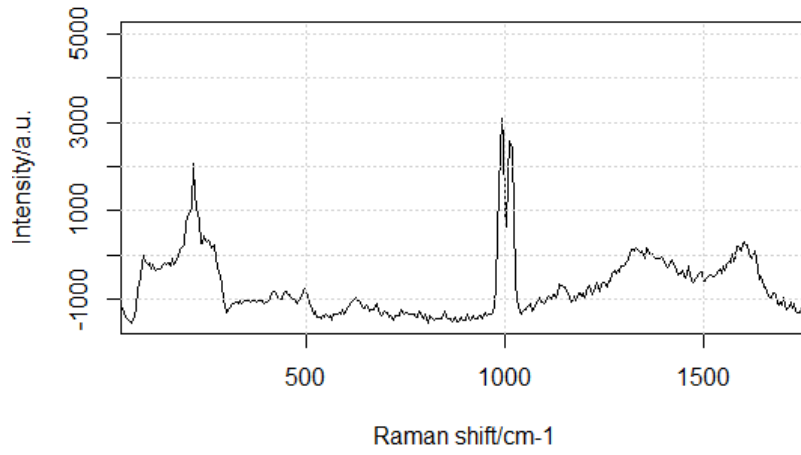


For a reference for black carbon see e.g. BEYSSAC ET AL. 2002; HODKIEWICZ 2010.

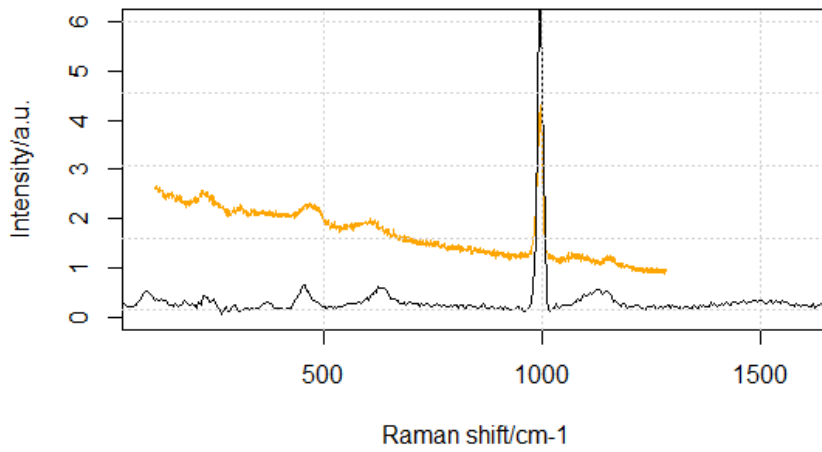
Na Sulfate



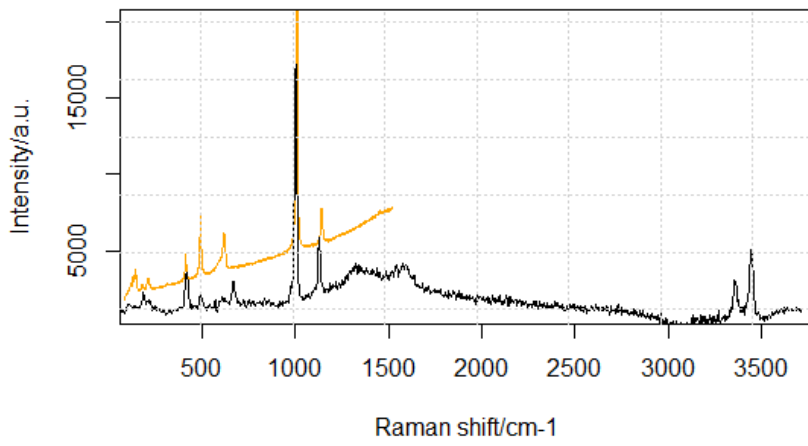
Na Sulfate & Black Carbon



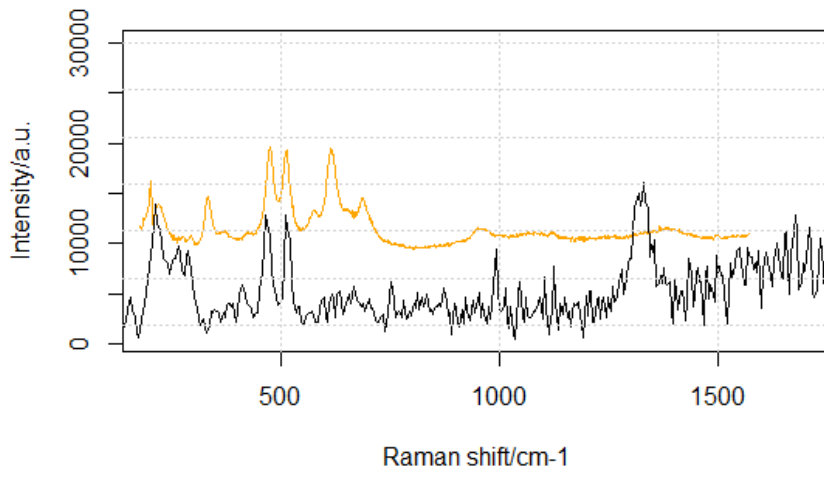
Ca Sulfate



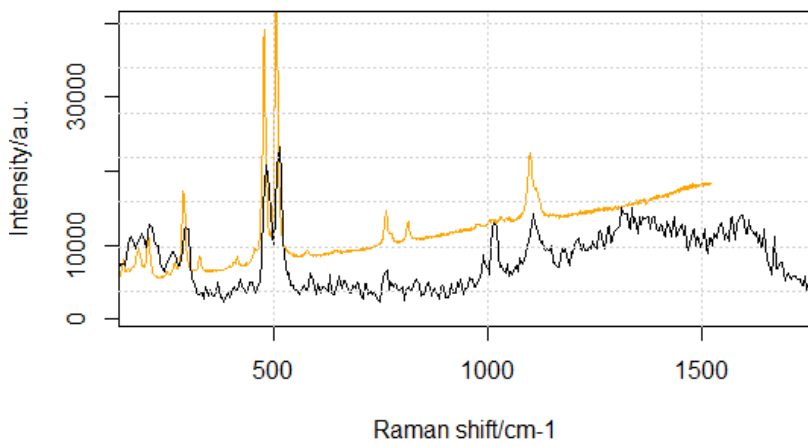
Gypsum & Black Carbon



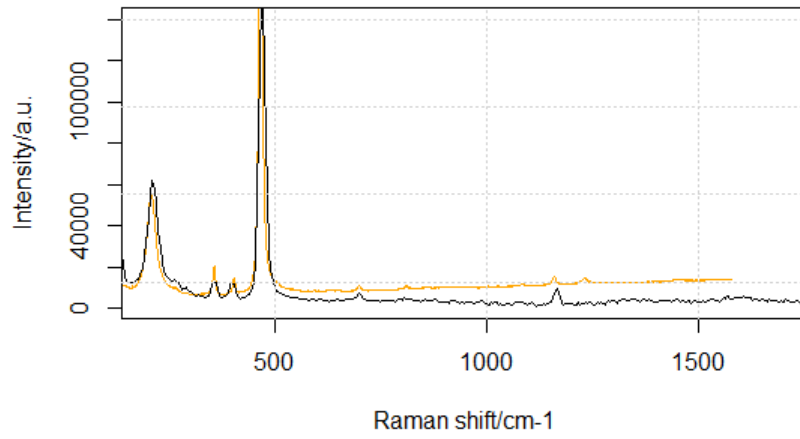
Silicate



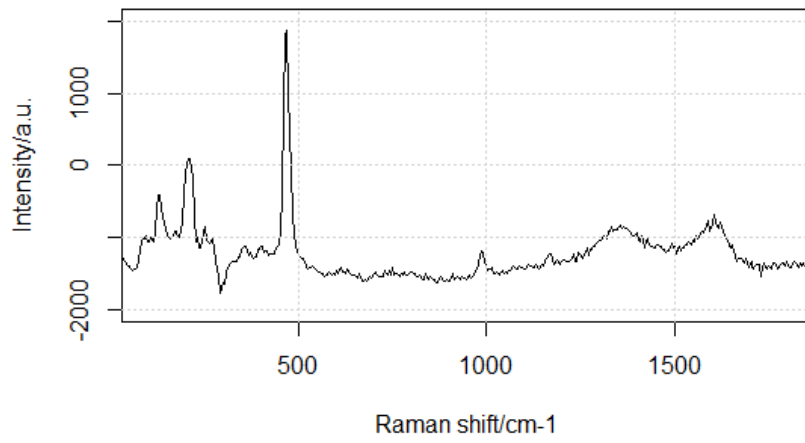
Feldspar & Black Carbon



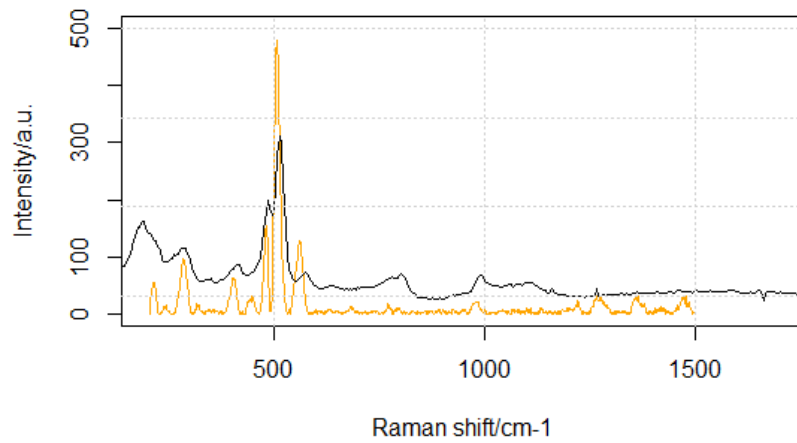
Quartz



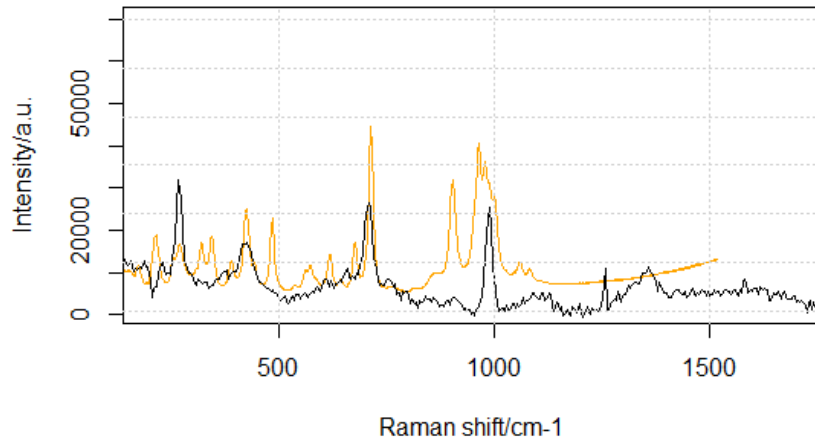
Quartz & Black Carbon



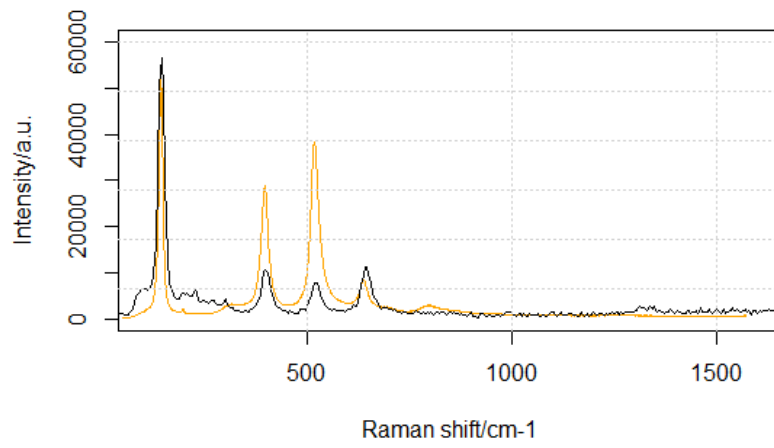
Plagioclase



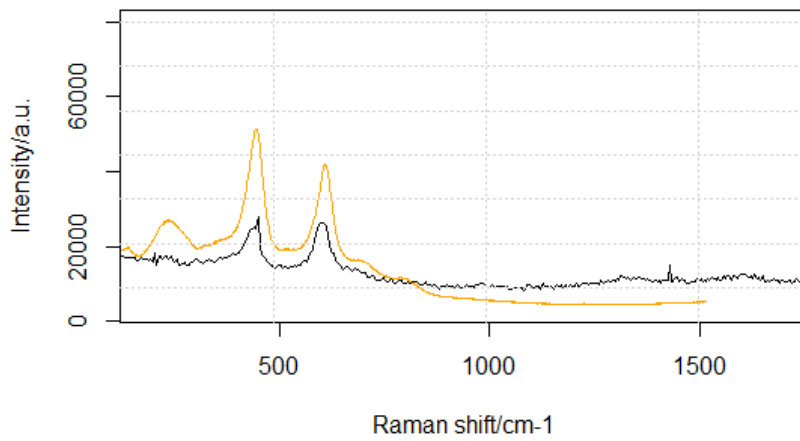
Ca Fe OH & Black Carbon



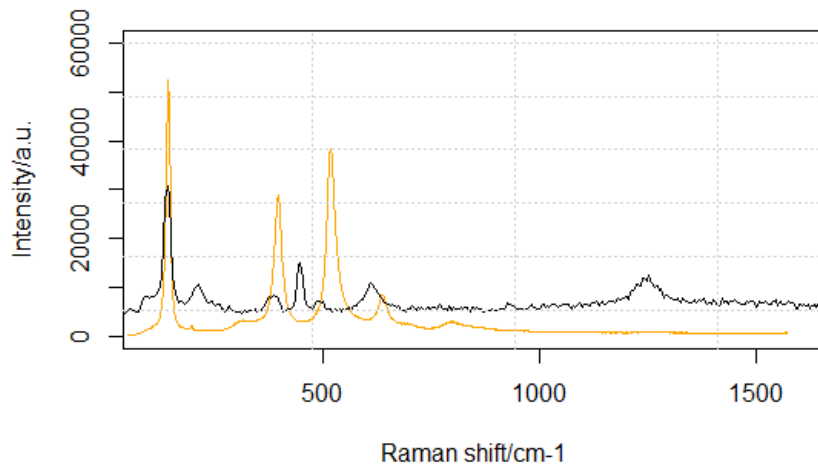
TiO2 (anatase)



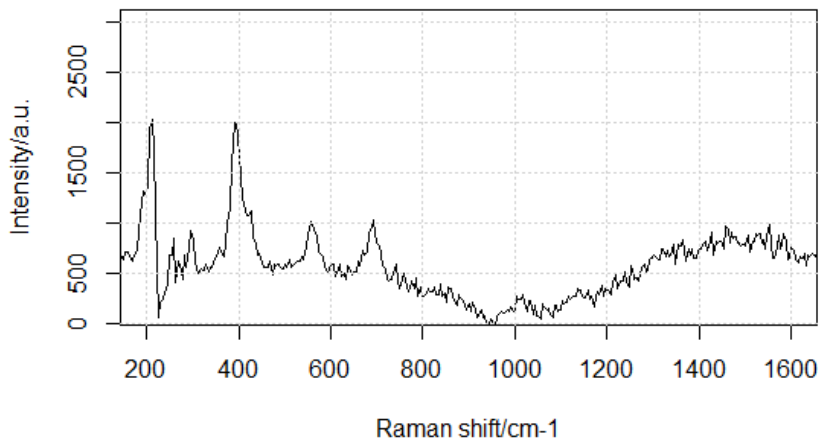
TiO2 (rutile)



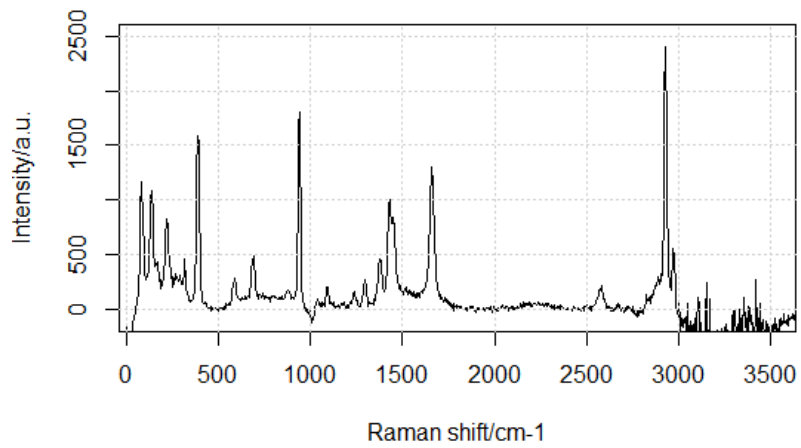
TiO2 mix



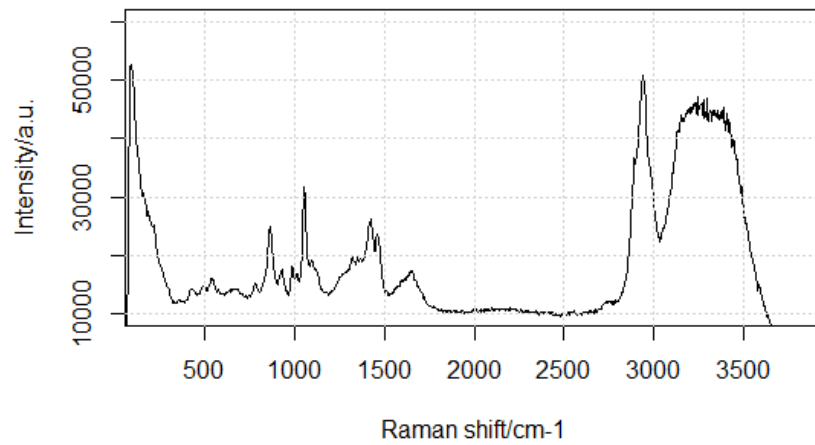
unidentified anorganic spectrum



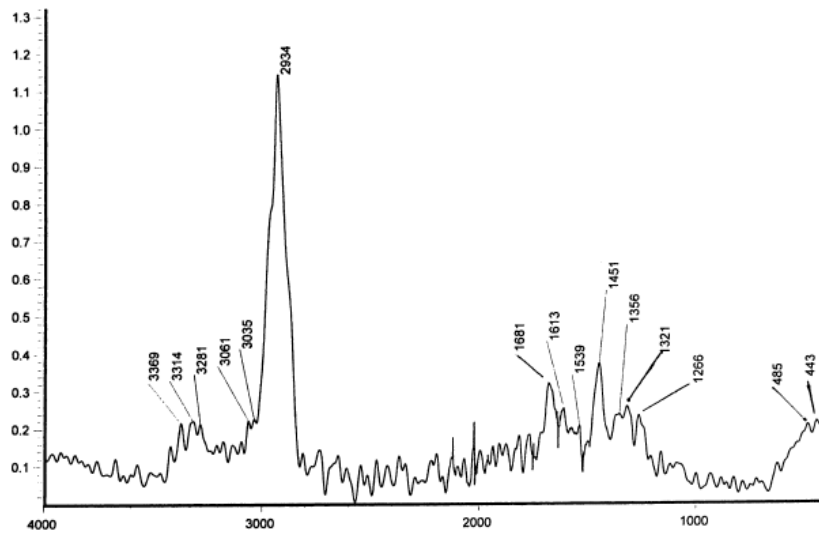
unidentified organic spectrum



unidentified organic spectrum (bacteria?)

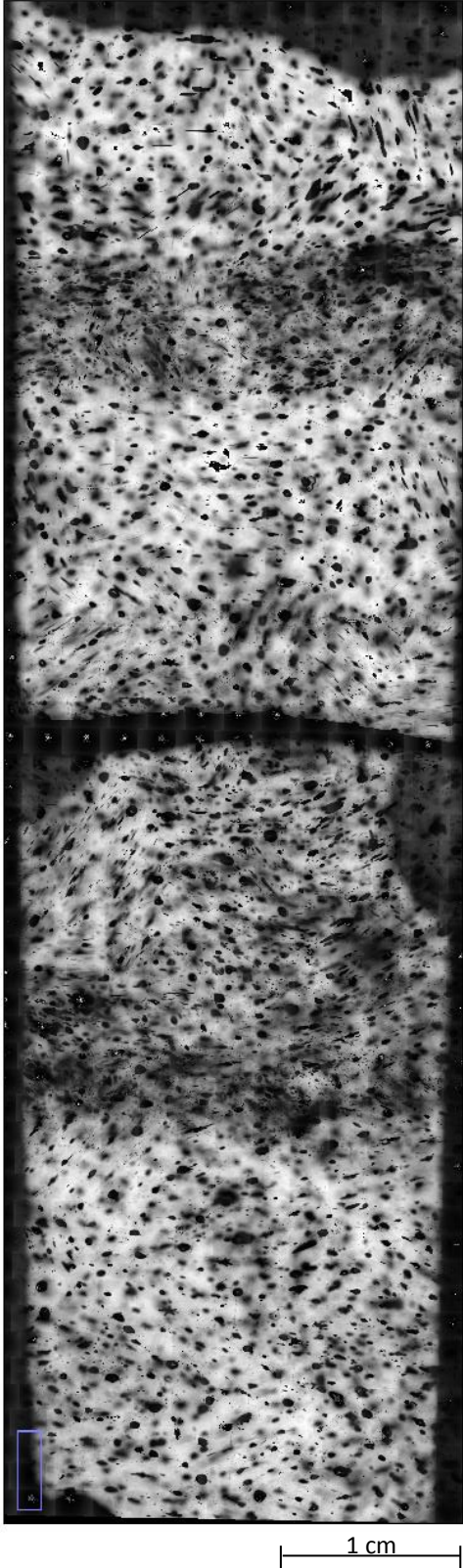


Raman spectrum of *Azospirillum brasilense* Sp7 as a possible identification for the organic spectrum shown above (KAMNEV ET AL. 2001):

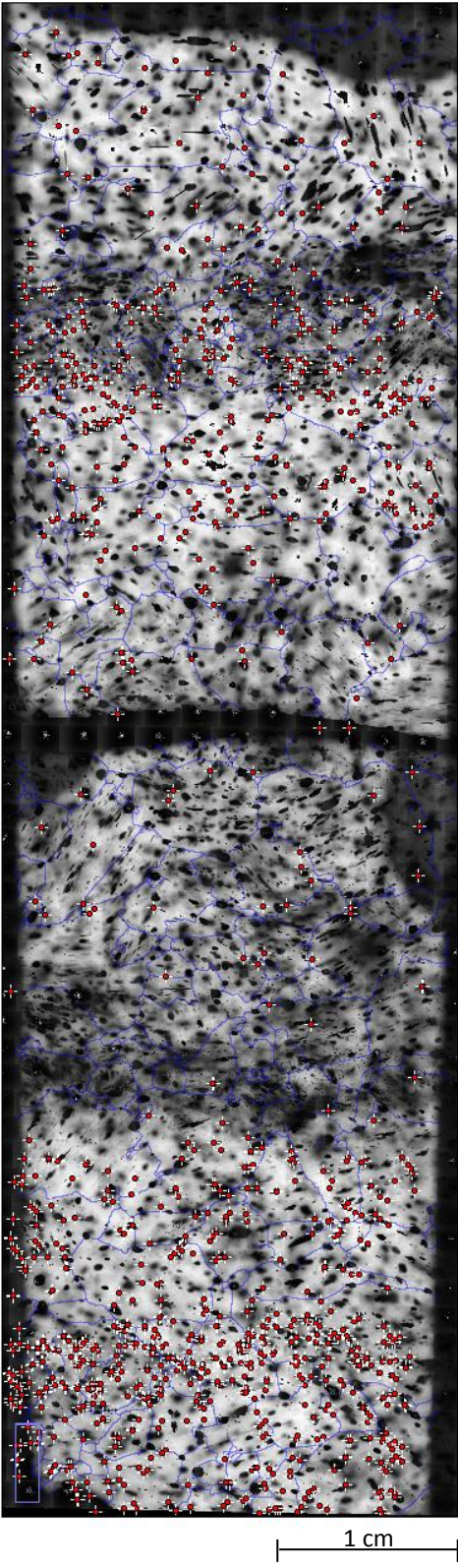


10.7 Microstructure maps of bag 1346_201 and 1346_501

Microstructure map of section 201 with marked grain boundaries and labelled black dots (right) and without (left)

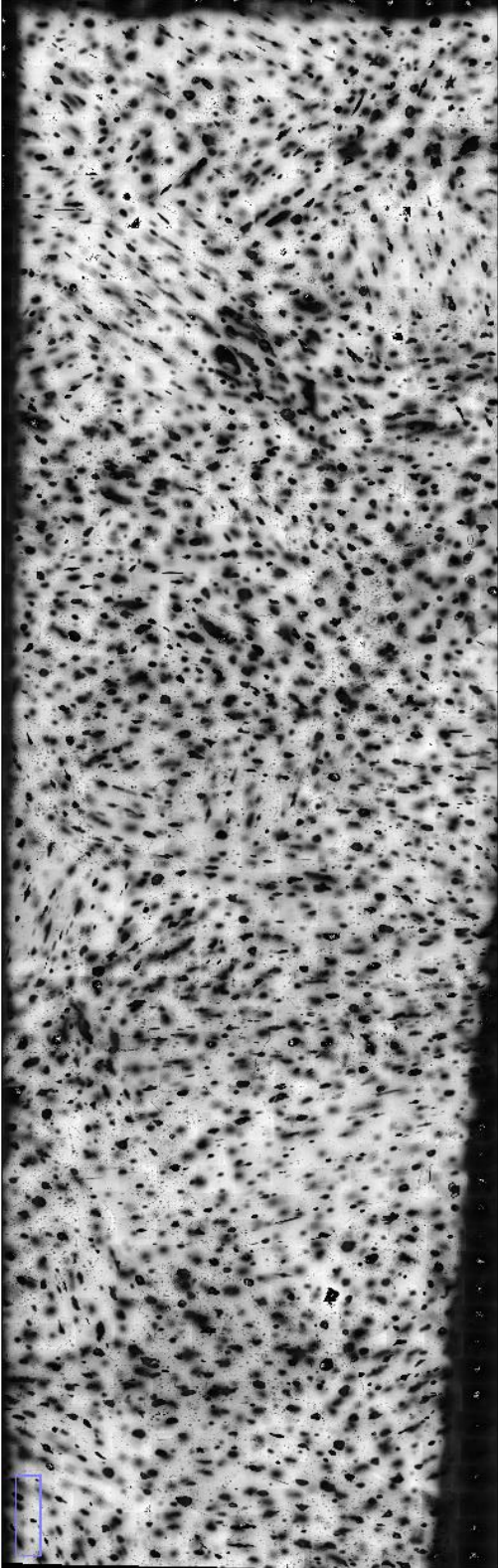


top

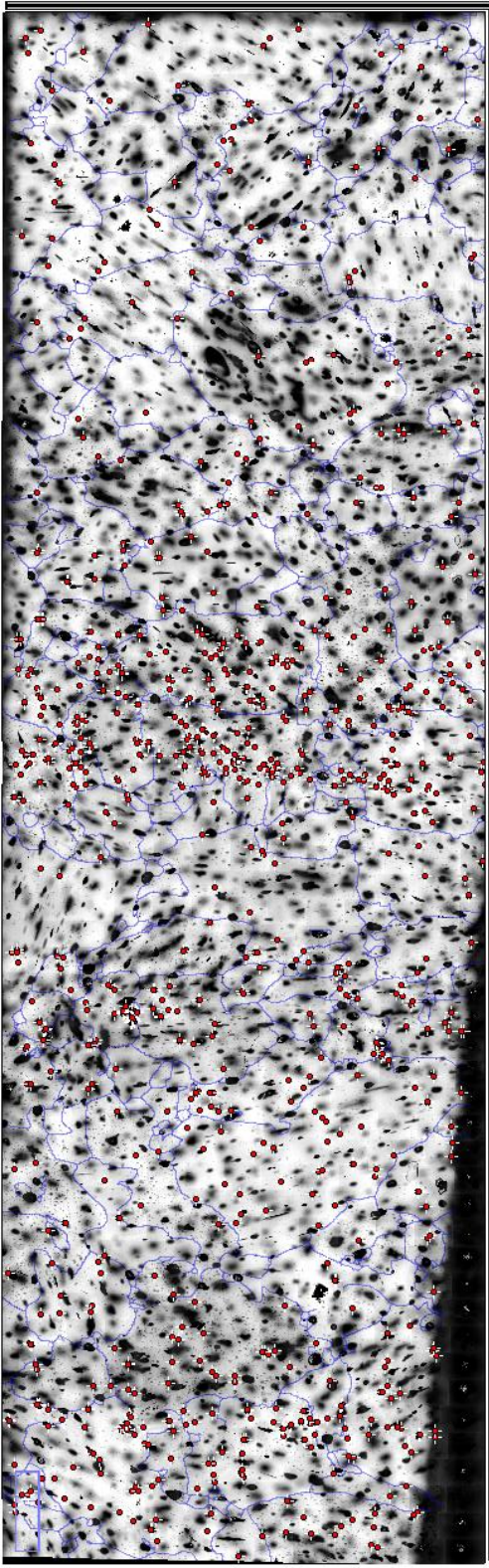


bottom

Microstructure map of section 501 with marked grain boundaries and labelled black dots (right) and without (left)



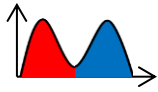
top



bottom

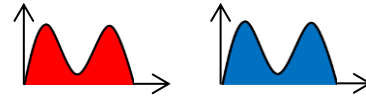
10.8 Summarized results of the Raman measurements

Colour code for the pie charts:



mixed

Sulfate (Al Sulfate)	S1
Na Sulfate	S2
Ca Sulfate	S3
Black Carbon	B1
BC & Sulfate/Phosphate	B2
BC & Na Sulfate	B3
BC & Gypsum	B4
BC & Feldspar	B5
BC & Quartz	B6
BC & Ca Fe OH	B7
Silicate	C1
Quartz	C2
Plagioclase	C3
TiO2 (Rutile & Anatase)	T1
TiO2 mixed signal	T2
unidentified	U
no spectrum	N

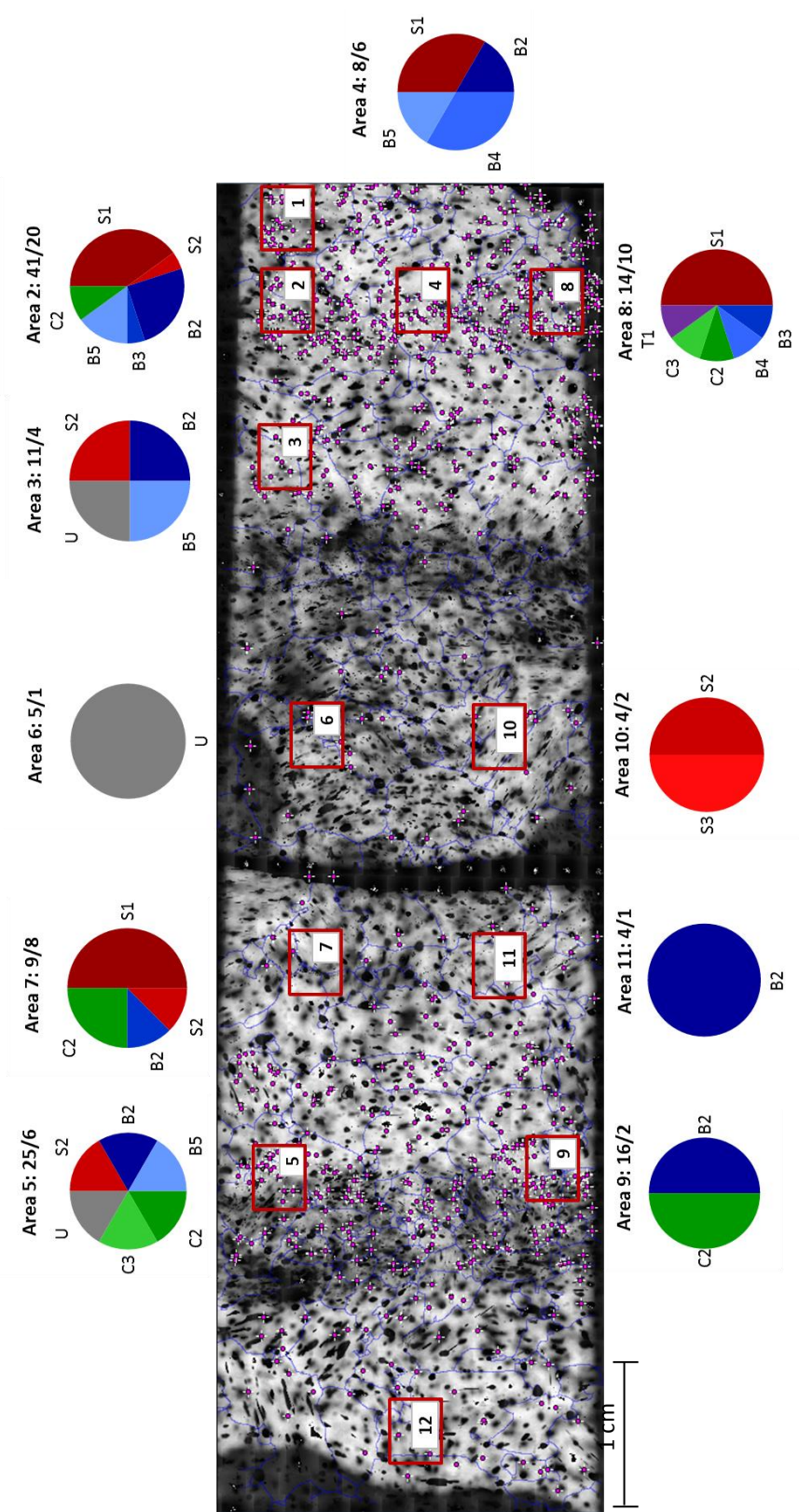


separated

Sulphate/Phosphate	S1
Sulfate (Al Sulfate)	S2
Na Sulfate	S3
Ca Sulfate	S4
Gypsum	S5
Black Carbon	B
Silicate	C1
Quartz	C2
Feldspar	C3
Plagioclase	C4
Ca Fe OH	F
TiO2 (Rutile & Anatase)	T1
TiO2 mixed signal	T2
unidentified	U
no spectrum	N

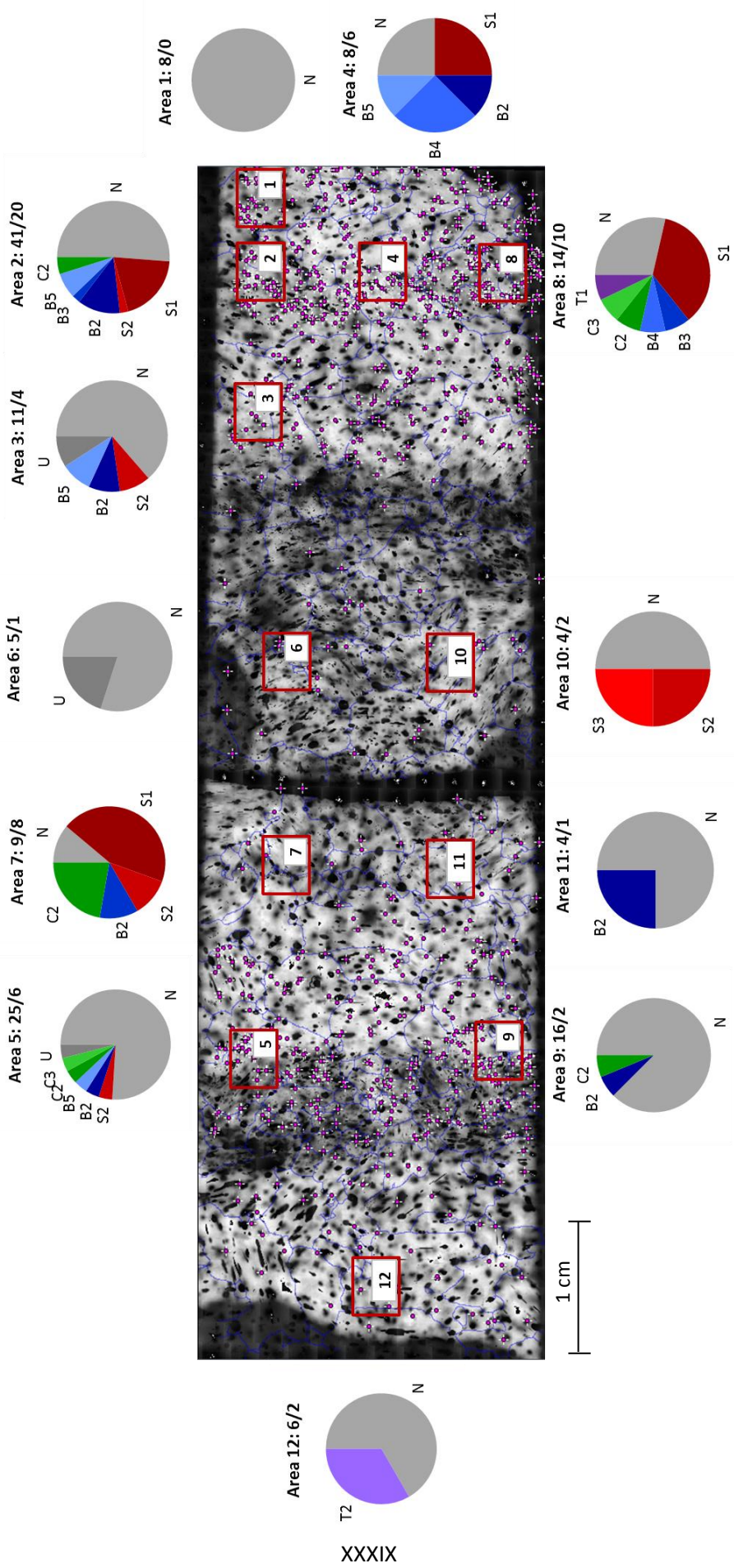


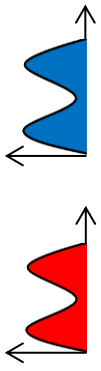
Bag 1346_201: particles that showed a spectrum included (mixed signal, fig.a)



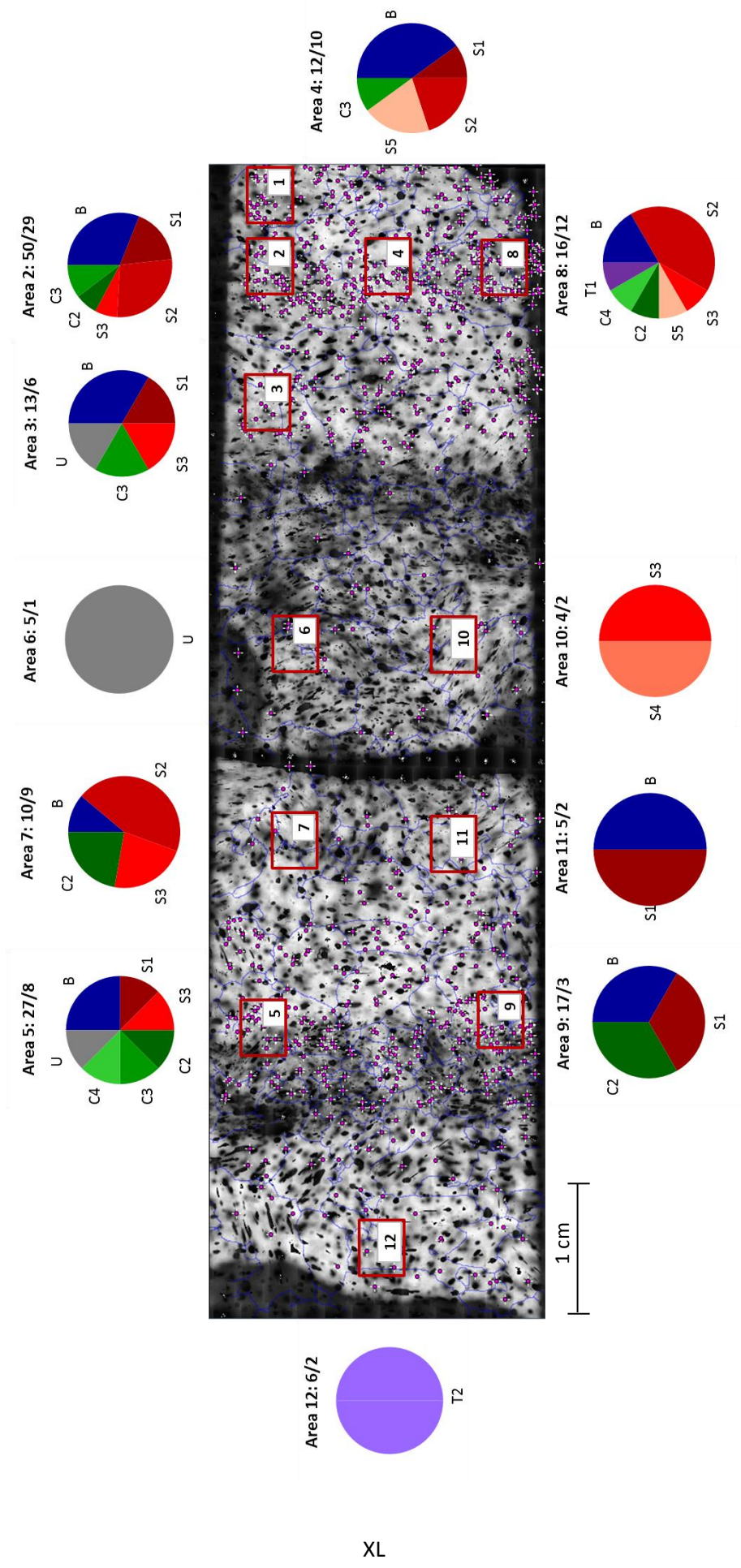


Bag 1346_201: all particles included (mixed signal, fig. b)

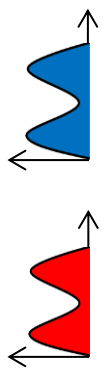




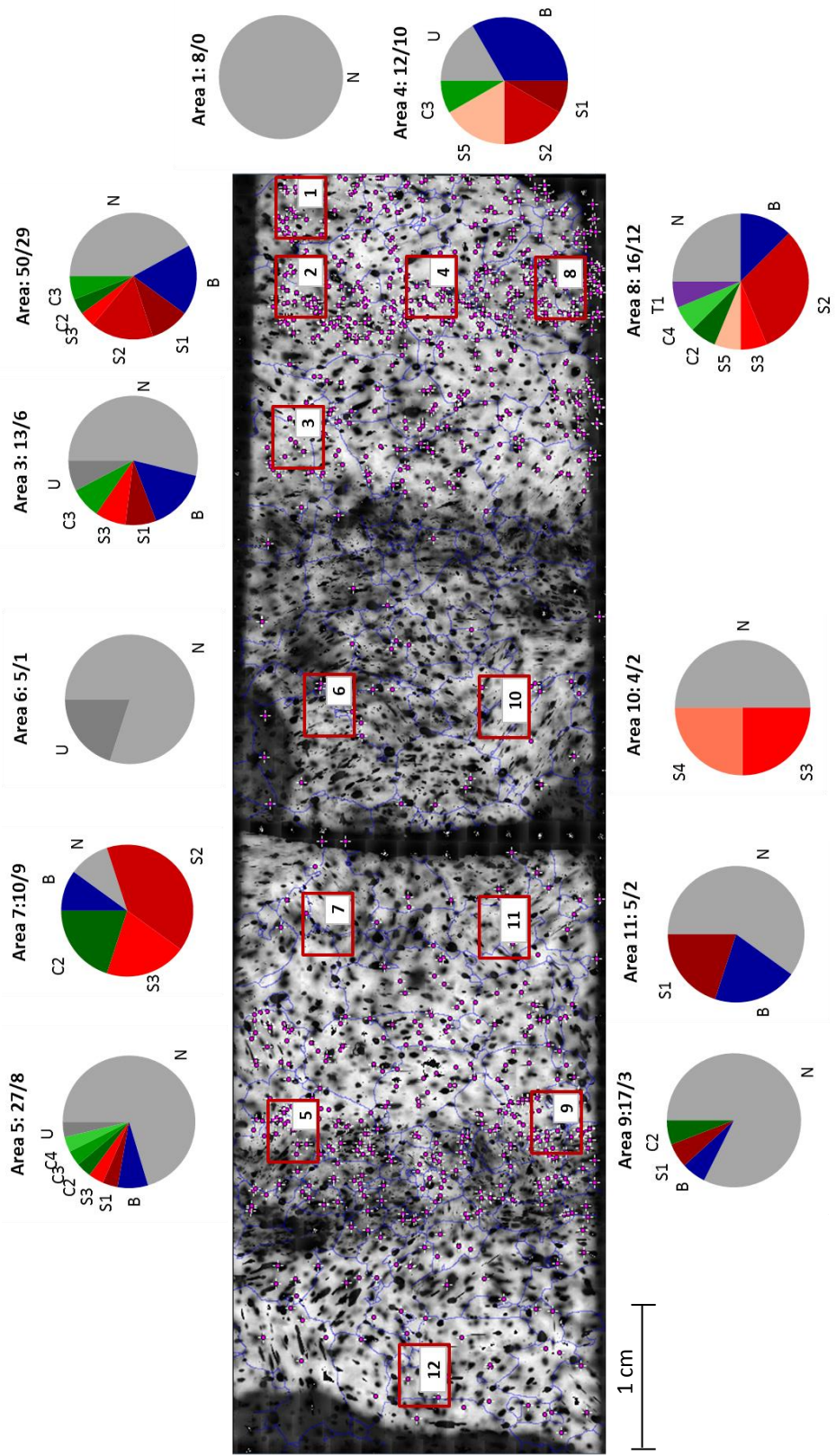
Bag 1346_201: particles that showed a spectrum included (separated signal, fig c)



XL

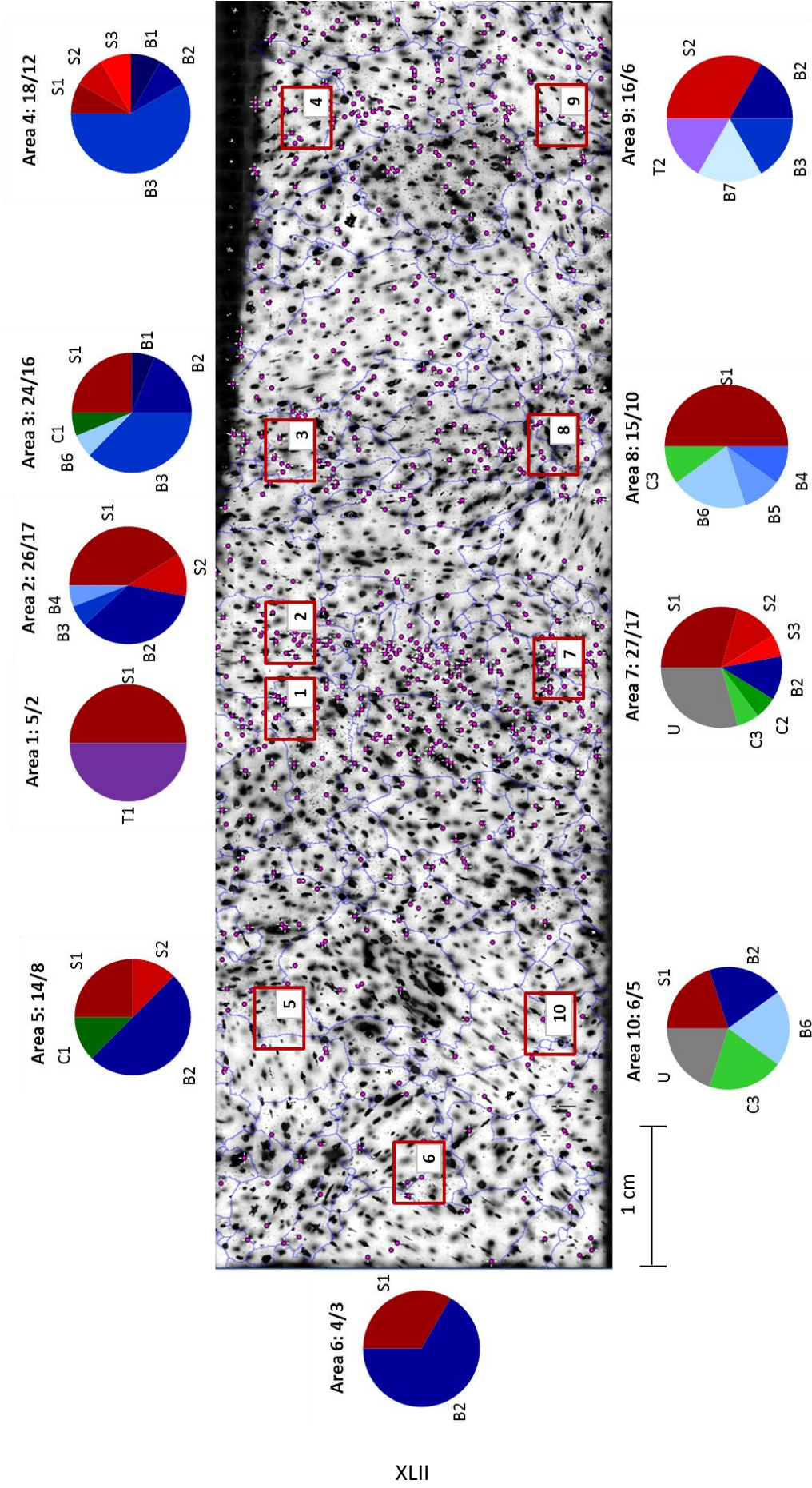


Bag 1346_201: all particles included (separated signal, fig. d)



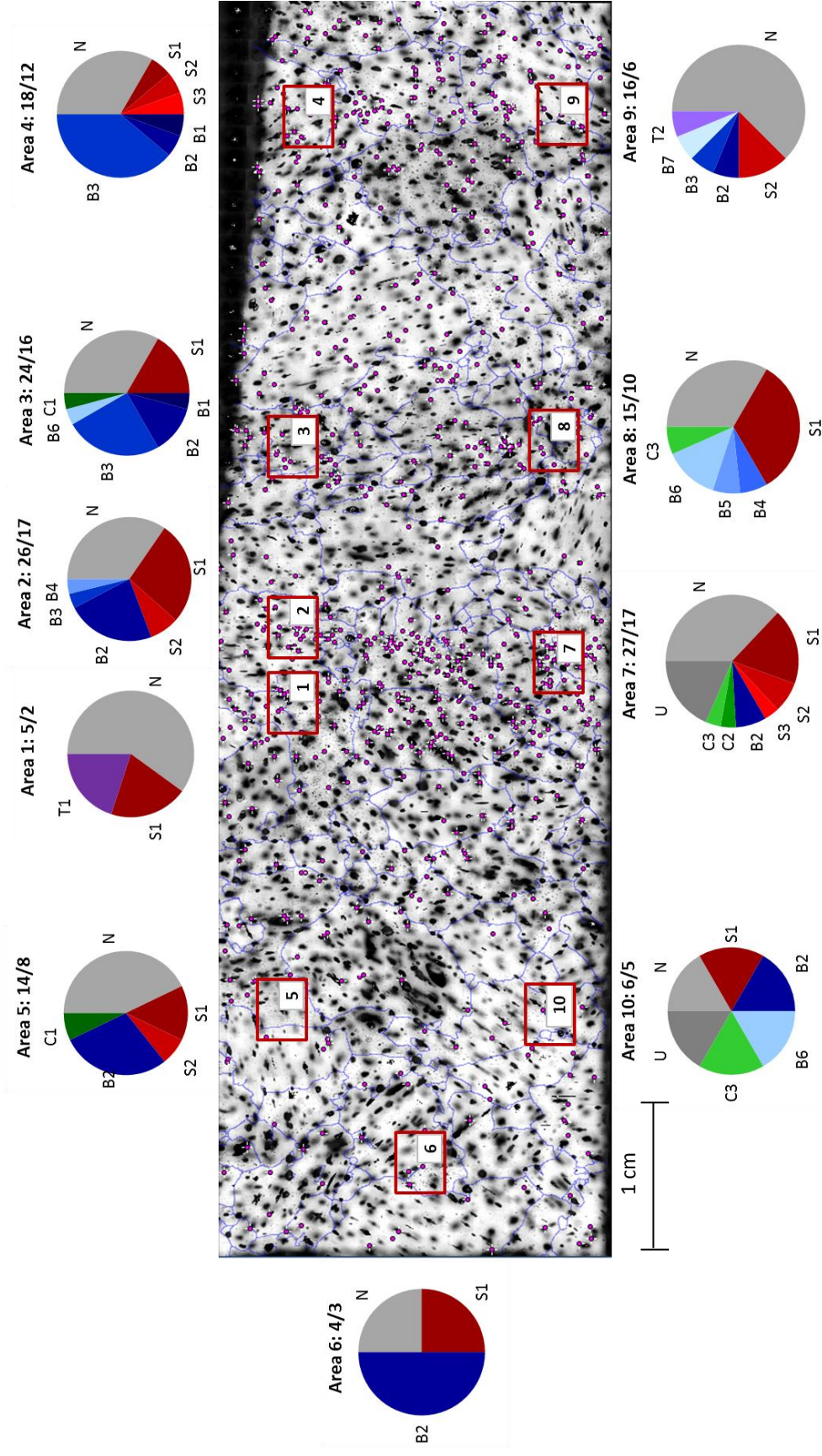


Bag 1346_501: particles that showed a spectrum included (mixed signal, fig a)

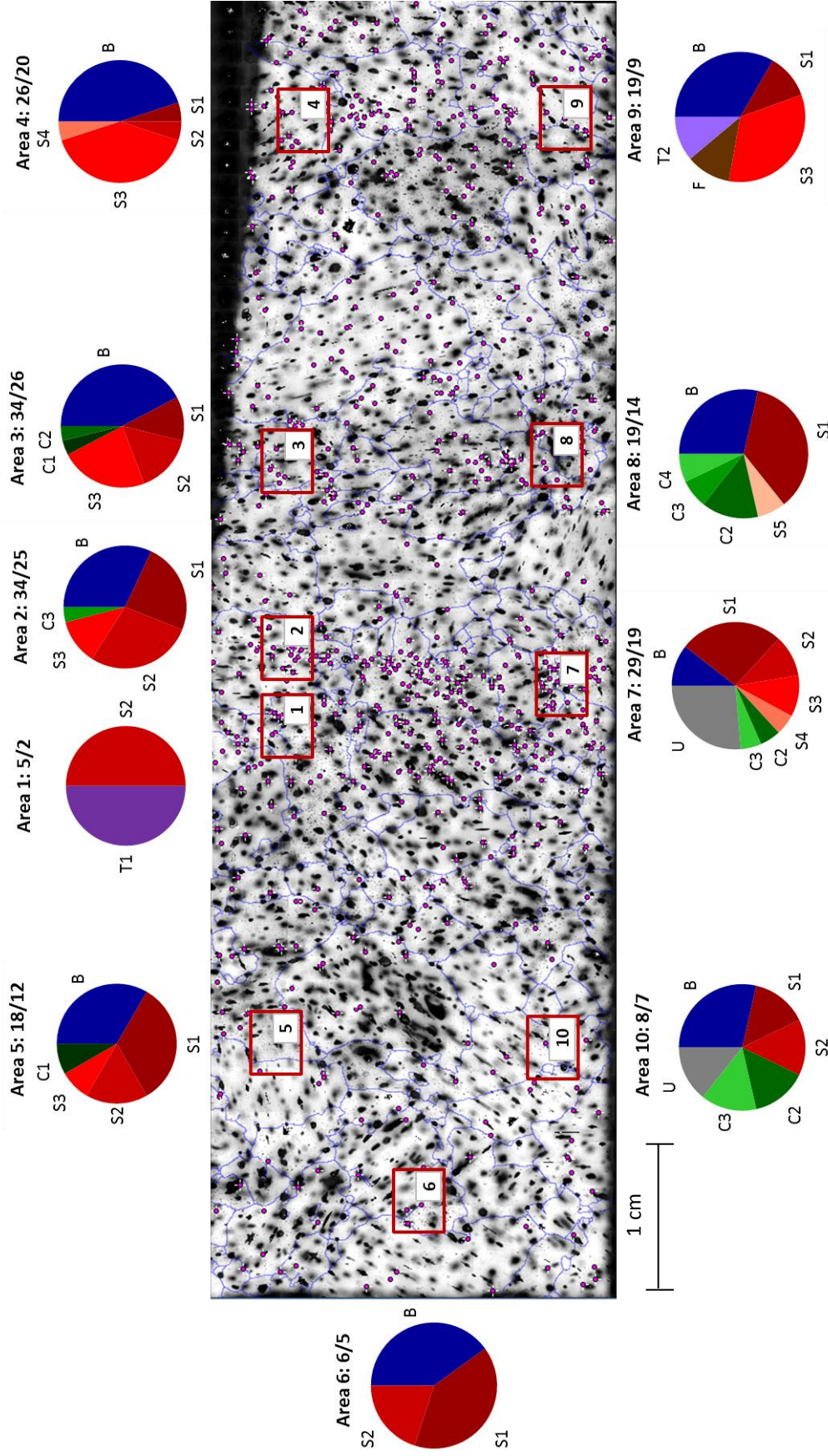
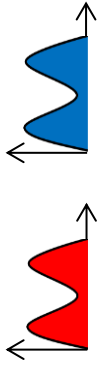


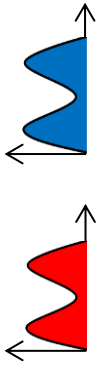


Bag 1346_501: all particles included (mixed signal, fig. b)

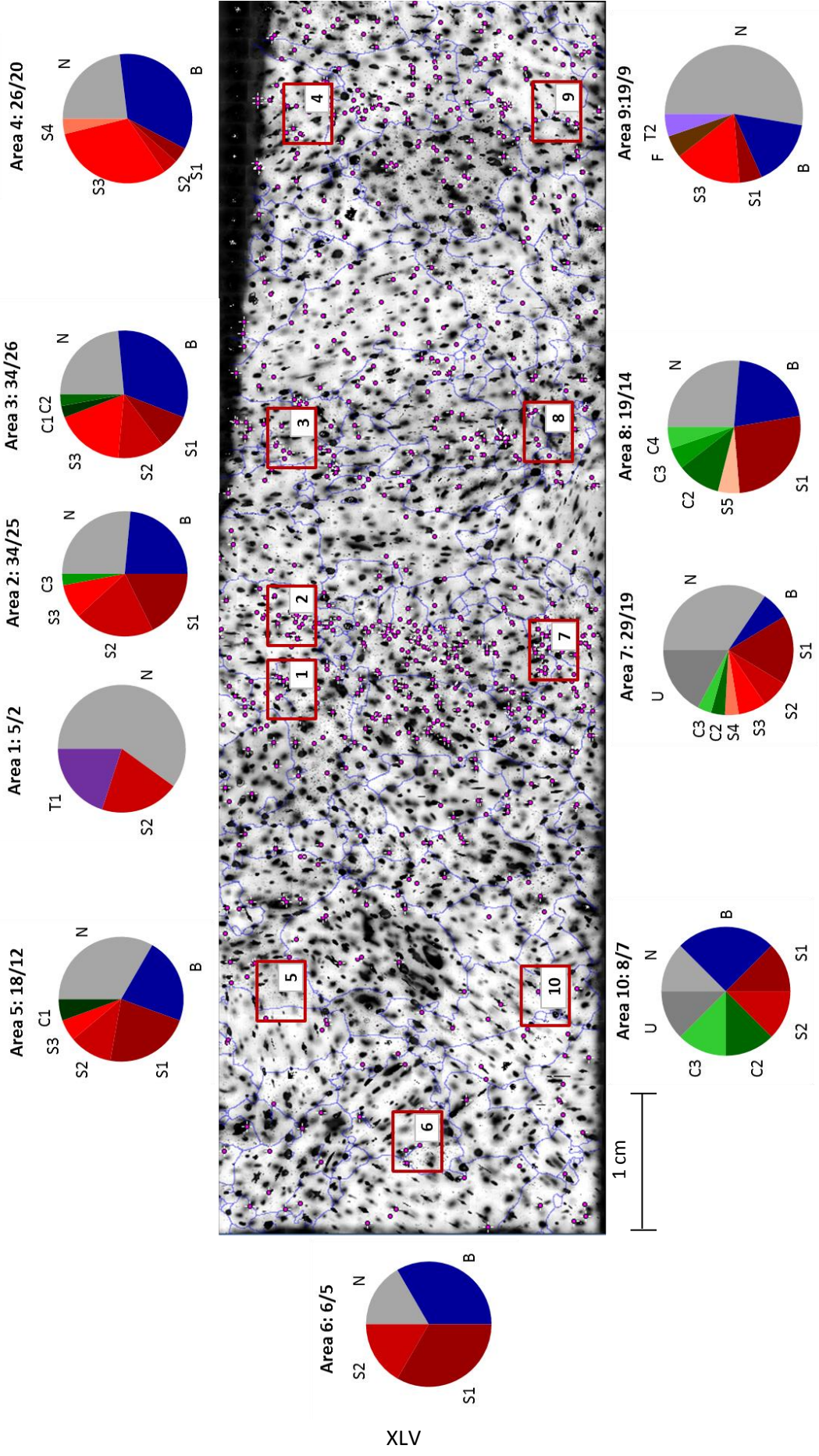


Bag 1346_501: particles that showed a spectrum included (separated signal, fig. c)



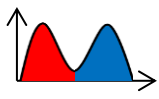


Bag 1346_501: all particles included (separated signal, fig. d)



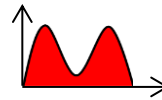
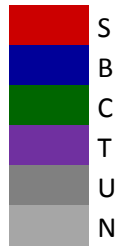
XLV

Colour code for the pie charts for the entire section/both section:



mixed

sulfate
black carbon
silicate
TiO₂
unidentified
no spectrum

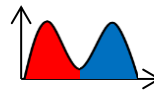


separated

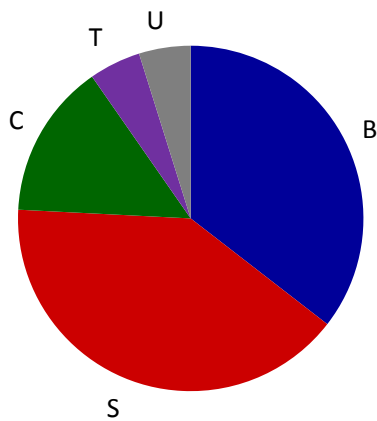
sulfate
black carbon
silicate
Ca Fe OH
TiO₂
unidentified
no spectrum



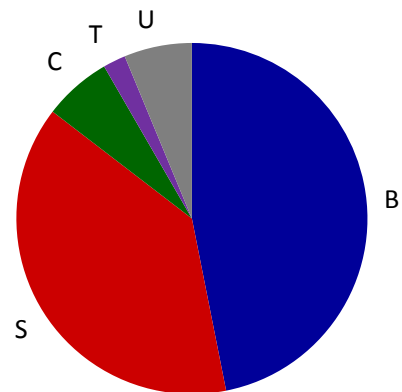
Summarized pie charts for each section (mixed signal)



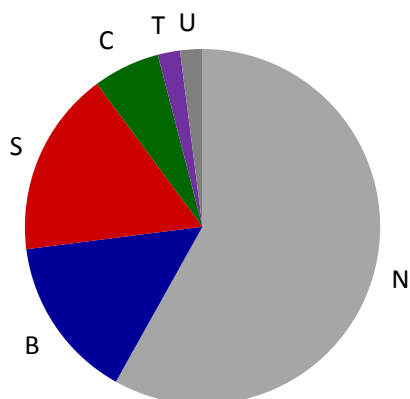
1346_201: 151/62



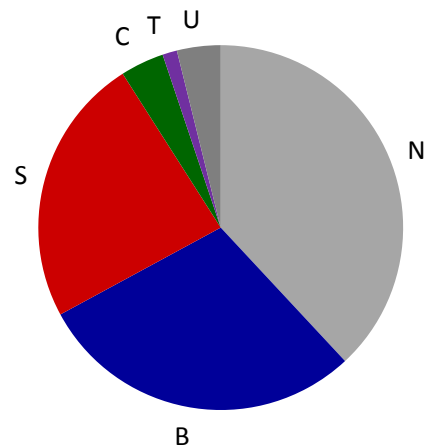
1346_501: 155/96



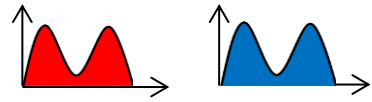
1346_201: 151/62



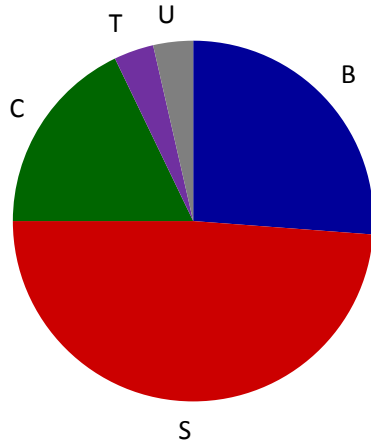
1346_501:155/96



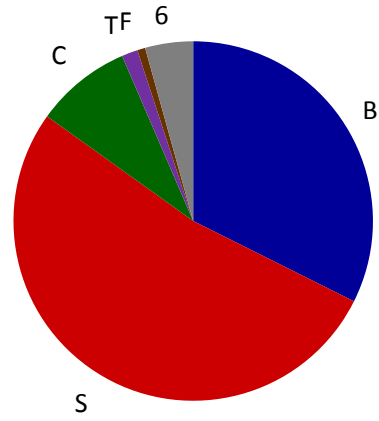
Summarized pie charts for each section (separated signal)



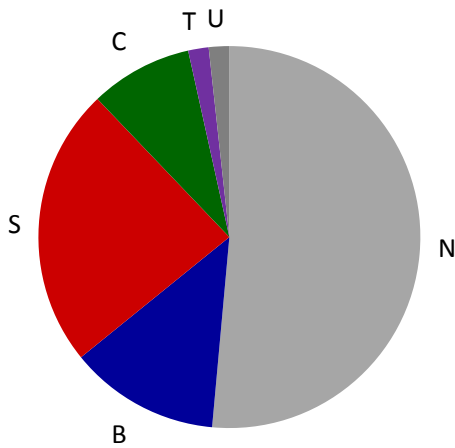
1346_201: 173/84



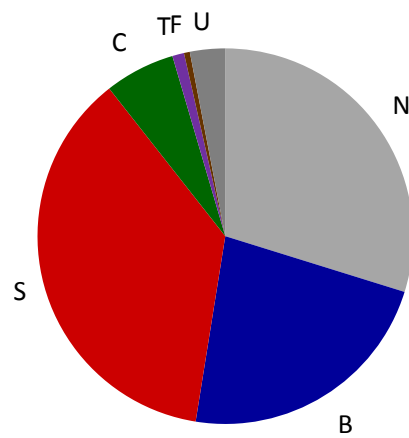
1346_501: 198/139



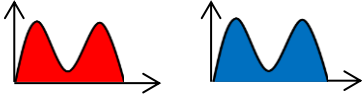
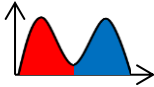
1346_201:173/84



1346_501: 198/139

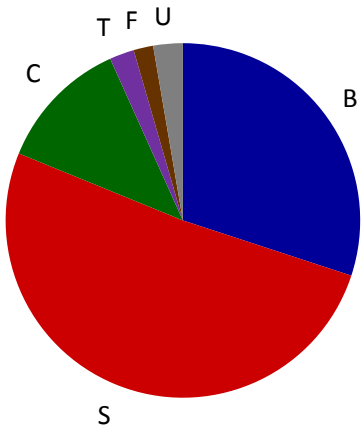
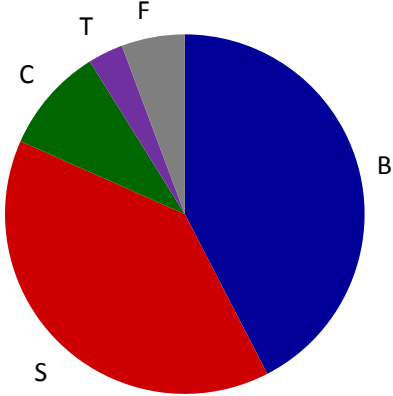


Summarized pie charts for both sections as mixed (left) and separated signal (right)



1346_201/501: 306/158

1346_201/501: 371/223



1346_201/501: 306/158

1346_201/501: 371/223

